EXPERIMENTAL AND THEORETICAL INVESTIGATIONS OF A NEW INTEGRATED SOLAR TOWER SYSTEM FOR PHOTOCATALYTIC HYDROGEN AND POWER PRODUCTION

By

Rafay Shamim

A Thesis Submitted in Partial Fulfillment

of the Requirements for the Degree of

Master of Applied Science in Mechanical Engineering

Faculty of Engineering and Applied Science

University of Ontario Institute of Technology

Oshawa, Ontario, Canada

Abstract

Solar energy conversion via photocatalytic hydrogen production from water is an attractive route for the propagation of a hydrogen economy. Increasing the efficiency of such systems to meet the target of 10% is essential for industrial their adoption. A new hybridized system employing a photocatalytic reactor and photovoltaic cells in a cavity receiver of a solar tower system is proposed. A fully functioning lab scale system, capable of handling continuous flow processes, is built, and experiments are conducted to investigate the behaviour of this system.

Production of hydrogen in the photo-reactor is observed to increase with an increase in temperature and a decrease in the pressure to below the atmospheric pressure. A maximum quantum efficiency of 1.9% is achieved with a 77% - 23% ratio of CdS – ZnS mixture under a visible light source. With power output from the light harnessed by the photovoltaic cells, the energy efficiency is increased from 0.2% to 2%, respectively. The optimal flow rate for an electrolyte concentration of 0.3 M and reactor volume of 90 ml is determined to be 50 ml/h.

A thermodynamic study of a proposed large scale system is conducted. This system combines a photocatalytic process, a photovoltaic process, and a heat engine to efficiently utilize solar radiation. For a given solar tower system that requires a reflective area of 913, 289 m^2, energy and exergy efficiency values up to 40% and 30% are achieved respectively. Based on archived solar data, for a given summer day the system produces 50 tonnes of hydrogen if outputs from the photovoltaic process and the heat engine are used to run an electrolyzer.

Acknowledgements

I would like to extend my gratitude foremost to my supervisor, Dr. Ibrahim Dincer, and my co-supervisor, Dr. Greg Naterer, for giving me the opportunity to work under their supervision on this project, for providing academic guidance, and for constantly encouraging me.

I would like to thank Dr. Calin Zamfirescu for his help with the various obstacles and issues that I encountered during the project, particularly with the experimental setup and the thermodynamic analyses.

I would like to acknowledge all my colleagues at the Clean Energy Research Laboratory (CERL); especially Ed Secnik, for patiently dealing with the many organizational issues I presented him with, and Ron Roberts, Ehsan Baniasadi, and Musharraf Rabbani for their valuable technical inputs.

I would also like to thank Hassan Bokhari, Nasir Awan, Ali Tariq and Osman Sheikh, for allowing me a haven where I could step away from it all, leave my research at the door, and recharge myself for the fight.

Most significantly, I would like to thank my family; my sisters, for leaving me without burden at home, and my parents, for instilling in me the desire to achieve; for setting the bar high, by becoming what they have become, yet never putting any pressure on me. They taught me never to admit defeat, and never to give up the desire to see the light at the end. Without them, it wouldn't have been possible.

Finally, I would like to show my appreciation to the Phoenix Canada Oil Company and the University of Ontario Institute of Technology for their financial support.

Table of Contents

List of Figures

List of Tables

Nomenclature

a	Solution degradation variable
A	Area (m^2)
$\mathcal{A}$	Avogadro's number
c	Constant (mK)
$\mathbb{c}$	Speed of light (m/s)
$\dot{E}$	Energy flow rate(W)
ex	Specific exergy (J/kg)
Ex	Exergy (J)
$\dot{E}x$	Exergy flow rate (W)
f	Optical factor
F_{field}	Compounded heliostat field factor
G	Gibbs energy of formation (J)
h	Specific enthalpy (J/kg)
H	Enthalpy (J)
$\mathbb{h}$	Plank's constant (m^2kg/s)
I	Intensity of solar radiation (W/m^2)
$\bar{I}$	Normalized intensity
$\mathbb{I}$	Current (A)
k	Extinction coefficient
K	Constant (J/K)
$\mathbb{m}$	Non ideality constant

$\mathcal{n}$	Refractive index
$\dot{n}$	Mole rate (mol/s)
n	Number of moles
P	Pressure (Pa)
$\dot{Q}$	Heat flow rate (W)
q	Elementary charge (C)
R	Resistance (Ω)
r	Rate (mmol/min)
$\mathcal{R}$	Reflectance (%)
$\bar{R}$	Universal gas constant (J/mol.K)
s	Specific entropy (J/kg.K)
S	Entropy (J/K)
$\dot{S}$	Entropy flux (W/m^{2}K)
T	Temperature (K)
U	Uncertainty (%)
V	Volume (m^3)
$\dot{V}$	Volume flow rate (m^3/s)
$\mathbb{V}$	Voltage (V)
$\dot{W}$	Work rate (W)
y	Mole fraction
Y	Calculated quantity

Greek Letters

Δ	Difference
η	Efficiency
λ	Wavelength (nm)
Φ	Quantum efficiency
Ω	Ohm
θ	Inclination angle

Subscripts

0	Reference state
at	Attenuation
b	Blocking factor
c	Cell
ch	Chemical
conc	Concentration
cond	Condensor
d	Destruction
diff	Diffuser
en	Energy
ex	Exergy
exch	Heat exchanger
gen	Generation
i	Index

in	Input
M	Maximum power point
oc	Open circuit
ph	Photon
$phys$	Physical
$prod$	Production
r	Reaction vessel
s	Series
S	Solar
$\mathit{ѕ}$	Shading factor
sc	Short circuit
sh	Shunt
sol	Solution
t	Time
th	Thermal
$turb$	Turbine
w	Cavity receiver window
γ	Optical aberration

Acronyms

AM	Air Mass
ASTM	American Society for Testing and Materials
CB	Conduction band

CSTR	Continuous stirred tank reactor
DOE	Department of energy
ECM	Electrical management unit
HHV	Higher heating value
HTF	Heat transfer fluid
IPCC	Intergovernmental Panel on Climate Change
LED	Light emitting diode
LMTD	Log mean temperature difference
MPPT	Maximum power point tracker
NREL	National Renewable Energy Laboratory
NI	National Instruments
NIST	National Institute of Standards and Technology
OAI	Solar simulator manufacturer
ORC	Organic rankine cycle
PEC	Photo electrochemical
PEM	Proton exchange membrane
PV	Photovoltaic
PW	Picowatt
SAM	System Advisor Model
TW	Terawatt
UOIT	University of Ontario Institute of Technology
VB	Valence band

Chapter 1: Introduction

1.1 Energy Issues

The world consumes a large amount of energy at present and still depends on fossil fuels to supply it (Goldemberg, 2006). The problem with this is two pronged; fossil fuel usage leads to accelerated change in global warming, and its reserves are diminishing. In a period of 20 years, the worldwide consumption of coal, oil and natural gas increased 22%, 27%, and 71% respectively, resulting in an increase of CO_2 emissions from 5 billion to 6.6 billion metric tons (Chow et al., 2003). In 2008, emission levels reached approximately 9 billion metric tons, a staggering increase (Boden et al., 2010). The IPCC stated in 2001 that continued emissions of CO_2 above sequestration capacity of natural sinks will result in not only increased mean temperatures, but also the additional issue of a greater frequency of extreme climatic events such as droughts and intense storms (Chow et al., 2003). This has proven to be true considering the occurrence of a major disaster almost every year of the last decade. It is estimated that at the current consumption rate, coal, natural gas, and oil will run out in 130 years, 60 years, and 42 years, respectively (Abbott, 2010). Others have used different models to arrive at similar conclusions (Shafiee and Topal, 2009). Dissenting voices to both of these problems exist, but they are outnumbered by those professing a belief in their existence (Maugeri, 2004; Powell, 2013; Watkins, 2006).

1.2 Potential of Renewables

Renewable sources of energy contain the potential to alleviate both of these issues, as they are inexhaustible and have a significantly smaller environmental impact. While changes in landscape, noise pollution, and effect on ecology caused by renewable sources may be termed as

negatives, their effect is certainly not as direct as that of fossil fuels. Among the renewable sources of energy, the energy received on the Earth's surface from the Sun seems to be the most promising, simply due to the sheer magnitude of the radiation. The Sunlight that is available for terrestrial solar collectors is 85 PW, significantly more than the global energy consumption of 15 TW. All the other sources of renewable energy combined amount to less than 1% of this value. Interestingly, even if only the solar power that is incident on the deserts of the world is considered, it is still 500 times more than the present consumption, and the other renewables amount to less than 3% of that value if combined (Abbott, 2010). This means that the solar energy can be harnessed away from populations, allowing the negative issues associated with it to be overcome. The versatility of solar energy is also an advantage over other forms of renewables. The ability to either use it as it arrives on the surface or concentrate it allows it to be used in a whole host of applications (Crabtree and Lewis, 2007).

1.3 Hydrogen as a Fuel

Fossil fuels may be classified as both a source of energy, and a fuel. A substance may be defined as a fuel if it has attributes that allow it to store and transport energy, and release it as desired. Thus, any renewable source of energy must be linked to a suitable fuel system in order to comprehensively replace fossil fuels. To this end, hydrogen is proposed as an attractive option. It has many advantages, such as a clean and renewable combustion cycle, increased safety due to its relatively low density, a high energy-mass ratio, and economically feasible long distance transmission. Its main disadvantage is its low energy-volume ratio. Even if compressed to a liquid form, the volumetric density of gasoline remains more than three times as large. In the liquid form, its handling and storage also becomes increasingly energy intensive (Bockris, 2013; Mazloomi and Gomes, 2012; Pagliaro et al., 2010). Despite this, the importance of hydrogen

production is not diminished as alternative fuel options, such as methanol, also require hydrogen for its production (Olah, 2005).

Since the use of hydrogen in combustion processes results in the production of water, it becomes ideally suited to be the source material of elemental hydrogen. This idea is further strengthened by the abundance of water on Earth, and its relative independence of geographical locations (Goldemberg, 2006). One of the proposed methods of obtaining hydrogen gas from water is through photocatalysis. Even removed from the issues of environmental degradation and fossil fuel reserves, which have spurred alternative energy research since the turn of the century, photochemical methods of energy production have been proposed from as far back as a century ago. The suggestion then was more to do with an appreciation of the superiority of energy conversion processes occurring in nature, and a need to mimic them in order to advance scientifically and industrially (Albini and Fagnoni, 2004; Ciamician, 1912; Yoon et al., 2010). With the realization of the issues associated with the use of fossil fuels, photocatalytic water splitting has again become a topic of interest for researchers since the turn of the century, as part of a more general trend pointing towards an increase in the pursuit of solar energy conversion (Kudo and Miseki, 2009).

In the following work, hydrogen production via photocatalytic splitting of water using solar energy as a source is investigated. The photocatalytic reactor is placed inside a cavity receiver atop a solar tower, which receives concentrated sunlight from a heliostat field. The idea is to increase the rate of photons entering the reactor, and to trap the photons in the cavity in order to increase the probability of reactions occurring. The system is hybridized by installing photovoltaic panels inside the walls of the cavity receiver, in order to utilize photons with insufficient energy to cause photocatalytic reactions.

1.4 Motivation and Objectives

Implementation of Hydrogen production from renewable sources is vital if fossil fuel issues to be overcome. Among the hydrogen production methods, solar photocatalytic splitting of water lags behind the others in terms of research and implementation. The infant nature of the process leads to interesting research paths, and provides an opportunity to contribute significantly towards its development.

The specific objectives of the study are listed as follows:

- To build an experimental system that has three main characteristics: it hybridizes a photocatalytic process with a photovoltaic process, subjects the hybridized system to concentrated radiation via a solar tower and cavity receiver system, and allows conduction of continuous flow photocatalytic processes.
- To investigate the effect of pressure, temperature and electrolyte concentration variation on the photocatalytic hydrogen production process.
- To compare the performance of photocatalytic hydrogen production under flow continuous and batch conditions.
- To develop a model based on experiments performed in order to study in greater detail the effect of flow on photocatalytic processes.
- To propose and analyse a large scale system based on the experimental system described, and investigate its performance.

The idea that concentrated solar power is essential in implementation of solar based systems is rarely argued against (Abbott, 2010). So, it follows that the photocatalytic process should also be subjected to such a system if it harbours hopes of being implemented industrially.

By proposing a hybridized hydrogen production system that operates with high efficiency, and attempts to utilize environmental waste, it is hoped that the practicality of such a system will be displayed.

Chapter 2: Literature Review

2.1 Significance of Photocatalytic Hydrogen Production

Hydrogen needs to be produced from a renewable material, using a limitless source of energy, if it is to be part of a sustainable economy. As mentioned earlier, solar energy is attractive as the limitless energy source, due to the sheer magnitude of radiation received on the surface of the Earth (Abbott, 2010).

The attraction of photocatalytic water splitting lies in its potential to be the central process in a highly efficient solar based hydrogen production system of the future. Natural photosynthesis, which is the blueprint for this process, executes its various steps with a remarkably high efficiency, leading to an expectation of a similar level of efficiency for any artificial system that may mimic successfully the reactions of the former (McConnell et al., 2010). The photocatalytic process also provides the most direct route for the solar-to-hydrogen conversion. It combines the harnessing of solar radiation and the transfer of it to the water molecule, two distinctly separate steps in other water splitting systems, into one single process on a macro scale. This allows the potential to minimize irreversibilities that are associated with each component of any engineering process (Sun et al., 2001).

2.2 Obstacles in Photocatalytic Hydrogen Production

The photocatalytic water splitting process for hydrogen production remains very much at the infantile stage of its development. In order to achieve the simplicity touted above, numerous obstacles need to be overcome. Foremost is the fact that several chemical functions need to be integrated into one stable chemical system (Alstrum-Acevedo et al., 2005). At the molecular level, various mechanisms that occur simultaneously, or in succession to one another, need to be

managed and optimized. This requires an innate understanding of the photosynthesis processes that occur in nature, and are the inspiration for this process (Benniston and Harriman, 2008; Ferreira et al., 2004). Effective catalysts that consist of abundant, cheap materials have not yet been discovered or synthesized. Rare elements show good hydrogen production activity, but are not cost effective. Those catalysts that are formulated using common elements do not absorb light effectively in the visible region, which is the major proportion of the solar spectrum (Yoon et al., 2010).

The United States-Department of Energy (US-DOE) has outlines the targets that need to be met in order for photocatalytic hydrogen production to be applicable and acceptable on an industrial scale (U.S. Department of Energy, 2013). Ultimately, a total solar to hydrogen conversion efficiency of 17% is identified as the target. In order to scale the efficiency ladder, research in photocatalytic water splitting is traversing a dichotomous route. One branch of it deals with the issues that pertain to catalyst development, which have been mentioned earlier. The aim is to make a catalyst that is cheap, has a slow degradation time, and works with reasonable efficiency over a significantly large portion of the solar spectrum. The second aspect involves creating systems that enhance the efficiency of the available technology by using it in an optimum manner. This involves performing parametric studies that determine the optimum conditions, experimental procedures, hybridization of different technologies, etc.

2.3 Heterogeneous and Homogeneous Catalysts

Various heterogeneous catalysts are used to split water in a stoichiometric ratio. Maeda et al. (2005) study a solid solution of GaN:ZnO loaded with RuO_2, and achieve an apparent quantum efficiency of 0.14%. Without the RuO_2 loading, no activity is observed. Lee et al. (2007) and Osterloh (2007) report similar results, which show definite photocatalytic activity

under visible light, where the catalyst is composed of abundant elements. Wang et al. (2009) demonstrate a polymeric catalyst, with comparison of different architectures of graphitic carbon nitrides. The best performance by far, though, is demonstrated by Maeda et al. (2008) by using a $(Ga_{1-x}Zn_x)(N_{1-x}O_x)$ solid solution catalyst. Upon loading with $Rh_{2-y}Cr_yO_3$, and post calcination at 823 K, an apparent quantum efficiency of 5.8% is obtained in a wavelength range of 420 – 440 nm.

For hydrogen producing half reactions, metal sulfides are shown to work well in the presence of electron donors. According to Kudo and Miseki (2009), in the presence of sulfide ions as electron donors, their reactions start well but the rate drops off due to the production of disulfide ions. This is overcome by adding sulfite ions to the solution, which prevent formation of disulfide ions. Buehler et al. (1984) demonstrate that CdS is an attractive catalyst for the reaction under visible light due to its narrow band gap. However, it is extremely prone to photocorrosion in the presence of oxygen, which makes it difficult to handle. ZnS does not have the issue of photocorrosion, and shows extremely good quantum yield. Reber and Meier have achieved values of up to 90% for the best samples of ZnS. However, due to its wide band gap, the catalyst is active only under UV light. Since this constitutes such a small portion of the solar spectrum, it is not a feasible catalyst for large scale production.

Yan et al. (2009) use Pt and PdS as a co-catalyst with CdS and show an increase in photoactivity, with an efficiency of over 90% being achieved. However, the status of the co-catalyst as rare metals makes the combination unfeasible. A way of extending the absorption spectra of ZnS into the visible range is by doping it with various metal cations. In separate studies, Kudo and Sekizawa (1999; 2000) investigate the doping of ZnS by Cu and record a quantum efficiency of 3.7% at 420 nm. Tsuji and Kudo (2003) dope ZnS with Pb and observe

some activity under visible light, but not with the same efficiency of Cu or Ni. They also find that co-doping with a halogen element results in comparable activity to Cu and Ni.

Developing solid solutions of metal sulfides is identified as an effective method for band gap reduction. Tsuji et al. (2005) achieve almost twice the yield of Pt loaded CdS using a solid solution of ZnS-$CuInS_2$-$AgInS_2$ in aqueous media. Due to similar crystal structures of CdS and ZnS, they can also be combined in solution, in the form $Cd_{1-x}Zn_xS$. Zing et al. (2006) compare different compositions discover that the best photoactivity is observed when x is set to 0.2. Under visible light, the quantum efficiency is calculated by them as 0.6%, a significant improvement over that of CdS or ZnS alone. del Valle et al. (2009) have reported similar results. Zamfirescu et al. (2013) obtain a quantum efficiency value in the range of 60 – 10% as the batch reaction progresses, and in the same study propose that the efficiency may be maintained at up to 60% under visible light if the concentration of ionic species in the electrolyte is maintained.

Homogeneous catalysts consist of complex molecular structure where different aspects of water splitting, such as photosensitization, charge separation and charge transfer are conducted by different specialized parts of the molecular structure. As compared to heterogeneous catalyst, their homogeneous counterparts are not to be found in literature as much. While a few studies show the catalytic evolution of oxygen, hydrogen production mainly remains elusive (Duan et al., 2010; Limburg et al., 1999; Yagi and Narita, 2004). Only Heyduk and Nocera show successful production of hydrogen (2001), and most recently, a group of researchers demonstrate hydrogen production on a Ru, Rh, Ru type molecular device (Elvington et al., 2007). Homogenous catalysts are an attractive proposition for water splitting, but the research still remains at a very basic stage.

2.4 Photocatalytic Systems

In parallel with the research that is going into developing better functioning catalysts, finding out new ways of implementation of the existing technology is also essential. Discovery of a new catalyst is not likely to require a complete overhaul of a system designed for maximum efficiency, but more likely a substitution of the said catalyst and minor modifications.

One way to achieve overall water splitting is by using a Z-scheme system. This employs a hydrogen evolution catalyst and an oxygen evolution catalyst, with an electron mediator as a link between the two. This system allows the use of photocatalysts whose band gap is suitable only for half reactions, and thus allows usage of a greater proportion of the solar spectrum. Another advantage is that these systems allow evolution of hydrogen and oxygen in separate sites, and thus remove the obstacle of gas separation before collection. This also leads to a safer process, as it prevents the flammable composition of hydrogen and oxygen, and at the same time prevents back reaction to form water. An issue with the Z-scheme is that the redox cycle of the mediator challenges the reduction or the oxidation of water at the hydrogen and oxygen evolution sites (Kudo and Miseki, 2009; Maeda, 2011). Tabata et al. (2010) use $Pt/ZrO_2/TaON$ as a hydrogen evolution catalyst in combination with Ta_3N_5 modified with Ir and $R\text{-}TiO_2$ as an oxygen evolution catalyst. IO_3^-/I^- is used as a shuttle redox mediator. The $R\text{-}TiO_2$, without which photocatalytic activity is not observed, is able to suppress the adsorption of I^- on the oxygen evolution site, thus allowing a two-step cycle to be completed. Maeda et al. (2011) use the same hydrogen evolution catalyst in combination with TaON that is loaded with ruthemium (Ru), and manage to observe photoactivity, which is not the case with unloaded TaON. Sasaki et al. (2009), meanwhile, successfully demonstrate a z-scheme system by using $Ru/SrTiO_3$ and $BiVO_4$ as hydrogen and oxygen evolution catalysts respectively, in which an electron mediator is not

required. The results indicate that an inter particle electron transfer occurs between the two catalysts.

A key aspect in optimization of solar energy conversion systems is by hybridization of different technologies. Due to the large variation in the energy levels of the solar spectrum, hybridization has the potential to significantly enhance the performance as compared to stand alone systems because different solar energy conversion technologies use different portions of the spectrum. Sarria et al. (2005) provide the earliest example of a hybridized photocatalytic system in their attempt to combine a photocatalytic water decontamination system and a photovoltaic (PV) system for simultaneous power output. Since the system deals with water decontamination instead of water splitting, a performance parameter is not given. The study instead focusses on the retardation in the performance of the PV system when a photocatalytic reactor is situated directly in front of the PV panel. They discover that the performance of the PV does not degrade significantly. Vivar et al. (2010) expand on the same concept in another study, and discuss the viability of various global locations for a pilot plant, along with conceptual designs for such a reactor. Kribus and Mittelman (2007) study a poly-generation system with PV and solar thermal energy conversion, with consideration given to various paths for the use of the thermal energy. The authors compare the cases where the waste heat from either primary device is used to run a heat engine, as direct thermal use, or for absorption cooling. In all cases, the performance for the polygeneration of the heat engine is better than the PV, and it is shown that concentration of the solar radiation improves the results in all cases. Joshi et al. (2009) investigate the thermodynamic performance a PV-thermal system, and compare it to a PV system. The exergy efficiency of the hybridized system increases from a maximum of 13% to 16% over the standalone PV system. Baniasadi (2013) investigates with a system that combines

a photocatalytic process with a light based proton pump, and finds a 25% increase in the exergy efficiency. The same author proposes a design with a photocatalytic chamber containing ZnS followed by a second chamber containing CdS. The ZnS, which has a high band gap absorbs the high energy radiation and allows the rest to pass through to be absorbed by CdS. Most recently, Zamfirescu et al. (2013) propose a theoretical scaled up system that hybridizes photocatalytic and PV processes. The solar spectrum is categorized as upper, middle and lower spectrum to correspond with usage for photocatalytic, PV-electrolysis, and thermal conversion systems.

As it can be inferred, the literature regarding the hybridization of photocatalytic hydrogen production systems with other systems is not very comprehensive. This study attempts to add to that body of literature, by combining concepts extracted from the work of Baniasadi (2013), where a concentrator system is suggested, and the work of Zamfirescu et al. (2013), where the hybridization of a photocatalytic and a PV system is suggested. The hybridized system is placed in a solar tower reactor, and an experimental and theoretical assessment is performed.

Chapter 3: Background

3.1 Water Splitting

Among the hydrogen containing resources available in the environment, water is the most abundant. The splitting of water into its constituents is energy intensive and is a non-spontaneous process, except at temperatures that are greater than 4500 K. At standard conditions, a minimum of 237 kJ of energy needs to be supplied in the form of work in order to split one mole of water (Chen et al., 2010) as follows:

$$H_2O \rightarrow H_2 + \frac{1}{2}O_2 \tag{3.1}$$

A certain proportion of energy is also absorbed in the form of thermal energy. As the process temperature is increased, the system requires a smaller amount of work input and a greater proportion of thermal energy (Tsutsumi, 2008).

Solar water splitting is when the required energy is taken from the Sun. Any of various methods may be used to harness this solar energy for the desired reaction. The methods of solar water splitting may be classified as electrolytic, photocatalytic, thermochemical, direct thermal decomposition, and biological production (Das and Veziroğlu, 2001; Dincer and Zamfirescu, 2012). Among these, the photocatalytic method provides the most direct route of energy transfer from the Sun into hydrogen (Baniasadi, 2012). This method is often termed as artificial photosynthesis, due to its similarity to the photosynthesis process of green plants where they split water to produce sugar (Kudo and Miseki, 2009). Its directness is an attractive feature as it allows the potential of minimization of energy loss caused by increasing steps within processes.

The work of Fujishima and Honda (1972) introduces the concept of using inorganic semiconductor particles to harness solar energy and use it to split water molecules.

3.2 Photocatalytic Water Splitting

A majority of the energy from the sun is in the form of visible light. The aim is to harness this energy, and use it to produce hydrogen from water. This is an attempt at energy storage, in the form of hydrogen. Water, however, does not absorb energy in the visible and the near ultraviolet (UV) range. This issue may be overcome by the presence of semi-conductor catalyst dissolved or suspended in water, that have the ability to capture the energy in the elusive region and transmit it to the water molecules.

Though similar in nature, a distinction may be made between systems that consist of dispersions of colloidal catalyst in water, and systems that comprise of semi-conductor catalytic material suspended in water in the form of electrodes, and connected electrically. The latter system is classified as a photoelectrochemical (PEC) system, while the former system falls under the category of photocatalysis, and is studied at in detail in this section (Wang et al., 2012).

An incoming photon of light comes into contact with a semi-conductor particle, and is absorbed. Semi-conductors have an electron structure where a band gap separates the conduction band (CB) and the valence band (VB). The absorption of photons by the particle translates its energy to an electron in the valence band, which is now able to jump to the conduction band. The catalyst is now in an unstable form, and it may revert back to its stable form by either losing the high energy electron to a reaction, or by losing energy as heat as the electrons falls back onto the valence band. While in this unstable state, the semi-conductor particle becomes a potential active site for a reduction reaction. If the electron is successfully lost to a reaction, then the catalyst

must gain back an electron in order to remain in equilibrium. Hence, a secondary active site is developed on the semi-conductor particle where an electron may be gained by a potential oxidation reaction (Kudo and Miseki, 2009; Maeda and Domen, 2010). The generic process is described in Figure 3.1 for any type of colloidal semi-conductor catalyst.

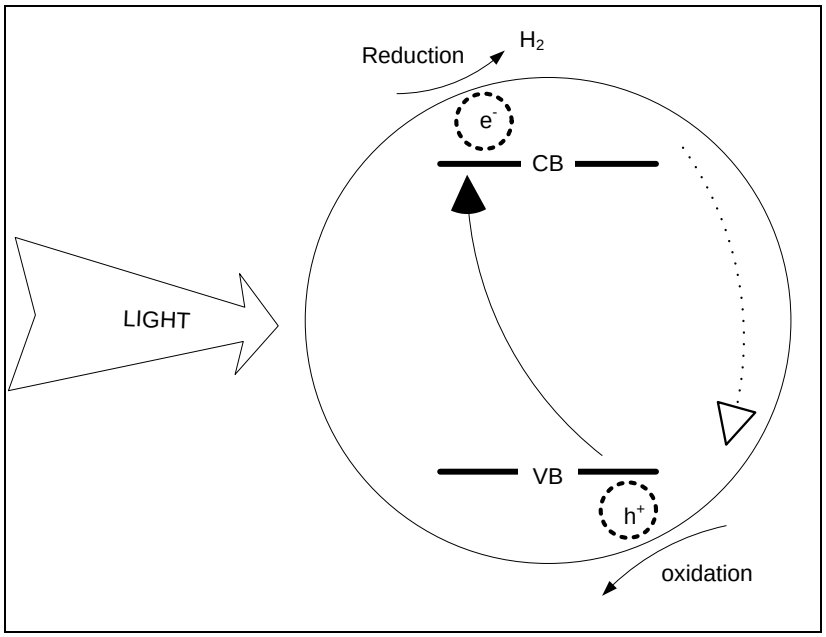

Figure 3.1: Description of the basic photocatalytic water splitting process.

In the case of water, the following reduction and oxidation reactions occur at the active catalyst site (Maeda, 2011):

$$2H^+ + 2e^- \rightarrow H_2 \tag{3.2}$$

$$H_2O + 2h^+ \rightarrow \frac{1}{2}O_2 + 2H^+ \tag{3.3}$$

The minimum energy theoretically required for splitting water is 2.46 eV (1.602×10^{-19} j) for each molecule of hydrogen produced. Since the production of each hydrogen molecule requires two electrons, the process requires two photons having energy of 1.23 eV each. This corresponds to about 70% of the solar spectrum, indicating a significantly high harnessing

potential (Baniasadi, 2012). However, the catalyst requires a certain amount of energy, equal to its band gap, before it activates. Photons with energy less than the band gap are not successful, even if their energy is greater than the 1.23 eV required for the production of a hydrogen molecule. For a system to incorporate the full, stoichiometric, water splitting reaction, the band gap of the catalyst must be such that the bottom level of the conduction band is more negative than the reduction potential of the reaction in Eq. 3.2, while the top level of the valence band is more positive than the oxidation potential of Eq. 3.3 (Kudo and Miseki, 2009).

The water splitting process may involve only a half reaction, in suitable ionic solutions. Though mainly used for evaluating catalysts, these reactions do not have to be limited to this end. They provide the potential for a two-step, or a Z-scheme, photocatalytic system that involves the use of two separate but interlinked reactors in which a reduction and oxidation processes occur separately. These systems involve a third reaction, involving an electron mediator, where the product of oxidation occurring at the hydrogen evolution cell is reduced at the oxygen evolution cell (Maeda and Domen, 2010). Conversely, a half reaction cell may be used for hydrogen production, with the product of oxidation being further processed to obtain a useful output. Another advantage of these half reaction systems is that it negates the issue of separation of hydrogen and oxygen that is encountered in a full photocatalytic system.

3.3 Solar Tower

Despite the abundance of energy in solar radiation incident on the earth, a few barriers remain that hinder its widespread use. One issue is the low radiation per unit of earth surface. For the power and heating needs of a detached, single family, North American home, 50 – 100 m^2 of non-shaded area must be used for photovoltaic-thermal systems (Zamfirescu et al., 2013). Therefore, collecting this low density solar energy becomes a main engineering task for high end

applications, such as power plants. This is achieved by concentrating solar radiation using appropriate reflective material to produce high temperatures, which may then be used for generating electricity using conventional power plants. Concentrated solar power (CSP) systems may be classified as either line concentrating systems or point concentrating systems. Line concentrating systems are generally easier to handle, but point concentrating systems provide a higher concentration of light (Müller-Steinhagen and Trieb, 2004). Line concentrating systems include parabolic trough collectors, compound parabolic collectors, and Fresnel trough collectors, while point concentrating systems include parabolic dish collectors and solar tower receivers (Dincer, 2011).

A solar tower system works by using mirrors called heliostats to reflect light and focus it at a desired point, where it is incident upon a receiver mounted on a tower. The mirrors are small relative to the height of the tower, and typically involve a two-axis tracking system to follow the path of the Sun. A basic diagram of a solar tower concept is shown in Figure 3.2.

Certain factors place a limitation on the performance of these systems from an optics point of view. These are shading, blocking, and the cosine effect. Shading occurs when one heliostat interrupts the light rays from falling on to another heliostat. This effect is prevalent in heliostats close to the tower, and results in a dilution of the direct radiation being reflected onto the tower receiver. Blocking occurs when the path of reflected rays is blocked by an adjacent heliostat. This phenomenon affects the heliostats that are further away from the tower, and results in a decrease in the quantity of radiation reflected onto the receiver.

The cosine effect refers to the reduction in the usable surface area of the heliostats due to their angled orientation. The effective area is the unshaded and unblocked area multiplied by the

cosine of the angle between the solar vector and the normal to the heliostat surface. These factors need to be optimized when considering the design of a heliostat field (Schramek and Mills, 2003).

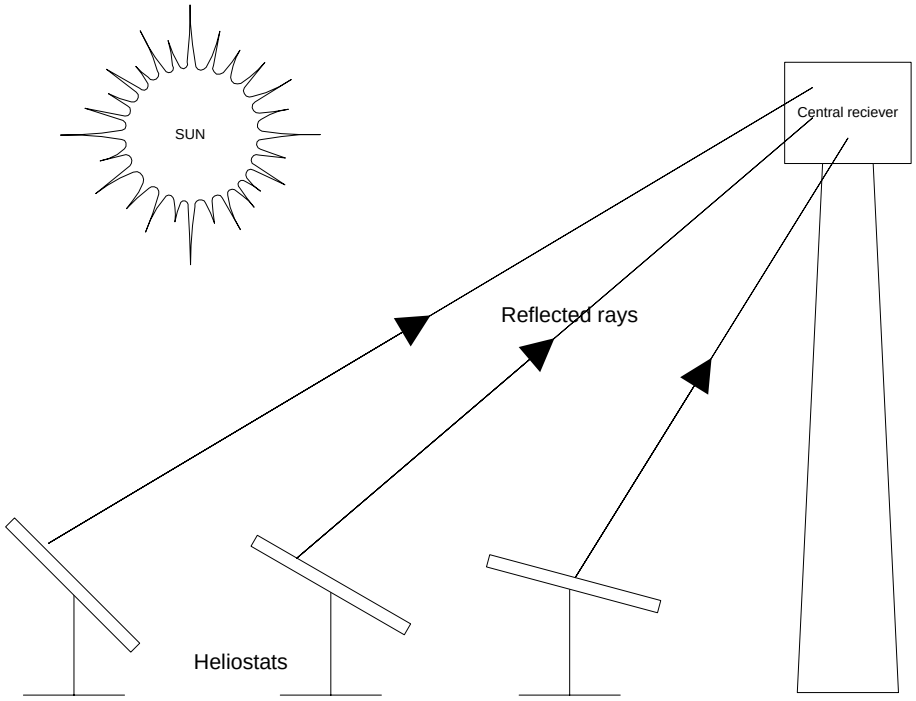

Figure 3.2: Solar tower receiver system.

3.4 Photovoltaic Systems

A photovoltaic device is defined as one whose conductivity is strongly enhanced due to excitation of electrons upon incidences of photons onto it. The excited electrons move in the potential that is created by an appropriately arranged p-n junction. The electrons flow from the n junction to the p junction, due to the relative densities of electrons present in the conduction band of each junction. The energy of the incident photon must be equal to or greater than the difference between the conduction band and valence band of the p type material. The efficiency of a solar cell is defined as

$$\eta = \frac{W_E}{I} \tag{3.4}$$

where η is the efficiency, W_E is the electrical work output from the solar cell, and I is the incident radiation flux. The efficiency is less than 1 due to various factors. The photons of energy less than the band gap are wasted, as mentioned above. Also, the useful photons may contain energy above the band gap that is also wasted, because of the discrete nature of the energy of photons. Another important factor is that the cell voltage needs to be some value below the maximum voltage (open circuit voltage) in order to obtain a finite current (Sorensen, 2011).

The general shape of the characteristic curve is shown in Figure 3.3. Parameters V_{OC}, I_{SC}, V_M, I_M indicate respectively the points of open circuit voltage, short circuit current, voltage at maximum power, and current at maximum power. The maximum power for an ideal cell is the theoretically achievable maximum value. Attempting to achieve anything greater than that would be akin to getting work output from an engine with efficiency greater than the Carnot efficiency. The quality of any solar cell can then be quantified as a ratio of the maximum power to this fictitious maximum power if the cell could be run at the open circuit voltage and short circuit current.

$$FF = \frac{V_M \times I_M}{V_{OC} \times I_{OC}} \tag{3.5}$$

Two major factors that cause the shape of the real characteristic curve to be different from the ideal curve are the series resistance and the shunt resistance. Ideally, the series resistance is 0 and the shunt resistance is infinity. Figure 3.4 shows the behaviour of the curve as the series resistance becomes greater than 0. Figure 3.5 shows the curve behaviour when the shunt resistance decreases to a value less than infinity (Markvart and Castañer, 2012).

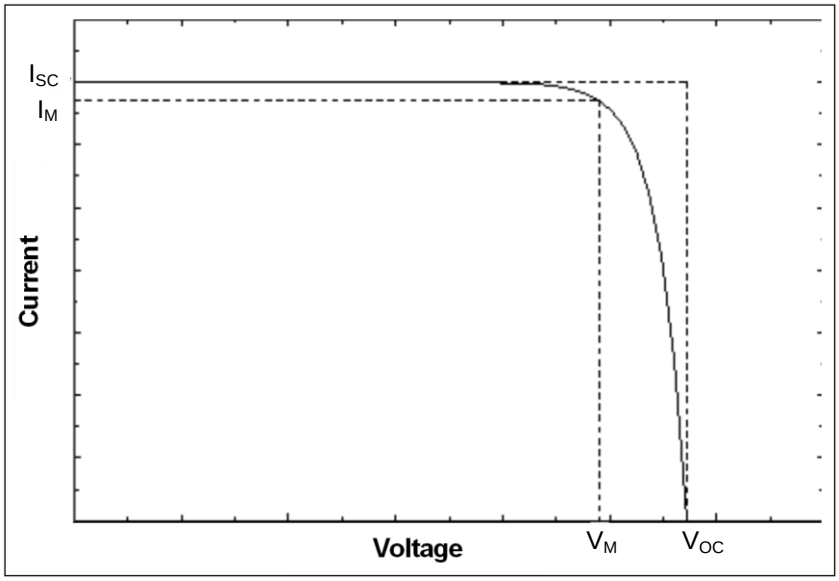

Figure 3.3: PV characteristic curve. (Adapted from Markvart and Castañer, 2012).

Solar cells are combined in arrays to obtain desired voltage and current values for a system. For identical cells under equal solar irradiance, the following simple assumptions may be made in order to obtain a characteristic curve: for cells in series, the voltage is directly multiplied by the number of cells; for cells in voltage, the current is directly multiplied by the number of cells (Golder, 2007).

The solar irradiance on each cell, however, may not always be equal. This may be due to shadows from surrounding objects, as the Sun moves along its path. The output may be reduced due to shading, but in some extreme cases, the shaded cell may act as a sink for the power produced by the un-shaded cells. To avoid this, cells in series have diodes installed in parallel with a forward bias, which are called bypass diodes. Whole strips of cells that are in parallel each have a diode in series with the strips. This prevents the strip, if dark, from becoming a sink for the current. This is called a blocking diode (Bremner, 2009).

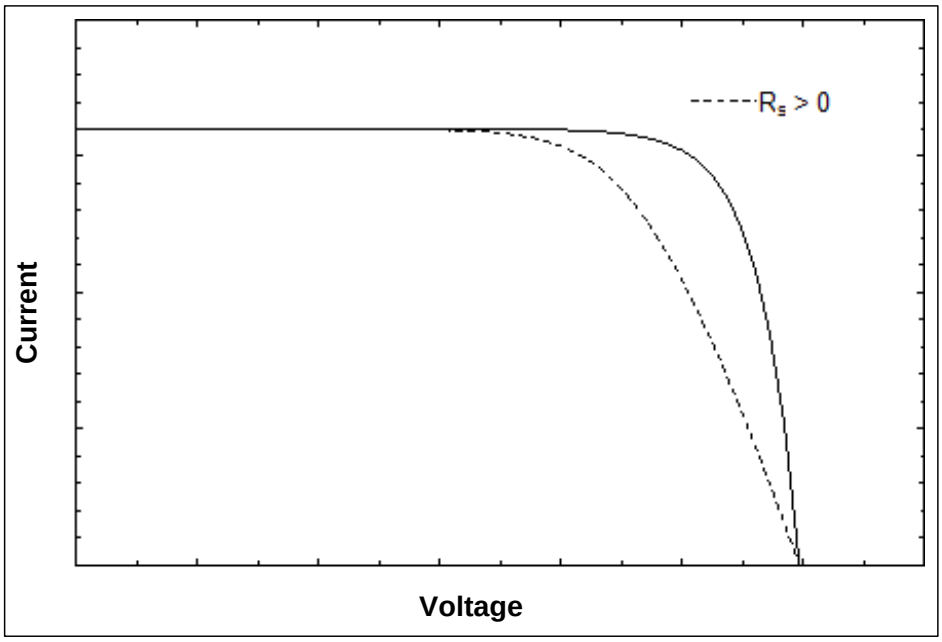

Figure 3.4: PV characteristic curve with series resistance greater than 0 Ω (Adapted from Markvart and Castañer, 2012).

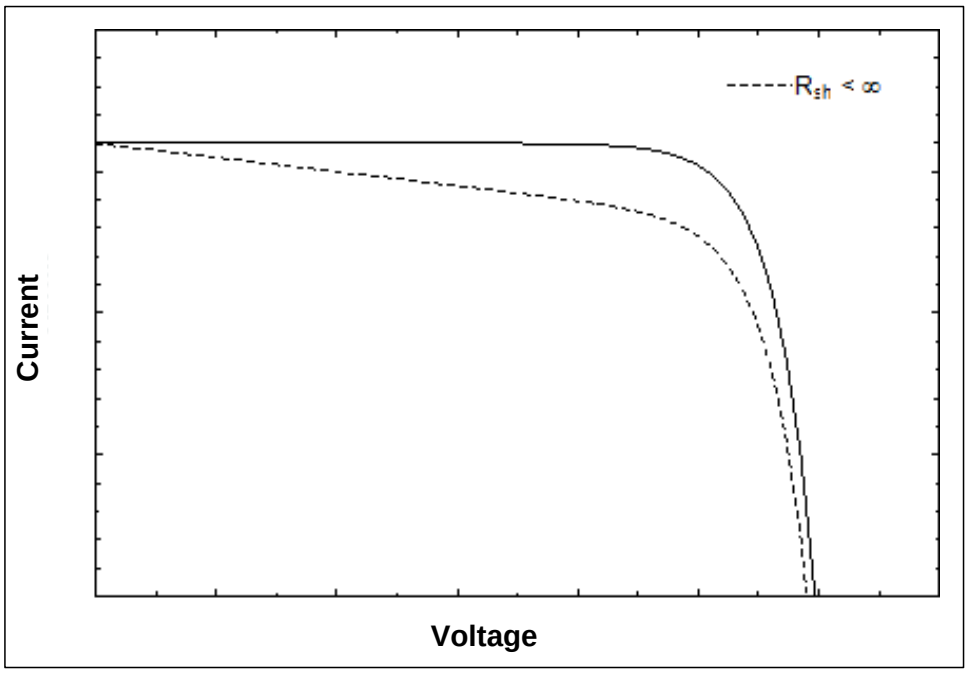

Figure 3.5: PV characteristic curve with shunt resistance less than infinity (Adapted from Markvart and Castañer, 2012).

Chapter 4: Experimental Apparatus and Methodology

In order to analyse the performance of the photocatalytic system, a certain number of experiments are performed that allow the extraction of valuable parameters for a theoretical study. An existing photo reactor previously designed and built by a senior year undergraduate group at UOIT is customized to allow for the reactions intended here. The apparatus is described here, with a highlight of the key modifications made. Certain crucial accompanying experimental procedures are also outlined, and the experimental methodology touched upon.

4.1 Basic Photoreactor

The reactor comprises of a tubular reaction vessel made of thin glass, which contains an immersed thermocouple and two electrodes. An electronically controlled cylinder is attached to the reaction vessel, which allows the photoreactor to operate in constant volume or constant pressure mode. For constant volume processes, a pressure transducer gives the output, which is the increase of pressure due to hydrogen production. For constant pressure operation, the transducer communicates with NI labVIEW which in turn controls the motor of the piston-cylinder through a data acquisition device. A digital caliper is attached to the piston which allows the height increments to be recorded, and thus the determination of the volume of gas produced. The schematic of the basic is given in Figure 4.1.

The reaction vessel has a liquid volume capacity of 100 ml. The piston cylinder device can store a volume of gas up to 50 ml. For the existing reactor, input light is supplied by four stacks of five LEDs on four sides of the reaction vessel, totalling 100 W. The solution is stirred by means of a magnet attached below the reaction vessel, and a magnetic stir bar placed inside the vessel.

Part no.	Part name
1	Reactor stacking assembly
2	LED and heat sink assembly
3	Reaction vessel assembly
4	Gas collection assembly
5	Electrical control box
6	Servo-motor assembly
7	Reactor housing
8	LED attachment screws
9	Piston track assembly

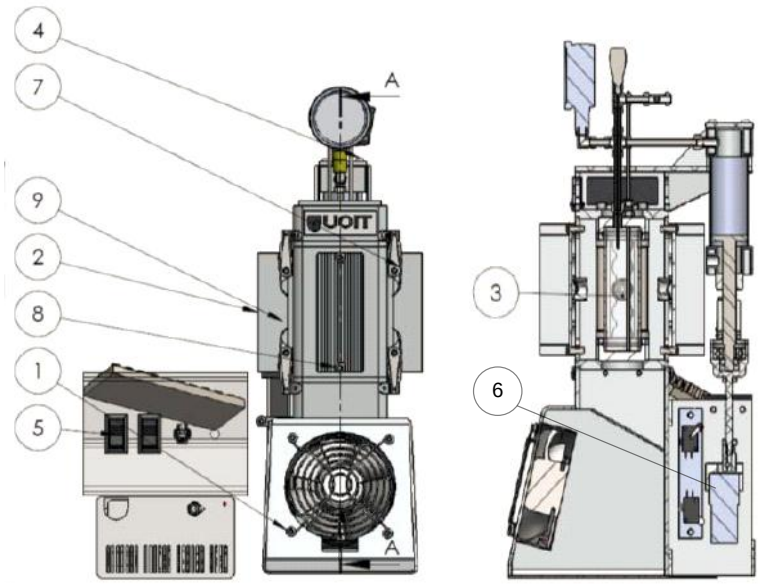

Figure 4.1: Schematic of UOIT photoreactor (Chagani et al., 2011).

4.2 Reconfiguration of Reactor Setup

The reactor needs to be modified in order to perform the experiments required. These modifications include design of a platform for solar tower setup, installation of a catalyst retainer, implementation of flow of electrolyte, and hybridization with PV cells.

4.2.1 Design of Platform

A solar tower involves a collection of heliostats that focus light over a desired area. Any change in the location of the illuminated area or the heliostats would require a re-calibration of the mirrors. As the solar simulator is used for various multiple experiments in parallel, leaving the set-up for a long duration under the solar simulator is not a plausible option. A platform is designed that allows the position of the reactor to be fixed relative to the heliostats and the solar simulator and which allows the set-up to be removed and re-installed repeatedly.

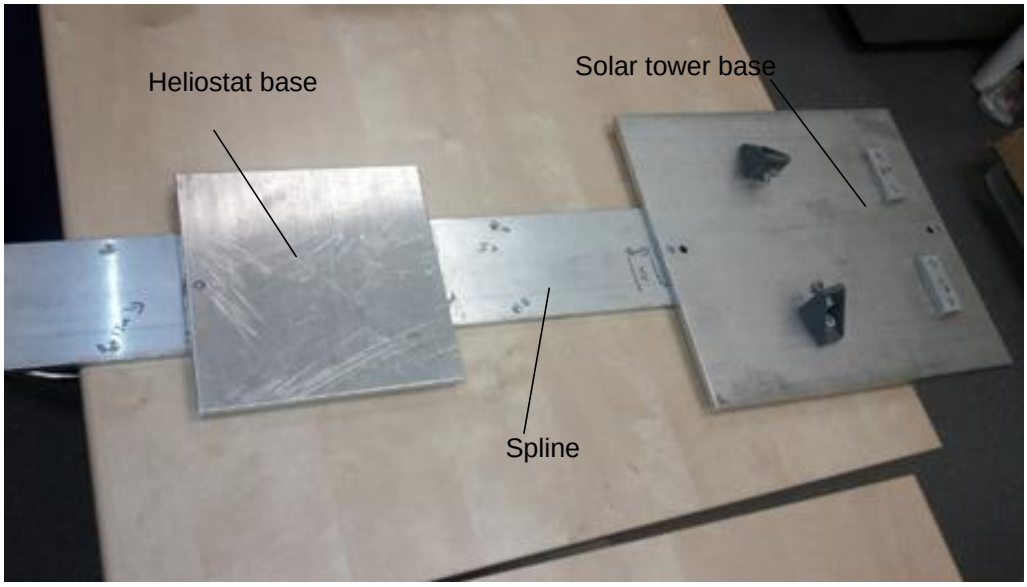

Figure 4.2: The platform for the solar tower assembly.

The platform is shown in Figure 4.2. It consists of a spine, a heliostat base, and a reactor base, all made out of thin aluminum blocks. The spine sits under the solar simulator in a fixed position. Tapered screw heads, which attach the spine to the simulator frame, allow the spine to be installed at exactly the same spot repeatedly. The heliostat base and the reactor base are screwed onto the spine. The reactor base has guides that allow the reactor to sit in one fixed spot repeatedly. An aluminum leg sits under the end where the reactor base is, in order to support the weight of the reactor. The platform allows the setup to be lifted and stored away from the solar simulator when not in use, without having to adjust any settings.

4.2.2 Heliostats

For solar tower systems, solar radiation is concentrated by using small mirrors (relative to the tower) that are arranged on a flat plane based on the movement of the Sun. The heliostat field position is optimized in order to obtain the largest possible amount of radiation for a period of time, which may be to the order of months or years. This results in an arrangement that may not be the most efficient at a given instance in time, but is beneficial over a longer range of

evaluation. For this study, however, the characteristics of the light input are not varied, including variation of incident angle. Therefore, the most suitable heliostat pattern is a circular pattern focussed towards the cavity receiver, with the radius of successive rows adjusted to avoid blocking and shading of light, as shown in Figure 4.4.

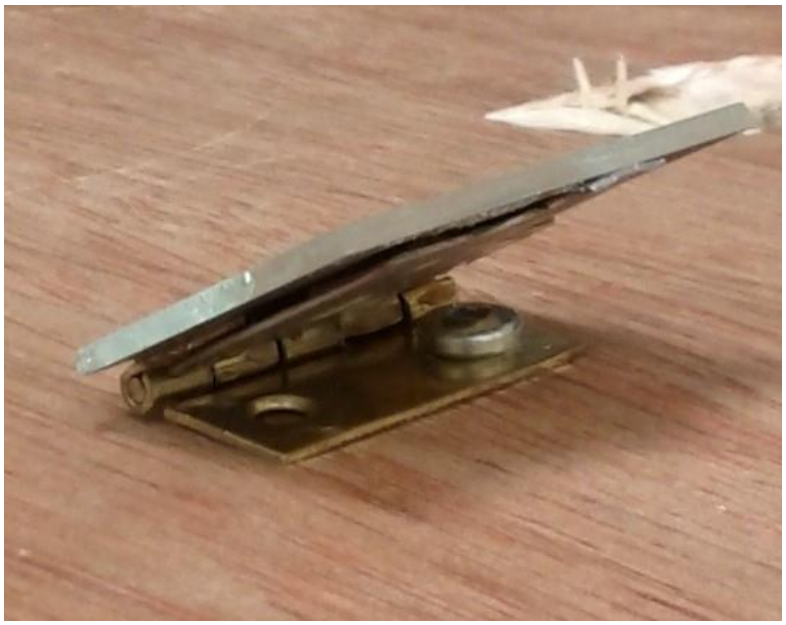

Figure 4.3: Heliostat shown mounted on its adjustable base.

Heliostats are designed by cutting small 30 mm square pieces from a household silver mirror. For each individual heliostat, an adjustable stand is designed using small brass hinges. The hinge is compressed in a vice to make it rigid, so that it may be adjusted to focus the reflected light beam in the vertical direction. Then the hinge is attached to the heliostat base using a single screw that allows adjustment of the light beam in the horizontal direction. Heliostats are mounted on the base using a heat resistant adhesive. Once the heliostats are calibrated, an adhesive is applied to each stand to fix the position. A heliostat mounted on its stand is shown in Figure 4.3. The base of the heliostat field is covered by non-reflective material in order to absorb the incident light that is not reflected by the heliostats.

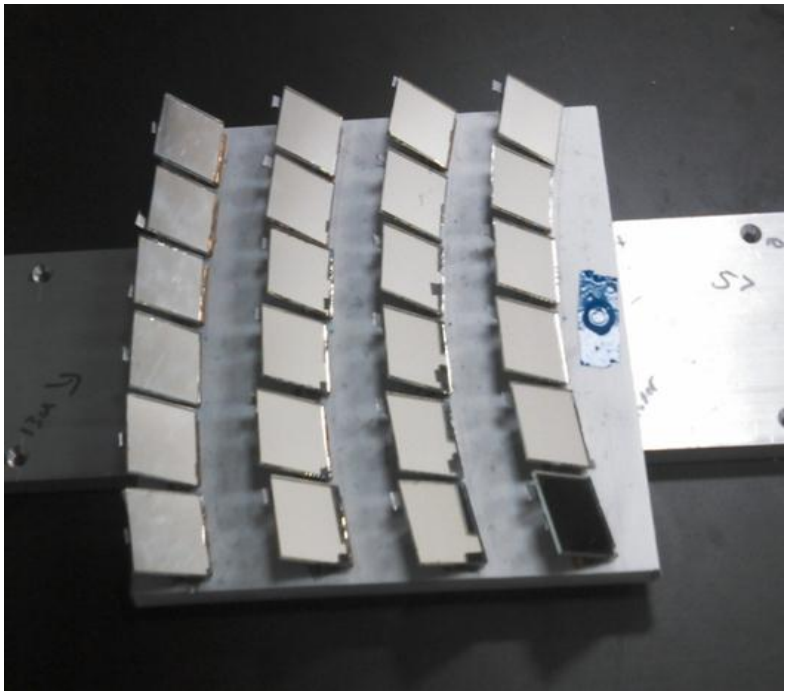

Figure 4.4: The completed heliostat field.

4.2.3 Installation of Photovoltaic Cells

The solar cells need to be installed in a manner that does not change the status of the photocatalytic process as the primary process. The cells, therefore, must not interfere with light incident on the photocatalytic reaction vessel, but should harness the radiation that is unused by the photocatalytic process. The size of the PV cells is an important factor to consider since a smaller size provides greater flexibility in fitting the greatest number of cells within the constraints of the existing reactor design. The cells may not be attached directly to the walls of the reaction vessel housing due to three factors:

- Electrical wires are soldered to the PV cells. If the cells are attached directly to the walls of the housing, that would create a requirement to drill holes in housing. The present condition of the reactor is to be maintained, so no irreversible changes can be made to the reactor.

- The simplest method of attachment of the cells is to glue them on to a surface. Again, this causes damage to the reactor housing. It also hinders any changes that are required in the positioning of the solar cells due to the permanency of the fixture.
- The cells under operation experience some heat loss. Creating a gap between the reactor housing and the solar cells allows passage of forced or natural air through the gap, aiding in the transfer of heat away from the cells.

A plate is designed, on which the PV cells are attached, as shown in Figure 4.5. The cells are glued onto the plate, and the plate screwed onto the reactor housing using existing holes in the housing. Short wire pieces are soldered onto the cells, which gives the flexibility of later creating various desired series and parallel combinations of the PV cells.

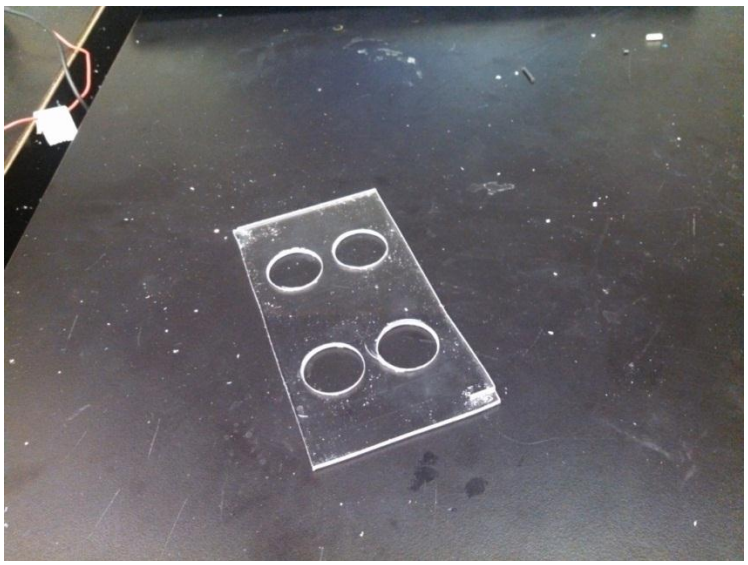

Figure 4.5: Duraplex plate for PV module.

Electrical wires are soldered onto the PV cells. Single core copper wires are selected for ease of soldering. A plate is created using high impact Duraplex plastic, on which the solar cells are attached to create a module. Each plastic plate has two cells in a column, and a total of three

columns. The holes in the plastic sheet are for the electrical wires to pass through. Small rectangular plastic pieces cut form the same sheet are attached at the top and bottom end of the plate. These are drilled and threaded, to be used as points of attachment of the plate to the reactor housing. The PV cells are glued onto the plate. Positive wires are red and the negative ones are black. The module is screwed onto the housing. Figure 4.6 shows these attached modules.

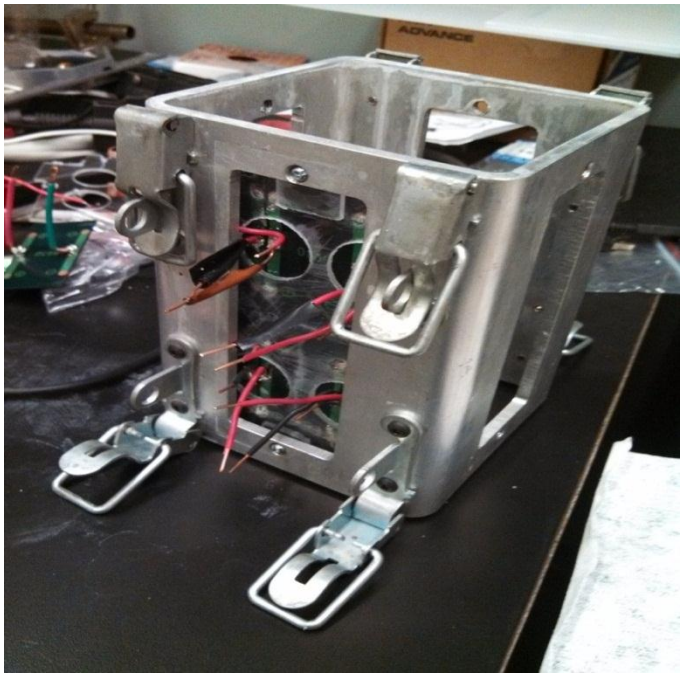

Figure 4.6: PV module attached to the reactor housing.

Three sides of the reactor housing are fitted with the cells. The back end has regular modules with six flat panels. However, due to size constraints, the modules at the sides need to be slightly modified. The column of PV cells at the end of the module is aligned at an angle in order to fit it in. Pieces cut form steel strappings are used to align each PV cell at the required angle. Figure 4.7 shows the steel strapping cut and shaped to provide the desired alignment, and Figure 4.8 shows the side PV module.

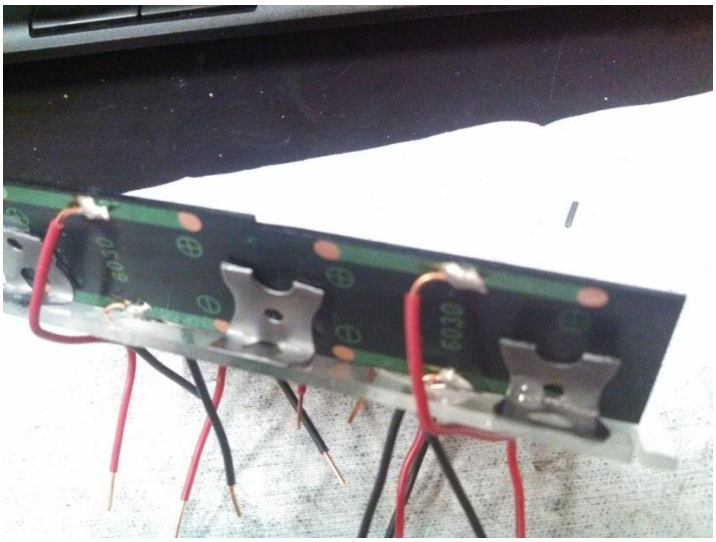

Figure 4.7: Steel strapping used to provide desired tilt to the PV cells.

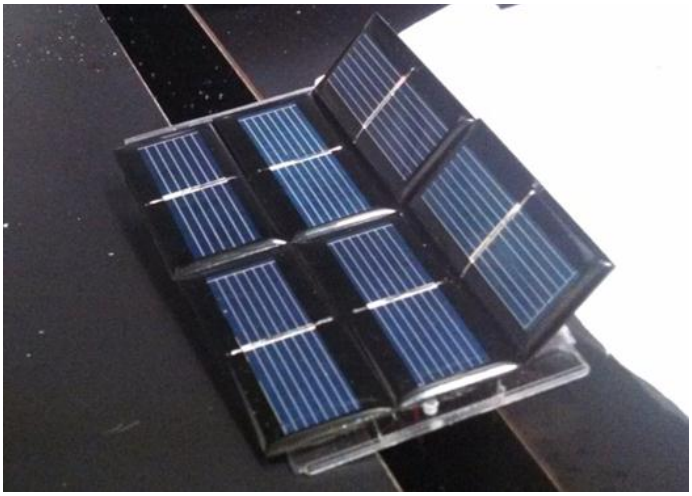

Figure 4.8: PV modules with tilted row of cells to accommodate for space.

Figure 4.9 shows the completed design for the retro-fitting of the aluminum reactor housing in order to determine the effect of PV hybridization on a photocatalytic process.

4.2.4 Cavity Receiver

The installation of the photovoltaic panels essentially creates a cavity receiver. The cavity receiver increases the efficiency of a system on the premise of trapping the photons inside the cavity. Since all exit routes are closed off for photons, the incoming photons from the window in Figure 4.9 above have to be used by any one of the three processes occurring simultaneously. If

the photon manages to avoid entering the photoreactor, it is then absorbed by the PV cell. Failing that, it is used for direct thermal usage for either hot air or hot water. In this case, the top of the reactor housing is not closed and provides an escape route for the photon, but it is not desirable to close it off due to a need for air flow.

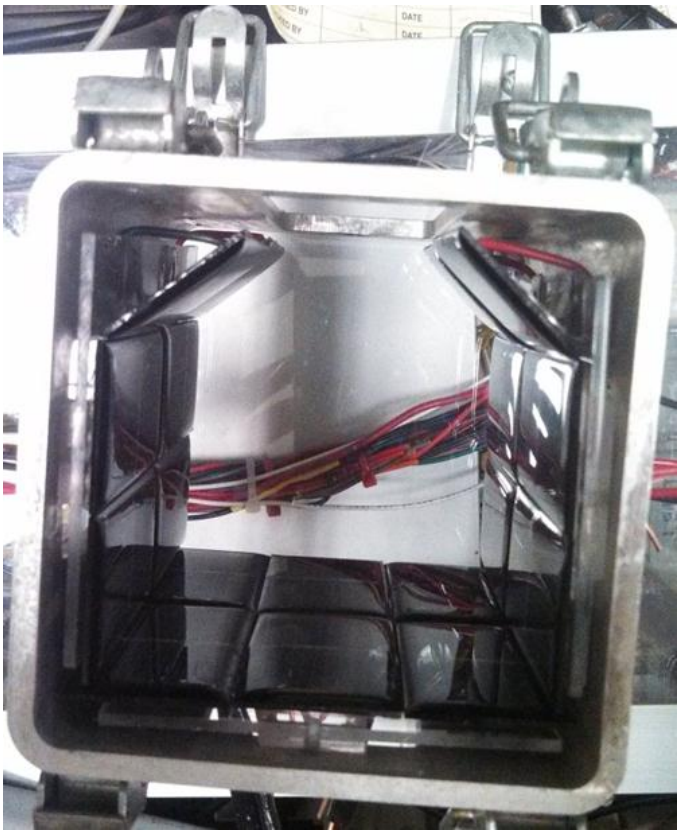

Figure 4.9: Completed reactor housing assembly.

4.2.5 Isolation of Reaction Vessel

For the reasons explained later in section 4.3, there is a need to isolate the reaction vessel from the main photoreactor body without exposing the contents of the reaction vessel to the environment. For this reason, the existing configuration of steel tubing that connects the reaction vessel to the piston cylinder is modified and a valve is attached that can be closed off to allow the detachment of the reaction vessel from the main reactor body.

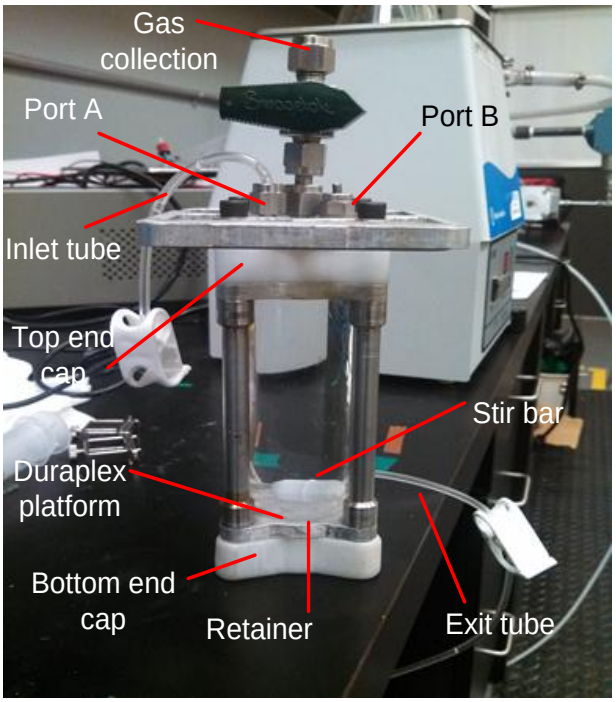

Figure 4.10: Isolated reaction vessel with bottom filtration.

The isolated reaction vessel is shown in Figure 4.10. The main reactor body is shown in Figure 4.11 in place under the solar simulator. The reaction vessel is inserted into the cavity receiver from the top, the photoreactor head unit is rotated to bring it into place, and latched to the body. The flex tube allows ease of assembly and disassembly, and the valve shown in Figure 4.10 allows the hydrogen collected in the piston cylinder device to be purged mid-experiment. During purging, the valve attached to the reaction vessel is closed off to prevent exposure to the environment, while a second valve attached directly to the cylinder is released and the piston returned to the zero position via an electronic switch.

4.2.6 Flow Tubes and Retainer for Continuous Operation

In order to allow the photoreactor to handle continuous flow processes, the reaction vessel is retro-fitted with a flow inlet for the fresh solution, an outlet for the used solution, and a catalyst retainer to maintain the colloidal catalyst inside the reactor.

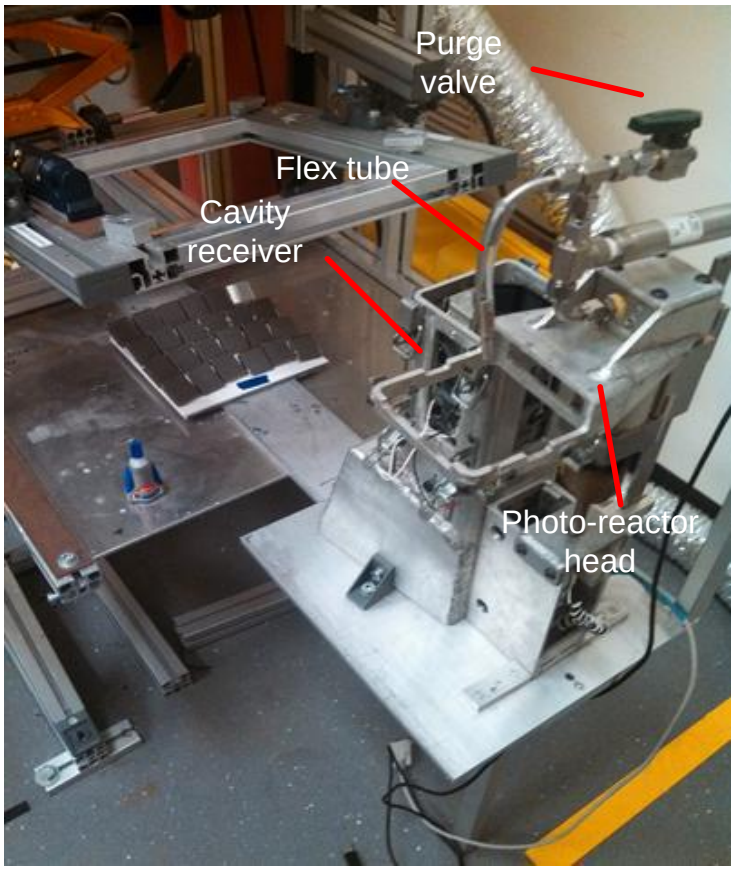

Figure 4.11: Main reactor body.

The reaction vessel consists of a glass tube, with two end caps on either end made of polymeric material. The first design involves a retainer installed at the bottom of the vessel, and the exit tube connects to a hole drilled through the bottom reactor cap. The setup is shown in Figure 4.10. Since the magnetic stir bar needs to sit on the membrane, a circular Duraplex disk is fitted above the membrane, so that damage to the membrane is avoided due to the motion of the stir bar. The two electrodes present in the original reaction vessel are removed, and the inlet tube is fitted to one of the newly available holes (port A). The other hole left vacated by the removal of the electrode (port B) is closed off. This idea is unsuccessful in its implementation. Due to the presence of the Duraplex platform fitted above the membrane to prevent wear to the membrane, a gap is created between the membrane and this disk. The colloidal catalyst is of an extremely

small size, and tends to get caught up in that gap. A significant catalyst loss is observed. It also results in the formation of cake on the membrane, and thus blockage of flow.

To avoid this issue, the new retainer design entails a tube entering from port B and extending close to the bottom of the reactor. Attached to the end of the tube, and floating in the electrolyte solution, is installed the retainer with the membrane, facing downwards. After test runs, almost no catalyst is observed to have accumulated on the membrane, and smoother flow is observed during experiments. Figure 4.12 compares the two filtration schemes. 4.12 (b) shows the scheme finally implemented successfully. Figure 4.13 shows the retainer with the reaction vessel inside the cavity receiver. The catalyst is visually observed accumulated on the exit tube connected to the retainer, but not on the retainer itself.

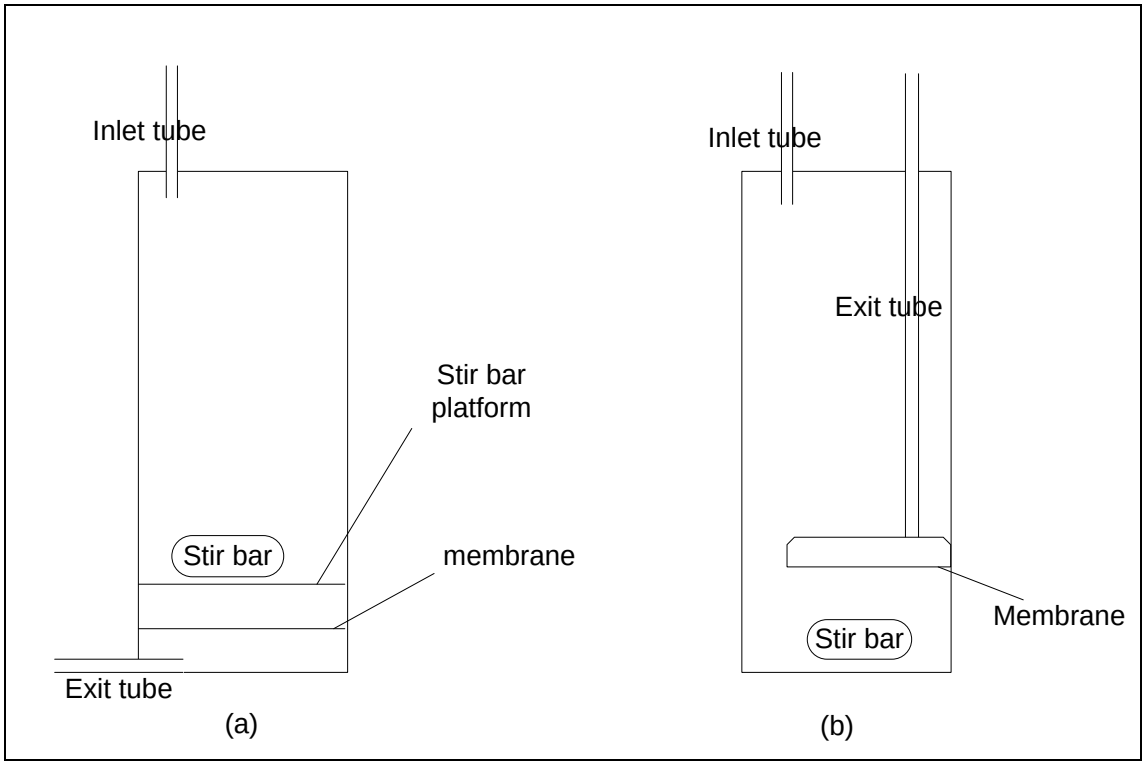

Figure 4.12: Filtration schemes for retaining catalyst inside the photoreactor.

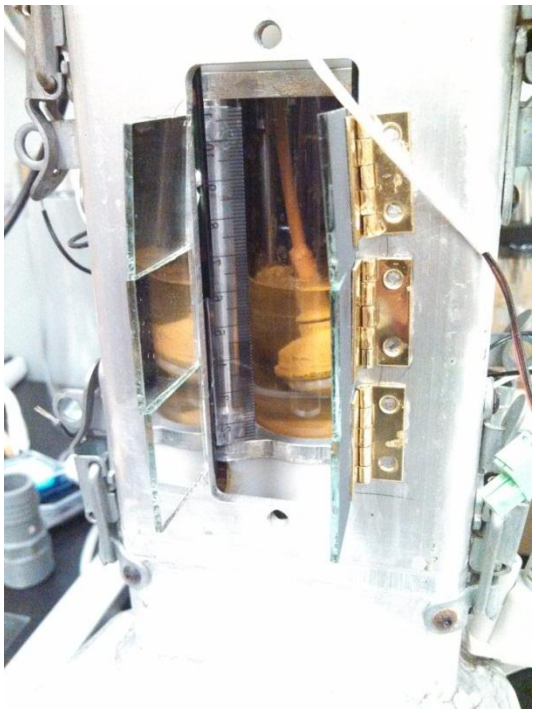

Figure 4.13: The retainer shown inside the photoreactor with the colloidal catalyst.

4.3 De-aeration and Isolation of Electrolyte

The photocatalyst used functions inefficiently in the presence of oxygen. In order to prevent this, three steps are taken as follows:

- The fresh electrolyte solution is de-aerated.
- The de-aerated solution is transferred to the constant pressure reservoir without exposure to air.
- The catalyst is transferred to the reaction vessel in a nitrogen environment.

It is stated that the presence of oxygen results in the reduction of oxygen instead of hydrogen (Buehler et al., 1984; Reber and Meier, 1984). It is also observed during the experimental runs that the catalyst is deactivated following prolonged exposure to oxygen.

For batch experiments, the solution is renewed by extracting the used solution via a pump, and then pulling the fresh solution in by creating a vacuum in the reactor. This too, in essence, is a pseudo-flow process. This section describes the methodology and the setup that is devised in order to facilitate the three steps described above.

4.3.1 De-aeration of Freshly Created Electrolyte

The de-aerator is set-up as shown in Figure 4.14. A volumetric flask is set-up with a rubber cork through which three tubes protrude. Each tube has a valve at its end that allows it to be sealed as required, and allows easy connection and removal of the vacuum and nitrogen hoses. One of the tubes extends all the way to the flask bottom so that it is submerged in the liquid. The other two tubes end just after the cork, so that the inner ends are in the air space above the liquid. The flask is clamped by a retort stand in a manner that suspends it inside an ultrasonic bath. Liquid is poured into the flask, and the cork attached. Nitrogen is bubbled through the solution using the tube that is submerged into the solution (tube 1) for five minutes, while the valve connected to tube 2 is open. The valve is closed, then the nitrogen supply is disconnected, ensuring a nitrogen environment inside the flask. A vacuum is connected to tube 3, and low pressure of approximately 6 kPa is created in the flask. The ultrasonic bath is set to 'degas' and turned on while the flask is in vacuum. Extreme agitation of the solution is observed, and bubbles rapidly escaping to the surface from the liquid. After about 1 minute, the bubbles cease, indicating that no more dissolved oxygen is present inside the liquid. The valve on tube 2 is closed, and the vacuum disconnected. The nitrogen supply is now connected to tube 3, and the pressure of the chamber brought to above atmospheric pressure. This ensures that no oxygen enters the flask from the environment.

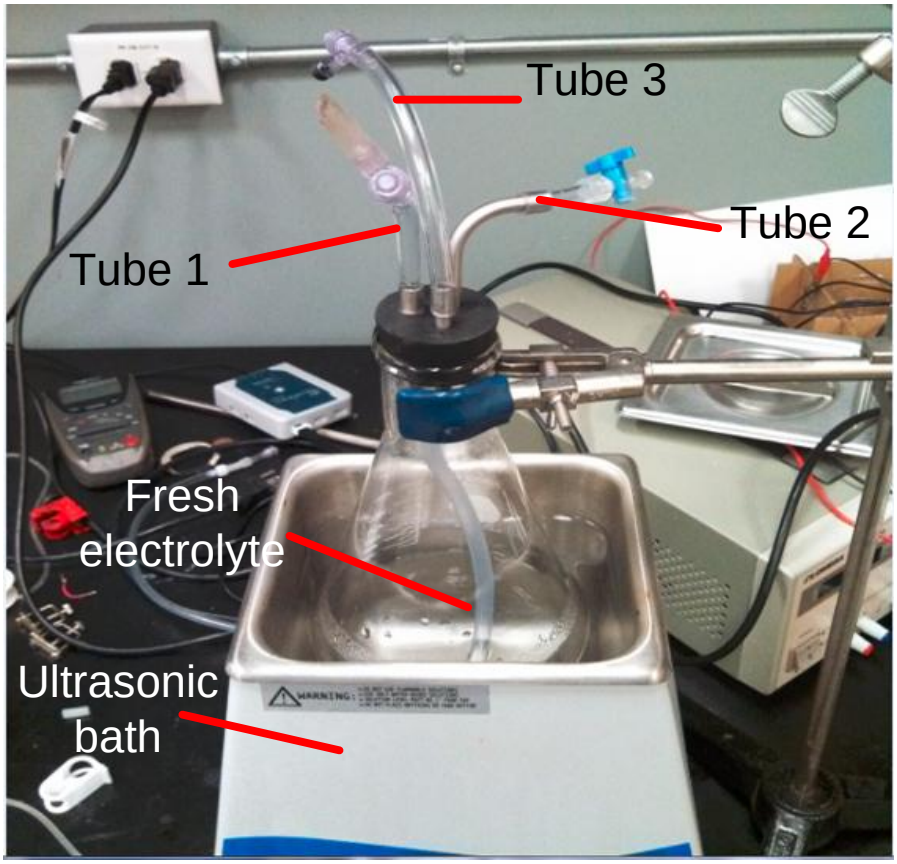

Figure 4.14: Experimental setup for fresh solution de-aeration.

4.3.2 Fresh Reservoir Fill-up Procedure

The volumetric flask with the de-aerated solution is placed next to another retort stand that holds a bag to be used as the fresh reservoir. Tube 1 is connected to one end of a pump, while the other end is connected to a sealed, vacuumed, bag (fresh solution reservoir). The solution is pumped into the bag using a peristaltic pump, ensuring a transition that does not bring the solution into contact with the air. Having the bag as the fresh reservoir allows the solution to be delivered to the reactor at a constant pressure. The set-up is shown in Figure 4.15. Nitrogen may be supplied to the volumetric flask to increase the pressure in the flask and facilitate the transfer of the solution from the volumetric flask into the reservoir.

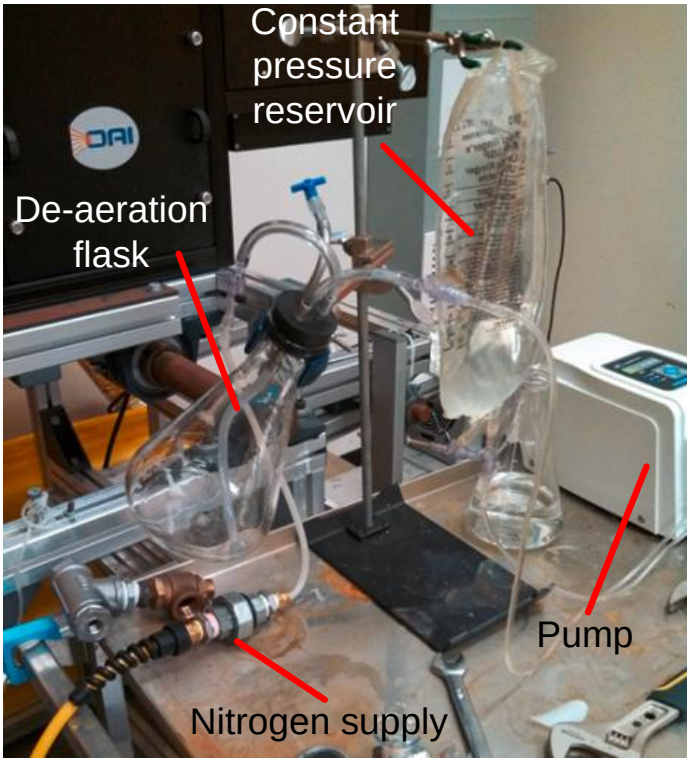

Figure 4.15: Transfer of de-aerated solution into reservoir.

4.3.3 Preparation of Reaction Vessel

The catalyst is stored in an oxygen free environment, and must be transferred to the reactor in a manner that does not expose it to oxygen. A glove box is used for this purpose. The reaction vessel is configured in such a manner as to allow it to be detached from the reactor while sealed. The glove box is prepared by vacuuming initially to get rid of the air present inside, and then filling it with nitrogen. The items to be worked on are placed inside the reactor before the nitrogen environment is created. The reaction vessel is disassembled inside and the required contents placed inside. Working through the gloves requires a certain level of skills and practice. The pressure inside the glove box must be maintained at a particular level that allows operation. A pressure that is too high restricts movement of the arms as it attempts to increase the volume of the glove box through expansion of the stretchable sleeves. Figure 4.16 shows the glove box with the nitrogen environment and the conduction of the required operation.

Figure 4.16: Preparation of reaction vessel for batch process inside the glove box.

4.4 Implementation of Continuous Flow Reactor Operation

Continuous flow operation of a catalytic process has the ability to increase the yield of hydrogen by maintaining concentration of donor ions in the electrolyte. The design of the flow scheme is shown in Figure 4.17.

The fresh solution is stored in a sealed compressible bag in order to maintain the reservoir pressure. The design is constrained by the availability of a single pump. Flow from the fresh reservoir is driven by a pressure differential, and controlled by the restrictor. The reservoir is at atmospheric pressure. The reactor is operated at a pressure below atmosphere. The fresh solution enters the reaction vessel at the top. Used solution is extracted from the bottom, through a retainer. The vacuum pump maintains the pressure in the waste reservoir. Keeping the pressure constant at all points minimizes variations in flow. The flow rate is calculated by taking weight measurements at regular intervals.

The micro flow pump is a major component of the flow system. A peristaltic pump is used as it prevents the electrolyte from coming into contact with any pump materials, and thereby prevents corrosive effects of sulfite ions. The pump is digitally controlled, and is able to provide a maximum flow rate of 500 ml/h between equal pressure ends. The digital control allows precise measurement and repeatability of flow. Figure 4.18 shows the micro-pump.

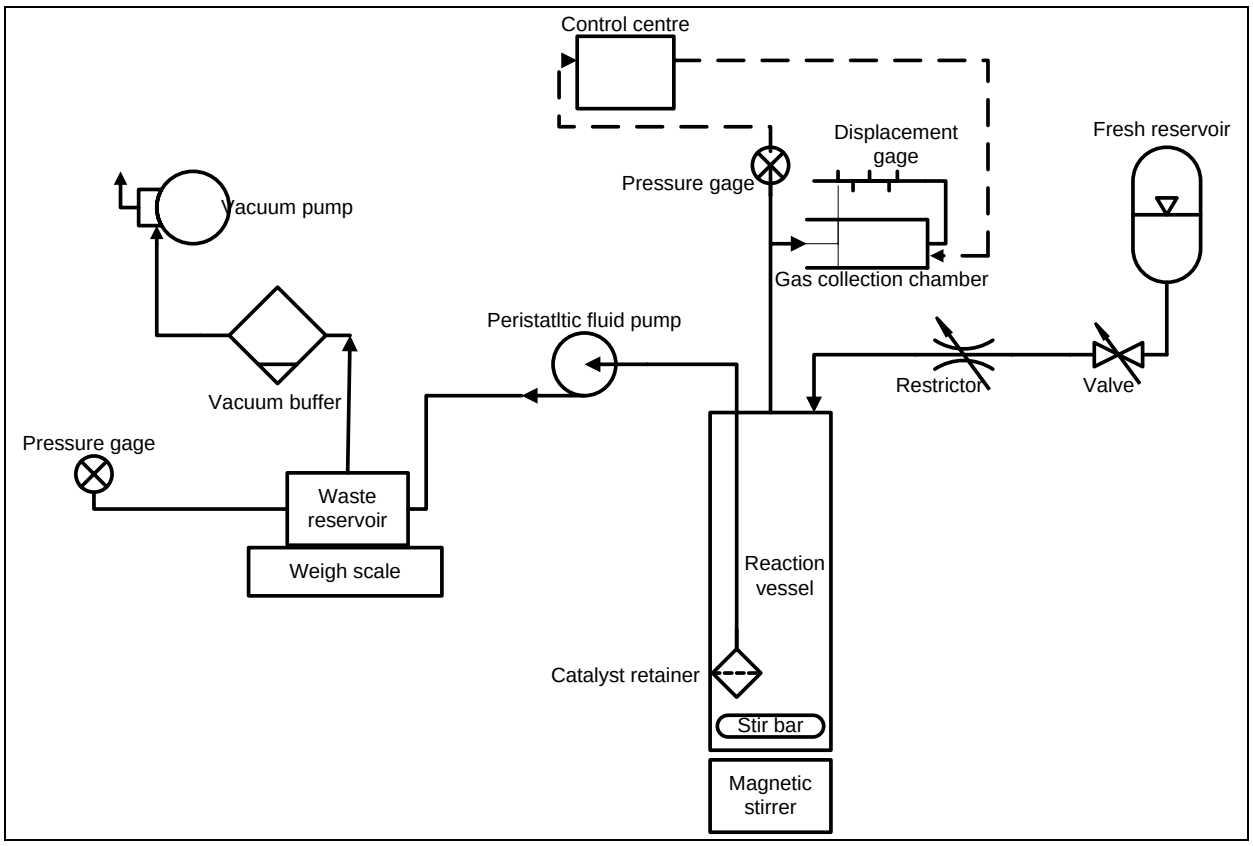

Figure 4.17: Flow scheme for continuous reactor operation.

4.5 Hybrid System Operation

The schematic of the hybrid system used for experimental study is shown in Figure 4.19. The complete system in action is shown in Figure 4.20. Hydrogen production measurements are manually recorded off the digital caliper attached to the piston cylinder. PV measurements ($V_{OC}$and I_{SC}) are recorded using a multi-meter. The flow rate is measured by noting the weight

increments of the waste reservoir. The energy input is known by knowing the intensity of the solar simulator and the concentration factor, determined experimentally.

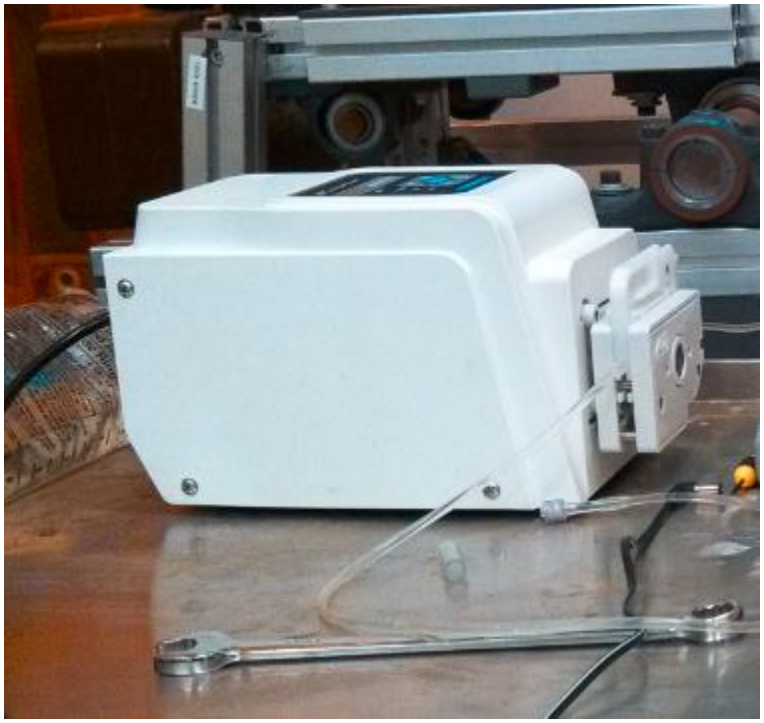

Figure 4.18: Micro flow pump used to implement a continuous flow operation.

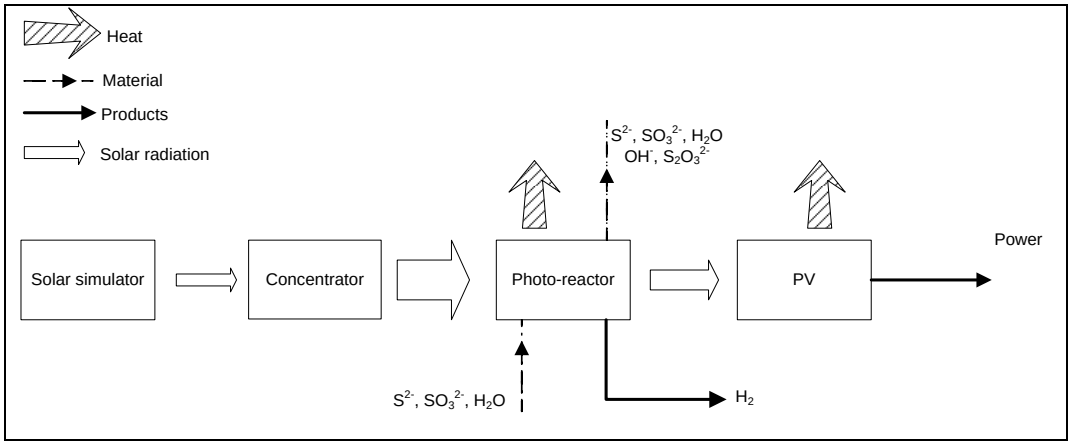

Figure 4.19: The full hybridized experimental system.

The solar simulator, manufactured by OAI, produces highly collimated light that simulates exactly the spectrum of the sun, as described by AM1.5. It is able to produce an output of 1300 W/m^2 at its maximum intensity. It has the capacity to simulate different environmental

conditions by variation of its intensity, and is mounted on a specially designed frame that allows its angle of incidence to be adjusted. However, for this study, the intensity and the angle of incidence are both maintained throughout. The simulator provides the only input into the system.

Heliostats affixed in the field of the solar simulator collect the light from the simulator, and concentrate it to a desired area. Small silver mirrors act as the heliostats. The light concentration factor of 4 is achieved. This is low in comparison to an actual solar tower system, where concentration factors of up to 100 or more may be achieved, but a limitation was placed in this case due to two factors. Firstly, the land area was limited, as the simulator output only covered an area of 8 inch X 8 inch. Secondly, there was a desire to avoid high temperatures, as some of the material on the photoreactor was not suitable for it. The aim here was two-fold: to observe the effect of a greater concentration of light on the photocatalytic process, and to test the concept of a hybridized photocatalytic-PV system in a cavity receiver. Both of these aims are achievable, and demonstrable by the present design.

The photoreactor receives the concentrated reaction, which causes a chemical reaction to occur. This reaction is described under results. A significant portion of the light is absorbed by the reaction vessel. Some of it is released as heat. In an actual system, considering the heat as an output is likely to significantly improve the efficiency, but here it is not considered, and is termed a loss.

Photons reflected or transmitted by the reaction vessel are absorbed by the PV, or escape from the reactor as light, or as heat. The PV cells absorb those photons in the middle spectrum, and produce electrical power. A heat loss also accompanies the functioning of the PV panels, but

this is not likely to have as much of an impact on the efficiency as that from the photocatalytic reaction vessel, if recovered.

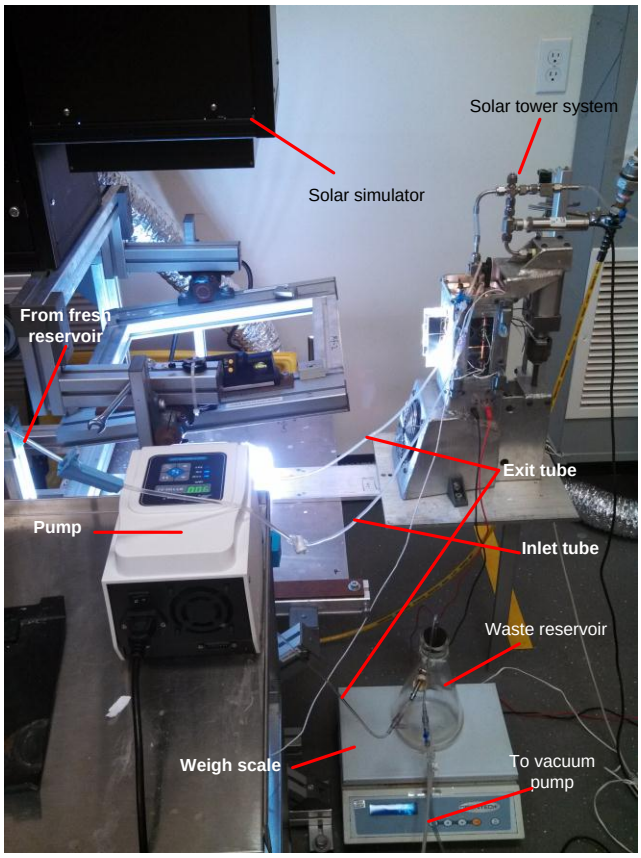

Figure 4.20: Complete hybrid system.

4.6 Experimental Methodology

In order to comprehend the system described, certain experiments are carried out. For all experiments, the catalyst concentration, light intensity, solution volume and other parameters are kept constant. For each experiment, three runs are conducted in order to ensure an acceptable level of repeatability for the experiments is achieved.

- Batch experiments at two different temperatures to determine the temperature-rate relationship.

- Batch experiments at three different pressures to determine the pressure-rate relationship.
- Batch experiments at three different concentrations to develop a concentration-rate model and validate it
- Pseudo-flow experiments at one concentration value in order to validate the flow model.

4.7 Uncertainty Analysis

Kline and McClintock (1953) define three types of errors that may play a part in the uncertainty of a measured variable. These are mistakes, accidental errors, or fixed errors. Mistakes are simply erroneous readings of devices such as scales, gauges and timers. An understanding of the process being conducted and careful observation allows these errors to be disregarded, as they result in significant deviation from the median value for a variable, and cause a large, noticeable error in the results calculated using that variable. Fixed errors, as the name implies, cause the readings to of a variable to be off by the same amount repeatedly. If the cause is known, then a suitable adjustment may be made to account for this type of error. Accidental errors are those due to which repeated readings differ randomly within a certain bound, for some unknown reasons.

In this work, the completeness of a value is accomplished by stating the uncertainty propagation of a calculated value. Since calculated values are functions of measured values, the uncertainties of the measured values play a part in the uncertainty of the calculated value. The method of determination of the uncertainty propagation is described later. This statement accounts for the accidental errors that are caused by the instruments. The second statement

concerns the error band found by repetition of experiments. Each experiment is repeated three times, and the median value is used for the statement of results. This is to account for the process based and procedure based accidental errors.

Fixed errors are eradicated by minimizing the bias error that is present in the instruments. The height gage is compared against manually measured readings. The pressure gage and temperature gage are compared against different instruments of the same type. The mistakes, as mentioned before, may be disregarded by careful observation of the readings taken. It is believed that the statement of results in this manner is sufficient in providing validity to the measured or calculated value that is in question.

The uncertainty propagation is determined by the method described in NIST Technical Note 1297 (Taylor and Kuyatt, 1994). The calculation of uncertainty is described by the following equation

$$U_Y = \sqrt{\sum_i \left(\frac{\partial Y}{\partial X_i}\right)^2 U_{X_i}^2} \tag{4.1}$$

where U represents the uncertainty, Y is the calculated quantity, and X_i is the i^{th} measured quantity. The determination of the uncertainty requires data on the uncertainty of the instruments used for the measured quantities. These are obtained from manufacturer's data, and presented in Table 4.2. The uncertainty value for data is presented with the results in their respective sections.

The way that the determination of the moles of hydrogen produced is structured allows the cumulative error in the final value to be determined. Equation 6.10, presented later, is used to determine the incremental increase in the moles of hydrogen. This value is accompanied by its uncertainty. As the next incremental increase in the moles of hydrogen is calculated, with its own

uncertainty, and added to the previously calculated value, the uncertainties of both quantities result in a cumulative uncertainty. Consequently, as all the incremental values are summed to obtain a final value of the hydrogen moles produced, the accompanying uncertainty is the cumulative uncertainty of the complete process. So not only does the uncertainty give an indication of the error of the final value, but it also relates to the shape of the process curve.

Table 4.1: Error values for measuring instruments.

Device Function	Device Name/Model	Absolute Error	Relative Error (%)
Pressure sensor	Omega PX409-USB	5 Pa	-
Temperature sensor	Omega RT PT-100	0.15 K	-
Height gage	iGAGING IP54	0.012 mm	-
Voltmeter	Equus 3300	-	0.8
Ammeter	Equus 3300	-	1.5
Light meter	Daystar DS-05	-	3
Weigh scale	Scientech SHC12	0.2 g	-

Chapter 5: Conceptual Design and Analysis

5.1 Large Scale Conceptual Design

The hybridized system scheme employed for the full hydrogen production system is shown in Figure 5.1. States 1 to 6 sown on the diagram track the energy and exergy content of the solar radiation as it passes through the optical devices. The radiation is split up according to the desired wavelengths and used as an input for the respective hydrogen producing processes.

The radiation from the sun, at 1, is concentrated via a heliostat field, and directed to the receiver atop a solar tower. At the entrance to the cavity receiver is an optical diffuser. The function of the diffuser, as its name suggests, is to diffuse the concentrated radiation inside the cavity receiver, so that photons are uniformly distributed. This ensures that the radiation is not blocked by elements towards the front of the cavity. Within the cavity receiver are three devices that absorb the solar radiation: photocatalytic reactors, PV modules, and a set of pipes that constitute the thermal receiver. Each of these devices are covered with suitable band pass coatings that only allow the desired frequency of radiation to pass through into the components, as indicated by states 4, 5, and 6.

Multiple cylindrical photoreactors are arranged vertically within the cavity receiver. Having multiple reactors that are smaller sized as compared to a single reactor is advantageous as it allows greater penetration of radiation into the depth of the reactor, and also allows the reactors to be distributed throughout the cavity receiver, thus allowing uniform spatial absorption of radiation. An additional benefit is that the reactors can operate independent of the other reactors, and the system may still operate at lower capacity during maintenance operations. For the continuous flow photocatalytic process, fresh solution enters the reactor at 11. The exit

stream at 7 contains all the chemical species, including the produced hydrogen gas as bubbles in the electrolyte. The colloidal catalyst that instigates the photoreaction is retained within the photoreactors, and is not a part of the flow streams. Hydrogen gas is separated inside the gas separator, and the stream is sent onwards to the waste extractor where excess hydroxyl and thiosulfate ions are removed. The stream from the waste extractor is sent to the make-up chamber, where the requisite chemical species are added in order to maintain the electrolyte composition, and the solution is pumped back into the reactor. The operating temperature of the photoreactors differs from the temperature of the cavity receiver at steady state, and thus, cooling tubes pass along the centre of the photoreactors, so that they do not interfere with the radiation for the photocatalytic process, while maintaining a desired temperature.

The walls of the cavity receiver are lined with PV modules. These modules harness the radiation that is allowed to pass through by the band pass coating applied on the front face of the modules. The PV modules produce electrical power, which is sent to the electrical management station. The modules are cooled using an appropriate heat sink at the back face, between the modules and the cavity receiver walls.

A network of cooling tubes runs through the photoreactors. The tubes are covered with coatings that only allow the long wavelength radiation to be absorbed, indicated by state 6. The heated fluid is sent to a hot storage, which is used as a heat source for a heat engine. The storage tanks act as energy buffers for the heat engine. Here the heat is transferred to the working fluid of the heat engine, which emerges as a superheated vapour at state 17. Power is produced as the fluid expands in the turbine. The working fluid is then cooled in the condenser and pumped back to the heat exchanger to maintain the cycle. The turbine is connected to a generator, which produces electrical power (23), and sends it to the power conditioning unit.

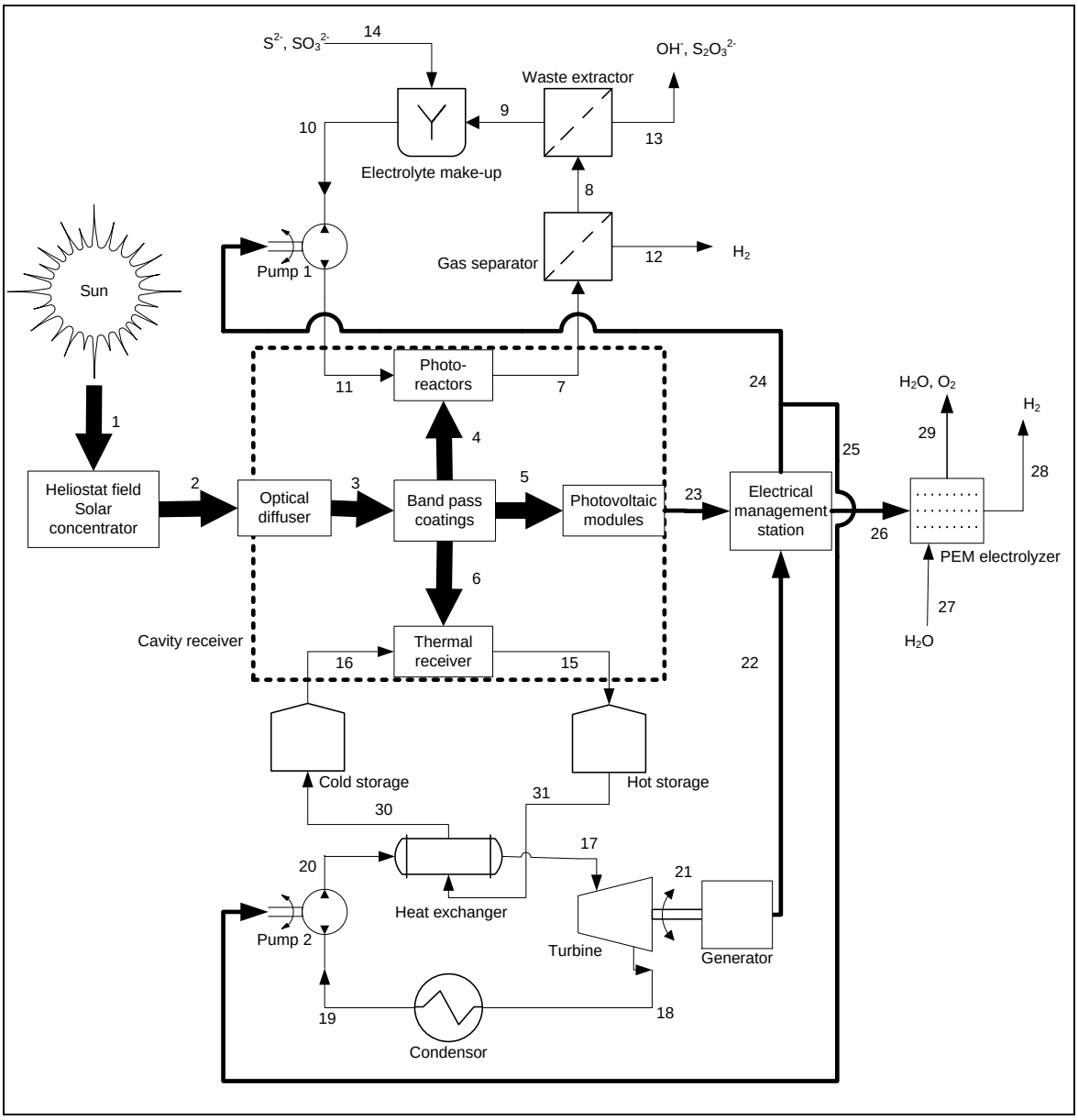

Figure 5.1: Hybridized scheme for hydrogen production plant.

The electrical management station (EMS) is a vital cog due to the intermittent nature of the solar radiation. The EMS provides electrical power to a proton exchange membrane (PEM) electrolyzer, as well as some auxiliary equipment required for the system. The auxiliary equipment, such as the pumps indicated on the figure, require a constant electrical input. The EMS achieves this by appropriately sharing the load between the auxiliaries and the PEM electrolyzer. Such an electrolyzer is used mainly because it is suited to a rapidly varying supply

of electrical power input (Ursua et al., 2012), as opposed to alkaline electrolyzers which respond slowly to power fluctuations. As the power input to the electrolyzer is varied, the EMS adjusts the voltage and current to match the power curve of the electrolyzer unit, in order to operate it at peak efficiency.

The low quality heat rejection occurs in the photoreactors, PV modules and the condenser of the heat engine, as described above. This heat may be used for heating, absorption cooling, or hot water needs of the operating stations of the hydrogen plant.

5.2 Spectral Optics Analysis

The ASTM G173-03 Reference spectrum defines the solar radiation that is incident on the earth's surface. This spectrum provides the power per wavelength for every wavelength of the solar spectrum for 1000 W/m^2. To convert this spectrum to any other intensity value, it is assumed that the shape of the spectrum does not vary as the intensity changes. This assumption is particularly valid with respect to a solar simulator. The power per unit area per unit wavelength for any intensity can then be found using

$$I_\lambda = \frac{I}{\int_0^\infty \bar{I}_\lambda \, d\lambda} \times \bar{I}_\lambda \tag{5.1}$$

where I is the intensity per unit area, I_λ is the intensity per unit area per wavelength, $\bar{I}$ indicates normalized intensity.

The reflectance of light depends on the material reflected off and the wavelength of the light. The reflectance is given by

$$\mathcal{R}_\lambda = \frac{(n-1)^2+k^2}{(n-1)^2+k^2} \times 100\ \% \tag{5.2}$$

where $\mathcal{R}_\lambda$ is the percent of incident light reflected,$\mathcal{n}$ is the refractive index of reflective material, and k is the extinction coefficient of the reflective material. $\mathcal{n}$ and k are wavelength dependent constants for the reflective material, and are obtainable from appropriate sources (Palik, 1998).

The concentrated spectrum is given by

$$I_{\lambda,conc} = I_\lambda f_{conc} \frac{\mathcal{R}_\lambda}{100} \tag{5.3}$$

where $I_{\lambda,conc}$ is the concentrated power per unit area per wavelength, and f_{conc} is the concentration factor of the heliostats and is determined experimentally.

The concentrated spectral photon distribution is given by

$$\dot{n}_{ph,\lambda} = \frac{I_{\lambda,conc}}{\mathcal{A}\mathbb{h}\mathbb{c}/\lambda} \tag{5.4}$$

where $\dot{n}_{ph,\lambda}$ is the rate of moles of photons per unit area per second per wavelength, $\mathbb{h} =$ is Planck's constant, and $\mathbb{c}$ is the speed of light, and $\mathcal{A}$ is Avogadro's number.

The rate at which photons enter the reactor is then given by

$$\dot{n}_{ph} = \int_{\lambda 1}^{\lambda n} \dot{n}_{ph,\lambda}\, d\lambda \times A_w \tag{5.5}$$

where $\dot{n}_{ph}$ is the photon mole rate entering the cavity receiver, and A_w is the area of the opening of the cavity receiver.

The rate at which the photons enter the reaction vessel is slightly different and is given by

$$\dot{n}_{ph,r} = \int_{\lambda 1}^{\lambda n} \dot{n}_{ph,\lambda}\, d\lambda \times A_{w,r} \tag{5.6}$$

where, $\dot{N}_{ph,r}$ is the rate at which moles of photons enter the reaction vessel, and $A_{w,r}$ is the exposed surface of the reaction vessel.

5.3 Determination of Hydrogen Production

In the constant pressure experiments, an electronically controlled piston detects changes in pressure and adjusts the volume of gas space accordingly. The increase in the volume is used to measure the production of hydrogen gas. Due to this set-up however, volume change may also be the result of variations in the temperature. Initially, the head space is vacuumed, and purged with nitrogen for ten minutes. This cycle is repeated three times to ensure that nitrogen is present solely in the cylinder. The ideal gas equation is written as follows:

$$P \times V_i = (n_{H_2,i} + n_{N_2}) \times \bar{R} \times T_i \tag{5.7}$$

where n is the number of molecules of gaseous species, P is the total pressure of gaseous species, V is the total volume occupied by the gas, $\bar{R}$ is the universal gas constant, and T is the reactor temperature. The subscript i indicates the index of the time intervals at which volume and temperature measurements are recorded. Equation 5.7 is solved for the moles of hydrogen to give

$$n_{H_2,i} = \frac{P \times V_i}{\bar{R} \times T_i} - n_{N_2} \tag{5.8}$$

The increase in the number of molecules of hydrogen gas between t_{i-1} and t_i can be calculated by using Equation 5.8, and subtracting, to get

$$\Delta n_{H_2} = n_{H_2,i} - n_{H_2,i-1} \tag{5.9}$$

which can be expanded using Equation 5.8 as follows:

$$\Delta n_{H_2} = \frac{P}{\bar{R}} \times \left(\frac{V_i}{T_i} - \frac{V_{i-1}}{T_{i-1}}\right) \tag{5.10}$$

If the initial value of moles of hydrogen is known, then the total value of molecules of hydrogen at any instance in time, t_i, can be calculated by

$$n_{H_2,i} = \frac{P}{\bar{R}} \times \left(\frac{V_i}{T_i} - \frac{V_{i-1}}{T_{i-1}}\right) + n_{H_2,i-1} \tag{5.11}$$

which allows the hydrogen production to be calculated based on the variations in volume of the cylinder and the temperature of the gas, and accounts for the presence of nitrogen without involving it in calculations.

5.4 Development of Rate Model

In this section, a model is developed that allows the progression of a reaction to be simulated for a continuous flow reactor. A model is created based on batch experiments conducted on a small scale model. It is then validated by using the results of further batch experiments, before being extended to a flow process.

The rate of the photocatalytic process depends on the probability of desirable collisions (Zamfirescu et al., 2013). In other words, the changes that occur in the solution as the reaction proceeds decrease the reaction rate. The molecules of undesirable ionic species, which are the product of the reaction, increase, while the electron donors, which are the desirable species in this case, decrease. This directly decreases the probability of desired collisions required for the reaction to occur. Thus, it can be inferred that the reaction rate is a function of the ionic species that are responsible for the changing composition (Reber and Meier, 1984). Based on the reaction mechanism described earlier, the rate of reaction can be written down as

$$r(H_2) = f(n_{S^{2-}}, n_{OH^-,prod}) \tag{5.12}$$

where the rate is $r(H_2)$, and n indicates moles. The sulfite ion is not included in the rate expression because in the mechanism, it is used in an intermediary step after the donation of an electron by the sulfide ion, and decreases in proportion to the sulfide ion. The increase in the presence of the hydroxyl ion is used as an argument for the expression, instead of the absolute value of the hydroxyl ion, because the fresh solution in any case has a certain constant amount of hydroxyl ions present, which depends on the initial concentration of the electron donor.

Based on experimental results conducted for a batch process, the following relationship is obtained for the rate of reaction:

$$r(H_2) = \frac{1}{1000} \times \begin{cases} 0.0001965 \times \ln a + 0.0005243, & a > 76.9 \\ 0.0009383 \times \ln a - 0.0026964, & 76.9 \geq a > 23.8 \\ 0.0000508 \times e^{0.1679092 \times a}, & a \leq 23.8 \end{cases} \tag{5.13}$$

where the parameter a describes the change in the electrolyte composition in terms of the ionic species, and is termed the solution degradation variable, given by

$$a = \frac{(n_{S^{2-},t}) - (n_{OH^-,prod,t})}{(n_{OH^-,prod,t})} \tag{5.14}$$

Here, the quantities on the right side of the equation are those present in the solution at a particular time. If the initial concentrations are known, then the process may be simulated by calculating an initial value of the parameter a using Equation 5.14, determining the hydrogen production rate for the first minute using Equation 5.13, calculating the variation in the moles of the ionic species based on the moles of hydrogen produced and the stoichiometric reaction equation, and repeating the steps again using the new values of moles of species. The process can thus be simulated over whatever length of period that is desired. The moles of hydrogen

produced, the moles of sulfide ions present, and the moles of hydroxyl ions produced are calculated using the following equations:

$$\frac{dn_{H_2}}{dt} = r(H_2)_t \tag{5.15}$$

$$\frac{dn_{S^{2-}}}{dt} = -r(H_2)_t \tag{5.16}$$

$$\frac{dn_{OH^-,prod}}{dt} = 2 \times r(H_2)_t \tag{5.17}$$

The model is extended further to simulate the production of hydrogen for a continuous flow process. To include the flow of ionic species in and out of the reactor, Equations 5.16 and 5.17 are modified as follows:

$$\frac{dn_{S^{2-}}}{dt} = -r(H_2)_t + \dot{V} \times [S^{2-}]_{in} - \dot{V} \times [S^{2-}]_{r,t} \tag{5.18}$$

$$\frac{dn_{OH^-,prod}}{dt} = 2 \times r(H_2)_t - \dot{V} \times [OH^-{}_{prod}]_{r,t} \tag{5.19}$$

Here, in Equation 5.18, the second last term on the right hand side indicates the moles of ions flowing into the system. This is a constant value, specified by the molarity of the fresh solution, as indicated by $[S^{2-}]_{in}$. This term is absent from Equation 5.19, as this equation deals only with the moles of hydroxyl ions produced in reaction. The fresh solution does not contain any moles of hydroxyl ions produced. The last term on the right hand side of each equation calculates the flow of ionic species out of the system. This term depends on the concentration of respective species inside the reactor at that particular instance.

5.5 Photovoltaic Modelling

The current voltage relationship for a PV cell, defined as its characteristic curve, may be modelled by the following equation (Golder, 2006):

$$\mathbb{I}_c = \mathbb{I}_{SC} - \mathbb{I}_0\left(e^{(q\mathbb{V}_C+\mathbb{I}_C R_S)/\mathbb{m}KT_C} - 1\right) \tag{5.20}$$

where $\mathbb{I}_c$ is the cell current, $\mathbb{I}_{SC}$ is the short circuit current, $\mathbb{I}_0$ is the saturation current, $\mathbb{V}_C$ is the cell voltage, q is the elementary charge having a value of 1.6×10^{-19} C, R_S is the series resistance, $\mathbb{m}$ is the nonideality constant for the cell, K is a constant having a value 1.38×10^{-23}J/K, and $T_C$is the cell temperature (K). All currents are measured in amperes (A), and the voltage in volts (V).

The saturation current is determined by setting cell current to 0 and the cell voltage equal to the open circuit voltage. The saturation current is then determined by

$$\mathbb{I}_0 = \frac{\mathbb{I}_{SC}}{e^{qV_C/\mathbb{m}KT_C}} \tag{5.21}$$

Once the constants in the equations are all defined, Equation 5.20 is used to plot the characteristic curve of the PV cell at any intensity using only the measured values for the short circuit current and open circuit voltage. The constants are determined by plotting the characteristic curve at any intensity, and curve fitting Equation 5.20 to the experimental plot. Once the cell current and cell voltage values are determined, the power curve may be determined by calculating the power at all values of the cell voltage using

$$\dot{W}_C = V_C \times I_C \tag{5.22}$$

5.6 Quantum Efficiency

The quantum efficiency is calculated as the percentage of successful quantum events occurring. Since this defines the quality of the photocatalytic process itself, the input to the equation is the moles of photons that are larger than the band gap of the CdS. The output is twice moles of hydrogen produced, as two photons are required for a hydrogen molecule to be produced. The equation is defined as

$$\phi = \frac{2 \times \dot{n}_{H_2}}{\dot{n}_{ph}} \tag{5.23}$$

where ϕ is the quantum efficiency, $\dot{n}_{H_2}$ is the rate of production of hydrogen, and $\dot{n}_{ph}$ is the rate at which photons enter the reactor. For calculation of efficiency of batch processes of molarity 0.3 M and above, the efficiency can be stated by replacing the rates of the hydrogen and photons by amounts for a given time. Efficiencies of batch process stated in the results take the time as 1 hour. The concentration is sufficient to maintain a relatively constant rate for that duration.

5.7 Thermodynamic Performance Analysis

To analyse the large scale system described in Figure 5.1, the energy and exergy interchange at every component is desired. The processes are all assumed to be in a state of steady flow.

In order to calculate the exergy of the solar spectrum, the concept of the effective photon temperature is utilized (Chen et al., 2008) where the effective photon temperature at each wavelength is defined as

$$T_\lambda = \frac{c_\lambda}{\lambda} \tag{5.24}$$

where $c_\lambda = 0.00533016\, mK$ is a constant. This concept is used to determine the effective spectrum temperature, which leads to the determination of the Carnot factor, and the calculation of exergy in a form analogous to the determination of the exergy of thermal energy.

For shaft work and electrical work, the exergy content is equal to its exergy content, as it is in its most useful form. For thermal energy, the exergy is calculated by multiplication with its Carnot factor, based on the temperature of the heat source, as

$$\dot{E}x_Q = \dot{Q}\left(1 - \frac{T_0}{T_{source}}\right) \tag{5.25}$$

The exergy of a flow stream is a combination of the physical and chemical exergies of the substances contained within the stream, and the kinetic energy and potential energy of the stream itself. Since the analysis in essence involves the change of exergy of flow stream, the assumption that the kinetic and potential energy changes are negligible allows the simplification to be made where the exergy change due to those two forms of energies is ignored. Further, in processes where no chemical reactions occur, the chemical exergy changes may also be ignored. The specific chemical exergy and specific physical exergy of flow streams, along with the total specific exergy of the stream may then be written respectively, according to the description provided by Dincer and Rosen (2012), as

$$Ex_{\mathrm{ch}} = \Delta G_0 + \sum_{\mathrm{i}} n_i ex_{\mathrm{ch,i}} \tag{5.26}$$

$$Ex_{\mathrm{phys}} = (H - H_0) - T_0(S - S_0) \tag{5.27}$$

$$Ex = Ex_{phys} + Ex_{ch} \tag{5.28}$$

where ΔG is the Gibbs energy of formation of the stream, n is the moles of chemical species in the stream, i is the subscript indicating individual species, h and s are the specific enthalpy and entropy respectively, and the subscript 0 indicates the value at reference state.

5.7.1 Solar Radiation

All the solar radiation emitted from the sun is assumed to be incident on the heliostats field (concentrator system). Therefore, the input to the concentrator is fully defined by expressing its energy, exergy, entropy, and temperature, according to the following equations:

$$\dot{E}_{1\lambda} = A_{conc}\dot{I}_{sol,\lambda} \tag{5.29}$$

where $\dot{E}_{1\lambda}$ is the energy with respect to wavelength entering the system, A_{conc} is the total effective area of the concentrator, and $I_{sol,\lambda}$ is the direct circumsolar intensity from the sun with respect to wavelength. $I_{sol,\lambda}$ is derivable from any of the standard solar spectrums used if the total intensity of a location is known. The total energy entering the concentrator is then calculated using

$$\dot{E}_1 = \int_0^\infty \dot{E}_{1\lambda} d\lambda \tag{5.30}$$

The effective entropy flux of the spectrum is then defined as

$$\dot{S}_1 = \int_0^\infty \frac{\dot{I}_{1\lambda}}{T_\lambda} d\lambda \tag{5.31}$$

where T_λ is the effective photon temperature with respect to radiation wavelength, defined by Equation 5.24.

Once the total energy and effective entropy of the spectrum are defined, the effective temperature can simply be calculated as

$$T_1 = \frac{\dot{I}_1}{\dot{S}_1} \tag{5.32}$$

Following from that, the effective exergy of the spectrum can be defined as

$$\dot{E}x_1 = \dot{E}_1 \left(1 - \frac{T_0}{T_1}\right) \tag{5.33}$$

The reflectance of mirrors is given by Equation 6.2 previously, and using that, the energy leaving the concentrator can be calculated using

$$\dot{E}_{2\lambda} = \dot{E}_{1\lambda} R_{c,\lambda} \tag{5.34}$$

The energy leaving the concentrator system, and its exergy, entropy and temperature can be calculated using the following equations:

$$\dot{E}_2 = F_{field} \int_0^\infty \dot{E}_{2\lambda} d\lambda \tag{5.35}$$

$$\dot{S}_2 = F_{field} \int_0^\infty \frac{\dot{I}_{2\lambda}}{T_\lambda} d\lambda \tag{5.36}$$

$$T_2 = \frac{\dot{I}_2}{\dot{S}_2} \tag{5.37}$$

$$\dot{E}x_2 = \dot{E}_2 \left(1 - \frac{T_0}{T_2}\right) \tag{5.38}$$

The factor F_{field} is the compounded optical factor for the heliostat field concentrator, and takes into account the various optical losses associated with it, as follows:

$$F_{field} = f_\theta f_s f_b f_{at} f_\gamma \tag{5.39}$$

where the individual factors on the right side of the equation refer to the losses due to the incident angle of the sun with respect to heliostats, the shading factor, the blocking factor, atmospheric attenuation, and optical aberration

For the optical concentrator, with the assumption that the loss of energy is in the form of heat, the energy, exergy and entropy balance are given by the following equations:

$$\dot{E}_1 = \dot{E}_2 + \dot{Q}_{l,conc} \tag{5.40}$$

$$\dot{E}x_1 = \dot{E}x_2 + \dot{Q}_{l,conc}\left(1 - \frac{T_0}{T_{conc}}\right) + \dot{E}x_{d,conc} \tag{5.41}$$

$$\dot{S}_1 + \dot{S}_{gen,conc} = \dot{S}_2 + \frac{\dot{Q}_{l,conc}}{T_{conc}} \tag{5.42}$$

where $\dot{E}_{l,conc}$, $\dot{E}x_{d,conc}$, $\dot{S}_{gen,conc}$ and are the total rate of energy loss, exergy destruction, and entropy generation at the optical concentrator respectively.

The concentrated radiation reaches the rectangular opening of the cavity receiver, where an optical diffuser spreads out the radiation into the cavity receiver. The optical diffuser has a wavelength dependent transmission characteristic. The characteristic parameters of the radiation at the diffuser exit may are given by the following:

$$\dot{E}_{3\lambda} = \dot{E}_{2\lambda} Tr_{d,\lambda} \tag{6.43}$$

$$\dot{E}_3 = \int_0^\infty \dot{E}_{3\lambda} d\lambda \tag{6.44}$$

$$\dot{S}_3 = \int_0^\infty \frac{\dot{I}_{3\lambda}}{T_\lambda} d\lambda \tag{6.45}$$

$$T_3 = \frac{\dot{I}_3}{\dot{S}_3} \tag{6.46}$$

$$\dot{E}x_3 = \dot{E}_3\left(1 - \frac{T_0}{T_3}\right) \tag{6.47}$$

The energy loss and exergy destruction of the diffuser are, respectively as

$$\dot{E}_2 = \dot{E}_3 + \dot{Q}_{l,diff} \tag{6.48}$$

$$\dot{E}x_2 = \dot{E}x_3 + \dot{Q}_{l,diff}\left(1 - \frac{T_0}{T_{diff}}\right) + \dot{E}x_{d,diff} \tag{6.49}$$

$$\dot{S}_2 + \dot{S}_{gen,diff} = \frac{\dot{Q}_{l,diff}}{T_{diff}} + \dot{S}_3 \tag{6.50}$$

Note that inside the cavity receiver there is an arrangement of multiple photoreactors, PV modules, and a network of pipes that absorb thermal energy via a heat transfer liquid flowing through them. Each is coated with the appropriate band pass coating that allows only the desirable wavelength photons to be transmitted, while the rest are reflected. The photons are not allowed to escape the cavity receiver except through the entrance. Here, the loss of photons through the entrance to the cavity receiver is neglected.

The characterizing parameters of the radiation that enter the photoreactors are

$$\dot{E}_{4\lambda} = \dot{E}_{3\lambda} Tr_{cat,\lambda} \tag{6.51}$$

$$\dot{E}_4 = \int_0^\infty \dot{E}_{4\lambda} d\lambda \tag{6.52}$$

$$\dot{S}_4 = \int_0^\infty \frac{\dot{I}_{4\lambda}}{T_\lambda} d\lambda \tag{6.53}$$

$$T_4 = \frac{\dot{I}_4}{\dot{S}_4} \tag{6.54}$$

$$\dot{E}x_4 = \dot{E}_4\left(1 - \frac{T_0}{T_4}\right) \tag{6.55}$$

The radiation entering the PV modules is based on the band gap coating applied on the module. The characteristic parameters are defined as

$$\dot{E}_{5\lambda} = \dot{E}_{3\lambda}(1 - Tr_{cat,\lambda})(Tr_{pv,\lambda}) \tag{6.56}$$

$$\dot{E}_5 = \int_0^\infty \dot{E}_{5\lambda} d\lambda \tag{6.57}$$

$$\dot{S}_5 = \int_0^\infty \frac{\dot{I}_{5\lambda}}{T_\lambda} d\lambda \tag{6.58}$$

$$T_5 = \frac{\dot{I}_5}{\dot{S}_5} \tag{6.59}$$

$$\dot{E}x_5 = \dot{E}_5 \left(1 - \frac{T_0}{T_5}\right) \tag{6.60}$$

The thermal receiver absorbs radiation that is passes through the band gap as follows:

$$\dot{E}_{6\lambda} = \dot{E}_{3\lambda}(1 - Tr_{cat,\lambda})(1 - Tr_{pv,\lambda})Tr_{th,\lambda} \tag{6.61}$$

$$\dot{E}_6 = \int_0^\infty \dot{E}_{6\lambda} d\lambda \tag{6.62}$$

$$\dot{S}_6 = \int_0^\infty \frac{\dot{I}_{6\lambda}}{T_\lambda} d\lambda \tag{6.63}$$

$$T_6 = \frac{\dot{I}_6}{\dot{S}_6} \tag{6.64}$$

$$\dot{E}x_6 = \dot{E}_6 \left(1 - \frac{T_0}{T_6}\right) \tag{6.65}$$

5.7.2 Photocatalytic System

For the photocatalytic system, the balance equations are written only for the photoreactor component of the cycle as follows:

$$\dot{m}_{11} = \dot{m}_7 \tag{6.66}$$

$$\dot{m}_{11} h_{11} + \dot{E}_4 = \dot{m}_7 h_7 + \dot{Q}_{l,cat} \tag{6.67}$$

$$\dot{m}_{11} ex_{11} + \dot{E}x_4 = \dot{m}_7 ex_7 + \dot{Q}_{l,cat}\left(1 - \frac{T_0}{T_{cat}}\right) + \dot{E}x_{d,cat} \tag{6.68}$$

$$\dot{m}_{11} s_{11} + \dot{S}_{gen,cat} = \dot{m}_7 s_7 + \frac{\dot{Q}_{l,cat}}{T_{cat}} \tag{6.69}$$

5.7.3 Photovoltaic Modules

Since no mass exchange occurs at the boundary of the photovoltaic modules, the energy, exergy, and entropy balance equations may be written as

$$\dot{E}_5 = \dot{W}_{23} + \dot{Q}_{l,PV} \tag{6.70}$$

$$\dot{E}x_5 = \dot{W}_{23} + \dot{Q}_{l,PV}\left(1 - \frac{T_0}{T_{PV}}\right) + \dot{E}x_{d,PV} \tag{6.71}$$

$$\dot{S}_6 + \dot{S}_{gen,PV} = \frac{\dot{Q}_{l,PV}}{T_{PV}} \tag{6.72}$$

5.7.4 Thermal Receiver

Assuming that the temperature of the thermal receiver is equal to the temperature of the cavity receiver, with this temperature being dependent on the mass flow rate of the thermal reservoir fluid, the mass, energy, exergy, and entropy balance equation for the thermal receiver are

$$\dot{m}_{16} = \dot{m}_{15} \tag{6.73}$$

$$\dot{E}_6 + \dot{m}_{16} h_{16} = \dot{m}_{15} h_{15} + \dot{Q}_{l,rec} \tag{6.74}$$

$$\dot{E}x_6 + \dot{m}_{16}ex_{16} = \dot{m}_{15}ex_{15} + \dot{Q}_{l,rec}\left(1 - \frac{T_0}{T_{rec}}\right) + \dot{E}x_{d,rec} \tag{6.75}$$

$$\dot{S}_6 + \dot{m}_{16}s_{16} + \dot{S}_{gen,rec} = \dot{m}_{15}s_{15} + \frac{\dot{Q}_{l,rec}}{T_{rec}} \tag{6.76}$$

The heat loss from the thermal receiver is the radiative heat loss due to the high temperature of the receiver with respect to the surroundings. If the temperature of the thermal receiver is assumed to be equal to the cavity receiver temperature, as is done in this case, then the environmental temperature is taken to be the surrounding temperature. The heat loss is given by

$$\dot{Q}_{l,rec} = \sigma\epsilon(T_{rec}^4 - T_0^4) \tag{6.77}$$

where σ is the Stefan Boltzmann constant, and ϵ is the emissivity of the material. For the storage tanks, the assumption is made that the tanks are significantly large reservoirs that do not undergo any changes in property, as long as the energy balance across them is maintained over a given time period. This allows the heat engine to run constantly with the only restriction the being the energy stored within the hot storage.

5.7.5 Heat Engine

The mass, energy, exergy and entropy balance equations for the closed heat exchanger are written as

$$\dot{m}_{31} = \dot{m}_{30} \tag{6.78}$$

$$\dot{m}_{20} = \dot{m}_{17} \tag{6.79}$$

$$\dot{m}_{31}h_{31} + \dot{m}_{20}h_{20} = \dot{m}_{30}h_{30} + \dot{m}_{17}h_{17} + \dot{Q}_{l,exch} \tag{6.80}$$

$$\dot{m}_{31}ex_{31} + \dot{m}_{20}ex_{20} = \dot{m}_{30}ex_{30} + \dot{m}_{17}ex_{17} + \dot{Q}_{l,exch}\left(1 - \frac{T_0}{T_{exch}}\right) + \dot{E}x_{d,exch} \tag{6.81}$$

$$\dot{m}_{31}s_{31} + \dot{m}_{20}s_{20} + \dot{S}_{gen,exch} = \dot{m}_{30}s_{30} + \dot{m}_{17}s_{17} + \frac{\dot{Q}_{l,exch}}{T_{exch}} \tag{6.82}$$

The mass, energy, exergy, and entropy balance for the turbine are written as

$$\dot{m}_{17} = \dot{m}_{18} \tag{6.83}$$

$$\dot{m}_{17}h_{17} = \dot{m}_{18}h_{18} + \dot{W}_{21} + \dot{Q}_{l,turb} \tag{6.84}$$

$$\dot{m}_{17}ex_{17} = \dot{m}_{18}ex_{18} + \dot{W}_{21} + \dot{Q}_{l,turb}\left(1 - \frac{T_0}{T_{turb}}\right) + \dot{E}x_{d,turb} \tag{6.85}$$

$$\dot{m}_{17}s_{17} + \dot{S}_{gen,turb} = \dot{m}_{18}s_{18} + \frac{\dot{Q}_{l,turb}}{T_{turb}} \tag{6.86}$$

The mass, energy, exergy, and entropy balance for the condenser are written as

$$\dot{m}_{18} = \dot{m}_{19} \tag{6.87}$$

$$\dot{m}_{18}h_{18} = \dot{m}_{19}h_{19} + \dot{Q}_{l,cond} \tag{6.88}$$

$$\dot{m}_{18}ex_{18} = \dot{m}_{19}ex_{19} + \dot{Q}_{l,cond}\left(1 - \frac{T_0}{T_{cond}}\right) + \dot{E}x_{d,cond} \tag{6.89}$$

$$\dot{m}_{18}s_{18} + \dot{S}_{gen,cond} = \dot{m}_{19}s_{19} + \frac{\dot{Q}_{l,cond}}{T_{cond}} \tag{6.90}$$

The mass, energy, exergy, and entropy balance equations for the pump are written as

$$\dot{m}_{19} = \dot{m}_{20} \tag{6.91}$$

$$\dot{m}_{19}h_{19} + \dot{W}_{25} = \dot{m}_{20}h_{20} + \dot{Q}_{l,pump2} \tag{6.92}$$

$$\dot{m}_{19}ex_{19} + \dot{W}_{25} = \dot{m}_{20}ex_{20} + \dot{Q}_{l,pump2}\left(1 - \frac{T_0}{T_{pump2}}\right) + \dot{E}x_{d,pump2} \tag{6.93}$$

$$\dot{m}_{19}s_{19} + \dot{S}_{gen,pump2} = \dot{m}_{20}s_{20} + \frac{\dot{Q}_{l,pump2}}{T_{pump2}} \quad (6.94)$$

For the generator, no exchange of mass takes place with the environment, and so the energy, exergy, and entropy balance equations are written as

$$\dot{W}_{21} = \dot{W}_{22} + \dot{Q}_{l,gn} \quad (6.95)$$

$$\dot{W}_{21} = \dot{W}_{22} + \dot{Q}_{l,gn}\left(1 - \frac{T_0}{T_{gn}}\right) + \dot{E}x_{d,gn} \quad (6.96)$$

$$\dot{S}_{gen,gn} = \frac{\dot{Q}_{l,gn}}{T_{gn}} \quad (6.97)$$

5.7.6 Electrical Management Station

No mass transfer occurs across the system boundary. The balance equations are written as

$$\dot{W}_{22} + \dot{W}_{23} = \dot{W}_{24} + \dot{W}_{25} + \dot{W}_{26} + \dot{Q}_{l,ECM} \quad (6.98)$$

$$\dot{W}_{22} + \dot{W}_{23} = \dot{W}_{24} + \dot{W}_{25} + \dot{W}_{26} + \dot{Q}_{l,ECM}\left(1 - \frac{T_0}{T_{ECM}}\right) + \dot{E}x_{d,ECM} \quad (6.99)$$

$$\dot{S}_{gen,ECM} = \frac{\dot{Q}_{l,ECM}}{T_{ECM}} \quad (6.100)$$

5.7.7 Proton Exchange Membrane Electrolyzer

The mass, energy, exergy and entropy balance for the PEM electrolyzer are written as

$$\dot{m}_{27} = \dot{m}_{28} + \dot{m}_{29} \quad (6.101)$$

$$\dot{m}_{27}h_{27} + \dot{W}_{26} = \dot{m}_{28}h_{28} + \dot{m}_{29}h_{29} + \dot{Q}_{l,PEM} \quad (6.102)$$

$$\dot{m}_{27}ex_{27} + \dot{W}_{26} = \dot{m}_{28}ex_{28} + \dot{m}_{29}ex_{29} + \dot{Q}_{l,PEM}\left(1 - \frac{T_0}{T_{pem}}\right) + \dot{E}x_{d,PEM} \quad (6.103)$$

$$\dot{m}_{27}s_{27} + \dot{S}_{gen,PEM} = \dot{m}_{28}s_{28} + \dot{m}_{29}s_{29} + \frac{\dot{Q}_{l,PEM}}{T_{PEM}} \quad (6.104)$$

5.7.8 System Efficiencies

The energy and exergy efficiencies of the system are calculated based on the following two equations

$$\eta_{en} = \frac{\dot{m}_{H_2} HHV_{H_2} + \dot{W}_{PV} + \dot{W}_{ORC}}{\dot{E}_1} \quad (6.105)$$

$$\eta_{ex} = \frac{\dot{m}_{H_2} ex_{H_2} + \dot{W}_{PV} + \dot{W}_{ORC}}{\dot{E}x_1} \quad (6.106)$$

Chapter 6: Results and Discussion

In this chapter, the experimental techniques derived for efficient experimentation are evaluated, and preliminary experimental results are validated by comparing them to published literature. The results of the experimental analysis of photocatalytic hydrogen production are presented and discussed. A photocatalytic rate model is developed and validated, which is subsequently used to simulate and analyse continuous photocatalytic processes. A novel conceptual system is presented for hybridized hydrogen production from solar energy, and its performance is analysed thermodynamically.

6.1 Validation of Experimental Results

The available photocatalytic reactor is re-configured extensively for the objectives of this study. Various techniques are derived, as explained in chapter 4, to facilitate efficient hydrogen photocatalytic hydrogen production. In this section the effectiveness of the reactor is evaluated through some preliminary studies that shed light on some particulars regarding the system. The experimental results obtained are compared and published data for validation.

Figure 6.1 shows the production of hydrogen gas under solar illumination of ZnS. 2 g of catalyst was placed in 90 ml of solution of 1 M sulfide ions, at a temperature of 40^{o}C, and stirred. After 60 mins, 0.11 mmol of hydrogen has are obtained. However, it is noticed that the rate of production noticeably starts to drop off.

A concentration of 1 M should be sufficient to maintain the production rate for the period of the experiment. However, the decrease in rate is due to the formation of disulfide ions, which compete with the reduction of protons, and also act as an optical filter preventing light absorbance by ZnS, and this inhibiting photoactivity (Reber and Meier, 1984). The quantum

efficiency calculated after a period of 60 minutes for the reaction given above is 73%, which is within the range for ZnS, but fairly lower than reported efficiency of 90% at 313 nm (Kudo and Miseki, 2009). However, when compared to a system operating under non-concentrating conditions, a measure of improvement is discovered. If for the same production of Figure 6.1, the input is assumed to be the number of photons that are incident under the same intensity of non-concentrating light, the effectiveness factors is almost 2. This proves the effectiveness of concentrating the light for hydrogen production.

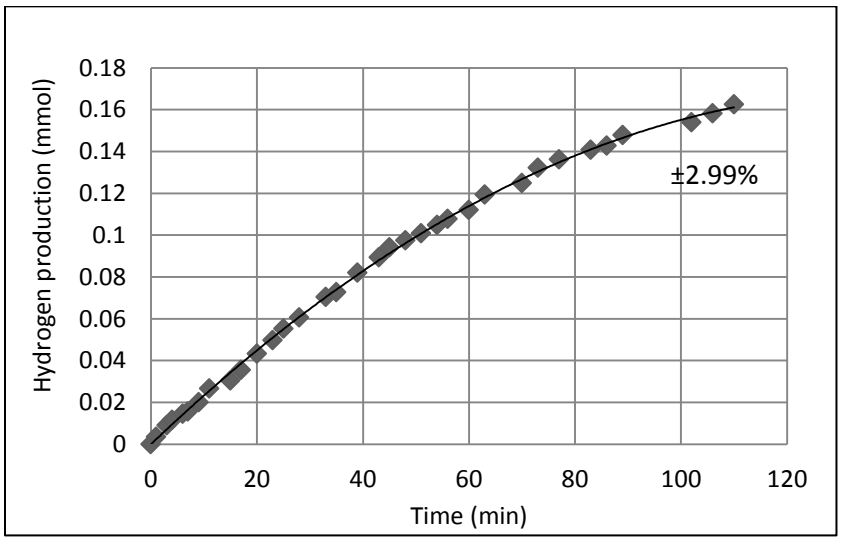

Figure 6.1: Photocatalytic hydrogen production from ZnS.

One reason that the efficiency of 73% is lower than the reported efficiency of 90% is that despite the concentration of light, the concentrated radiation has a smaller rate of photons per area than the non-concentrated radiation up until the 325 nm mark. This is due to the inefficiencies of the solar field, as shown in Figure 6.2, where the dotted line represents the reflected, concentrated radiation. Lower wavelength photons more efficiently instigate the photoreaction, due to the greater difference between their energy content and that required by the ZnS. Also, consideration needs to be given to the fact that the reported 90% yield is under monochromatic radiation, while here the experiment is performed over the full spectrum.

Variations in the absorbance with respect to wavelength result in lower efficiencies. Another factor may be that the production increases with concentration of light, but the increase is not linear.

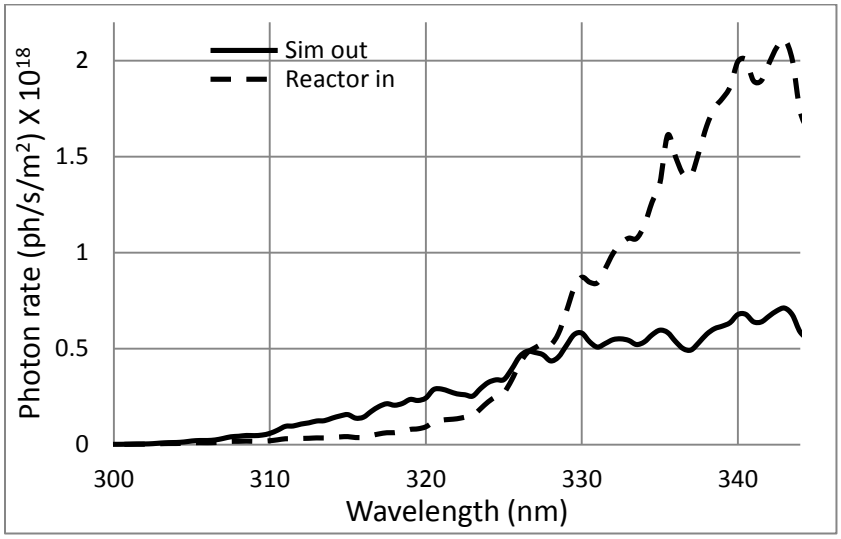

Figure 6.2: Photon rate for photons greater than ZnS bandgap.

One reason that the efficiency of 73% is lower than the reported efficiency of 90% is that despite the concentration of light, the concentrated radiation has a smaller rate of photons per area than the non-concentrated radiation up until the 325 nm mark. This is due to the inefficiencies of the solar field, as shown in Figure 6.2, where the dotted line represents the reflected, concentrated radiation. Lower wavelength photons more efficiently instigate the photoreaction, due to the greater difference between their energy content and that required by the ZnS. Also, consideration needs to be given to the fact that the reported 90% yield is under monochromatic radiation, while here the experiment is performed over the full spectrum. Variations in the absorbance with respect to wavelength result in lower efficiencies. Another factor may be that the production increases with concentration of light, but the increase is not linear.

The poor reflection of the high energy photons is due to the reflective properties of the mirror material used. The heliostats are made out of silver based household mirrors. Their reflective properties with respect to wavelength are shown in Figure 6.3, calculated based on compiled data (Palik, 1998). For visible light, however, the setup is sufficient for the purpose of demonstrating the dynamics of the photoreaction under concentrated light.

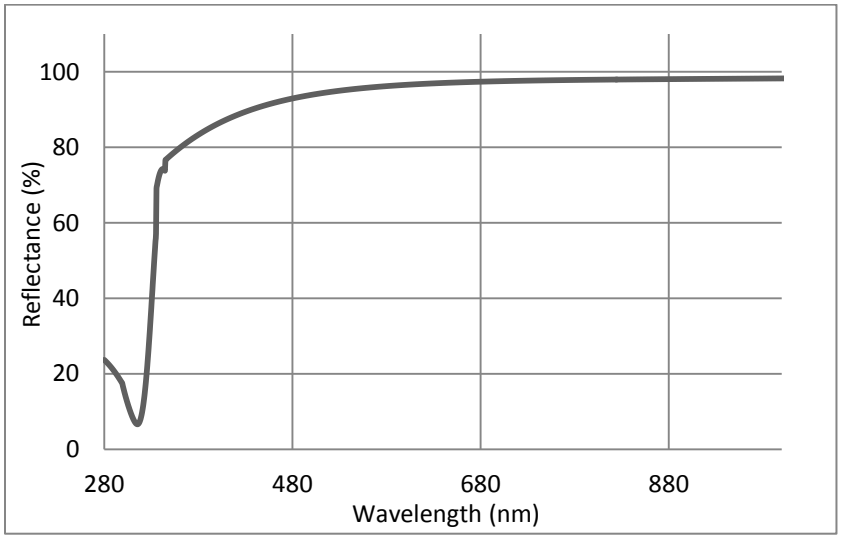

Figure 6.3: Reflective properties of heliostat material.

A comparison of reactor operation under constant pressure mode and constant volume mode is performed by illuminating 1.35 g of CdS catalyst in 90 ml of 0.3 M sulfide, and 0.2 M sulfite solution, under identical optical and operating conditions as described for ZnS. The two production curves are plotted in Figure 6.4. The low production in the case of the constant volume process is expected, as the increasing pressure shifts the equilibrium away from production of gaseous products. The production depends on the volume of gas space in the reactor. The curve of Figure 6.4 for the constant volume process is plotted at a storage volume of 27 ml. A larger gas space volume results in increased yield because the production of 1 mole of gas is accompanied by a smaller pressure increase as compared to the low volume case.

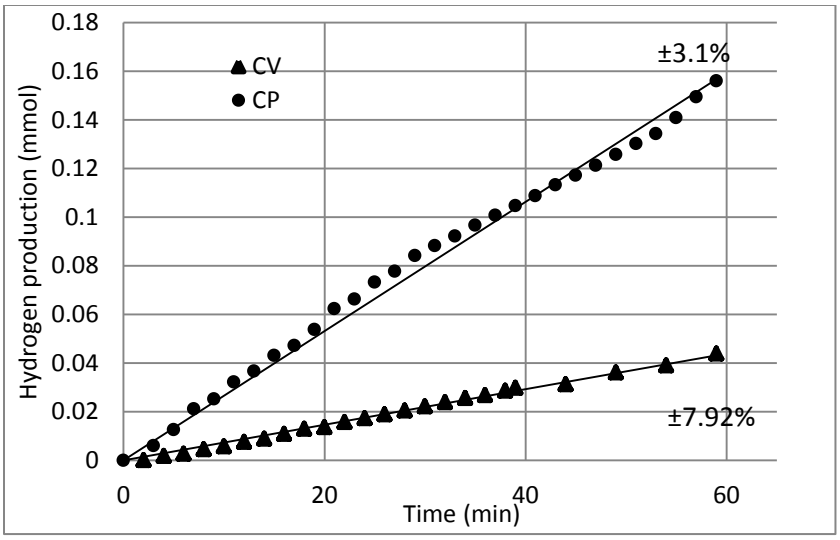

Figure 6.4: Comparison of constant pressure and constant volume operation.

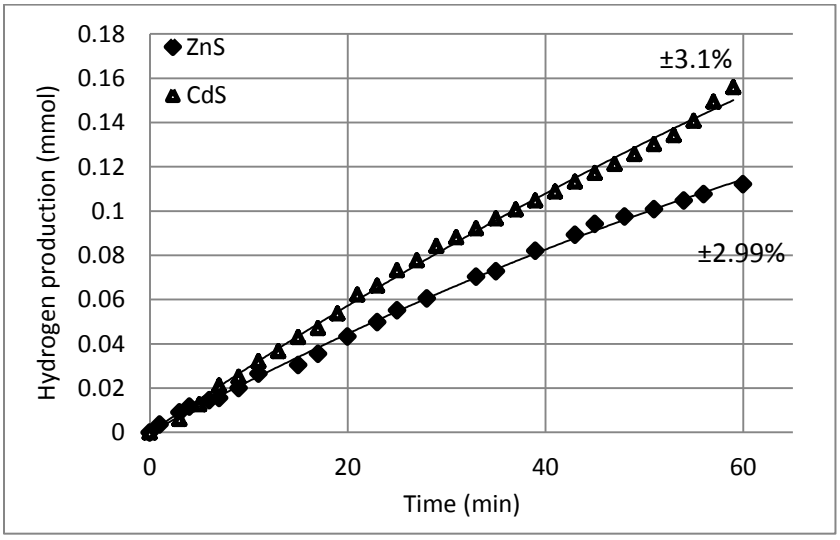

Figure 6.5: Comparison of ZnS and CdS.

A couple of things may be observed from the reaction using CdS. Figure 6.5 compares the processes with ZnS and CdS as catalysts respectively. The addition of sulfite ions to the electrolyte for the reaction with CdS shows their role in maintaining the reaction rate, by preventing formation of disulfide ions. It may be inferred that presence of sulfite ions in the ZnS reaction would result in a linear plot and a yield of hydrogen closer to that obtained for CdS. However, the superior performance of CdS as a visible light catalyst is indicated in consideration

of the fact that a lesser quantity of CdS produces comparable hydrogen to ZnS, while in an electrolyte with a lower concentration of sulfide ion electron donor.

Figure 6.6 shows the comparison of the photon spectra emitted by the solar simulator, and that reflected off heliostat field. With such a significant part of the absorbance spectrum of the CdS catalyst in the visible region, the poor reflectance of the silver mirrors in the UV region can be neglected. The complete spectrum over the range considered appears to be uniformly multiplied by the concentration factor. The quantum efficiency of CdS photocatalyst is reported at 0.06% for 0.1 g of catalyst under light of wavelength greater than 400 nm (Xing et al., 2006). For the constant pressure run of Figure 6.4, a catalyst amount of 1.3 g is used, which is in the magnitude of being 10 times larger than that used by Xing et al., and a similar scale of increase is observed in the quantum efficiency, which is 0.5% is achieved under the full concentrated spectrum. Again, to gage the effectiveness of the concentrated solar radiation and to compare with the non-concentrated case, the input is set as the rate of photons in to the system as if non-concentrated radiation is used. That gives an efficiency of 1.98%, indicating that the production achieved with the solar concentrator is almost 4 times larger. To evaluate the mechanism of the catalyst, the input is set as only those photons with sufficient energy to overcome the band gap (light shorter than 520 nm), and an efficiency of 1.48% is achieved.

The high quantum efficiency of ZnS within its band gap wavelength indicates that ZnS is more efficient at absorbing photons than CdS, but the smaller band gap of CdS allows it to be more productive under visible light. An experiment is conducted with a physical mixture of the two catalysts, in order to investigate whether greater efficiency may be achieved if ZnS absorbs the UV portion of the solar radiation and CdS the rest. The reactor vessel contains 1 g of CdS mixed with 0.3 g of ZnS, in a solution of 0.3 M sulfide and 0.2 M sulfite ions. The result is

plotted in 6.7. No discernible variation in performance is observed when compared to the experiment with CdS alone. This indicates that the difference in the absorbance mechanics of the two catalysts under UV light is not significantly different, and that experimentation with CdS alone under UV light only would result in similarly high quantum efficiency as ZnS.

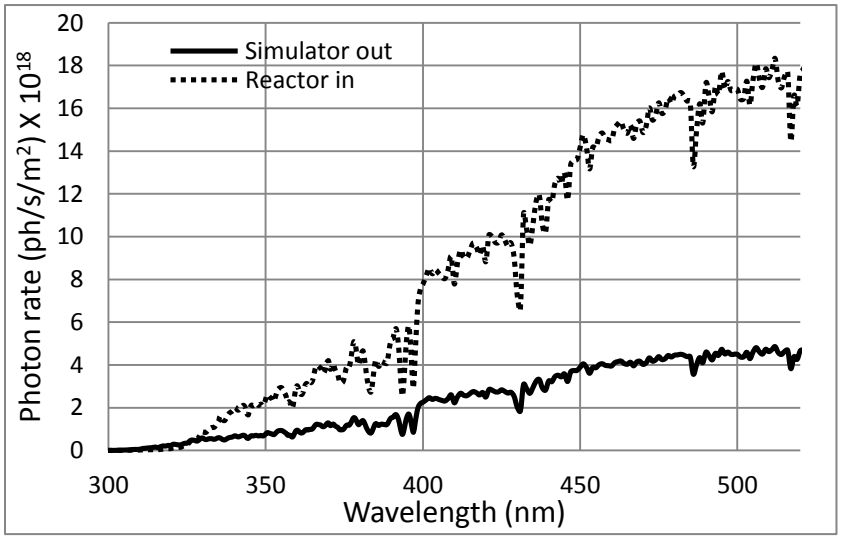

Figure 6.6: Rate of photons greater than CdS band gap.

The method described in section 4.3 for de-aerating and isolating the solution is designed in order to prevent photocorrosion of the metal sulfide catalyst, and allow its usage over a long period of time. The effectiveness of the method is evaluated by performing a long run experiment where the catalyst within the reactor is maintained. In order to ensure that any variation in rate is solely due to catalyst de-activation, the electrolyte is refreshed after every hour, using the flow system described in section 4.4. The cylinder is purged of hydrogen gas every time the electrolyte is refreshed. The electrolyte used contained 0.3 M sulfide solution and 0.2 M sulfite solution. A catalyst combination of 1 g of CdS and 0.3 g of ZnS is used, and the reactor temperature is maintained at 25 ºC. The results are plotted in Figure 6.8 for an effective 6 hour run. The closeness of the results obtained shows that the catalyst remains activated, and that the experimental procedures described and implemented are effective. For the curve for hour 4, it

appears that the yield is low, but that is not the case as the case, as after an initial period of low production, the production rate stabilizes again. So too, the curve for hours 5 and 6 show that activity is maintained, confirming that the drop in hour 4 is due to other, probabilistic reasons, and not catalyst de-activation.

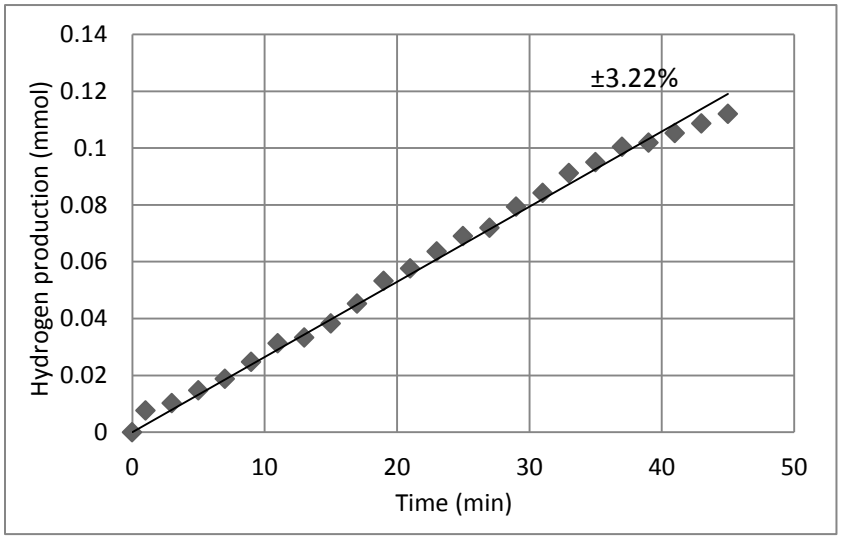

Figure 6.7: Hydrogen production with CdS ZnS physical mixture.

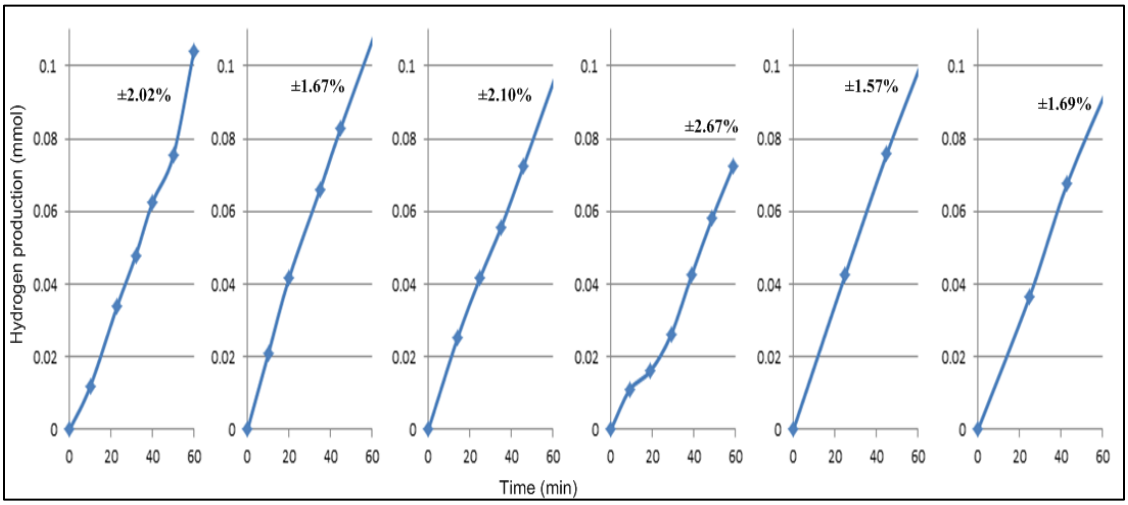

Figure 6.8: Photocatalytic hydrogen production: 6 hour run with 1 hour refreshing of solution.

During the experimental runs for Figure 6.8, an OceanOptics spectrometer with a fibre optic cable is used to compare the spectra in front of the photo catalytic reactor and behind the

reactor inside the cavity receiver. Figure 6.9 shows the two spectra superimposed for comparison.

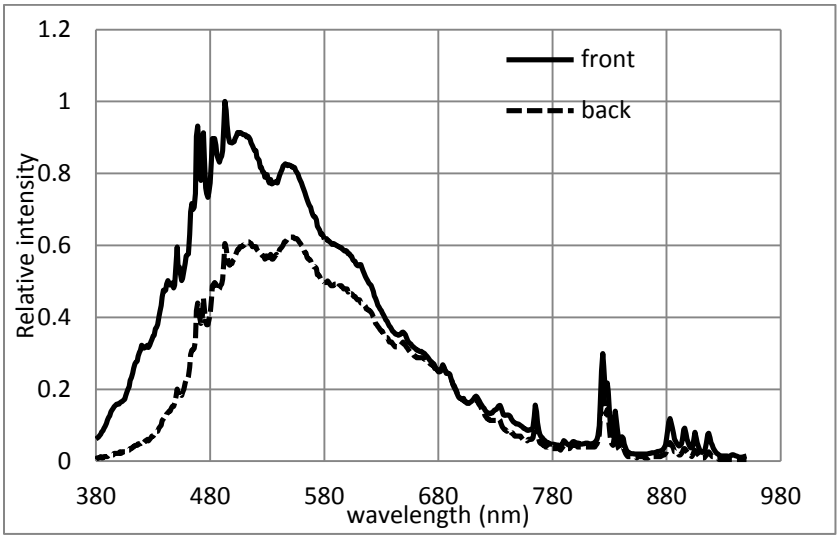

Figure 6.9: Emission spectra of solar simulator in front and back of photoreactor.

Expectedly, the majority of the absorbed radiation is at the shorter wavelengths. The photoreactor absorbs radiation efficiently up to 520 nm, and the PV cells are meant to absorb from 500 nm up to 1000 nm. In Figure 6.10, the absorbed fraction is compared to the absorbance of CdS. To a large extent, the fraction absorbed matches the absorbance of the CdS catalyst, although it would be expected that a larger fraction would be absorbed from about 480 nm – 520 nm, since that corresponds to a high absorbance for CdS, and also falls within the range of absorbance by the PV cells. The most likely reason in the case of the photoreactor is that there may be saturation of light, due to the concentration of light, which results in reflection of the higher wavelength radiation. Some direct radiation may also be incident on the cable, skewing the curve. In the case of the PV cells, it is shown that generally, the spectral response is poor at shorter wavelengths, increases gradually until it peaks at 900 nm, then starts dropping rapidly (Reich et al., 2005). The fraction absorbed at higher wavelengths in Figure 6.10 appears to follow this trend.

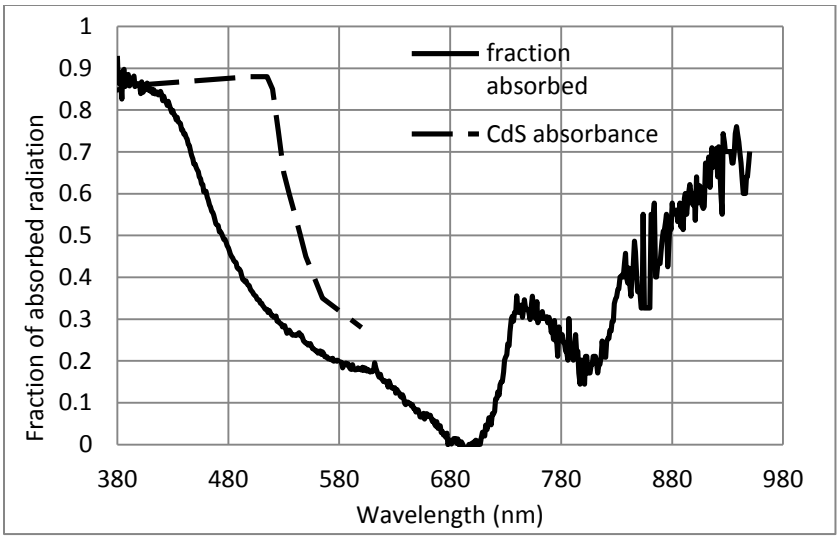

Figure 6.10: Fraction of radiation absorbed within cavity receiver and CdS absorbance spectrum.

Due to the low cost nature of the PV cells used, and hence expectedly poor performance, it can be inferred that the lack of absorbance around 680 nm occurs due to the spectral response being pushed further towards the larger wavelengths. High quality cells are designed to allow a better spectral response at the shorter wavelengths, but this is not the case here.

6.2 Mechanism of Photo-catalysis and Experimental Details

Photocatalytic water splitting is performed by illuminating a suspension of colloidal catalyst in the reactor described earlier. The reactor contains 90 ml of solution, and the illumination source is a solar simulator operating at 1200 W/m^2. The catalyst used is a combination of 0.3 g of zinc sulfide (ZnS w/v 0.33%) and 1 g of cadmium sulfide (CdS w/v 1.11%). This is kept fixed as a parametric study for some variables is performed for the reaction. A solution containing 0.3 M of sulfide ions (S^{2-}) and 0.2 M of sulfate ions (SO_3^{2-}) is used, as it is established as the optimum solution for the hydrogen half reaction. The following reactions take place in the solution for the production of hydrogen, as described by Zamfirescu et al. (2013). At the conduction band, water receives electrons from the catalyst to form hydrogen according to the following:

$$2H_2O + 2e^- \rightarrow H_2 + 2OH^- \quad (6.1)$$

At the valence band, the sulfide ion loses its electrons to the catalyst as follows:

$$S^{2-} \rightarrow S + 2e^- \quad (6.2)$$

The solid sulfur inhibits the progression of reaction by depositing on the catalyst and causing inactivation. The presence of sulfate ions allows the following reaction to occur spontaneously as follows:

$$S + SO_3^{2-} \rightarrow S_2O_3^{2-} \quad (6.3)$$

The overall reaction for the production of hydrogen is as follows:

$$2H_2O + S^{2-} + SO_3^{2-} \rightarrow H_2 + 2OH^- + S_2O_3^{2-} \quad (6.4)$$

The solution is stirred by means of a magnetic stir bar placed inside the reactor and activated by a stirrer placed affixed under the reactor vessel. The hydrogen is collected at constant pressure, by employing a servo-controlled piston cylinder device that senses pressure increments to adjust its volume accordingly. The increment in the height of the vertical piston cylinder device is measured using a digital caliper attached to the device, and read off manually. Figure 6.11 shows the production of hydrogen at a pressure of 8.9 psi (61 kPa) and a reactor temperature of 298 K.

As shown in Figure 6.11, each experiment is performed three times to establish an error gap. This error is due to the inherently probabilistic nature of the experiments, which causes variations in the rate of encounter with desirable or undesirable species present in the solution, and creates an impact which is observable at this small scale. For an experiment at a larger scale,

this impact is not likely to be as observable. The error band is inclusive of the uncertainty from the measurements taken from the equipment, and discussed earlier. For the set of experiments performed and analysed here, the maximum variation of 14% is observed in the results for 1 set of experiments. Though this value may appear significant compared to the scale of the results that are obtained, it is sufficient for the purpose of study here. Upon variation of parameters that are studied here, clear patterns emerge that establish the relationships between the output and the parameters.

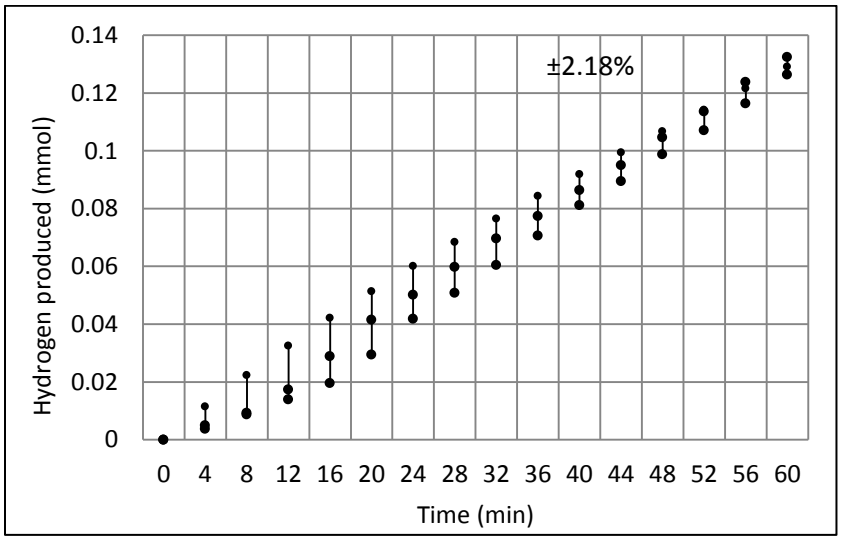

Figure 6.11: Hydrogen production versus reaction time shown with error band gap.

The production rate is linear for the batch process, despite no addition of fresh solution into reactor. This is understood by considering at the concentrations of the species present in the solution. The rate is determined by the quantity of the electron donor present, S^{2-} or SO_3^{2-} in this case, and the relative quantities of the other undesired species, which would be the products of the reaction, namely OH^-, $S_2O_3^{2-}$, and SO_4^{2-}, in varying quantities. At the start of the reaction, the solution contains 25 mmol of sulfide ions and 17 mmol of sulfite ions. For the main process route of the reaction, when the amount of hydroxyl ions present is low, the reaction involves the use of 1 mol of sulfide and 1 mol of sulfite per production of 1 mol of hydrogen gas. Based on

the production of hydrogen from Figure 6.11, and the initial quantities of the electron donors, the change in make-up of the solution is not enough to cause a drop in the reaction rate.

6.3 Pressure Variation

The production of hydrogen gas is plotted against reaction time for three different values of pressure in Figure 6.12. The highest pressure is set to the atmospheric pressure, which results in 0.1 mmol/h of hydrogen gas production. The production is observed to increase as the pressure is decreased. At an absolute pressure of 61 kPa, the production increases to 0.13 mmol/h. A further decrease in pressure to an absolute value of 21 kPa enhances the production rate to 0.16 mmol/h. The quantum efficiency increases from 0.94% at 101 kPa to 1.2% at 61 kPa, and further to 1.52% at the lowest pressure. The increase in efficiency from the highest pressure to the lowest pressure is by 62%.

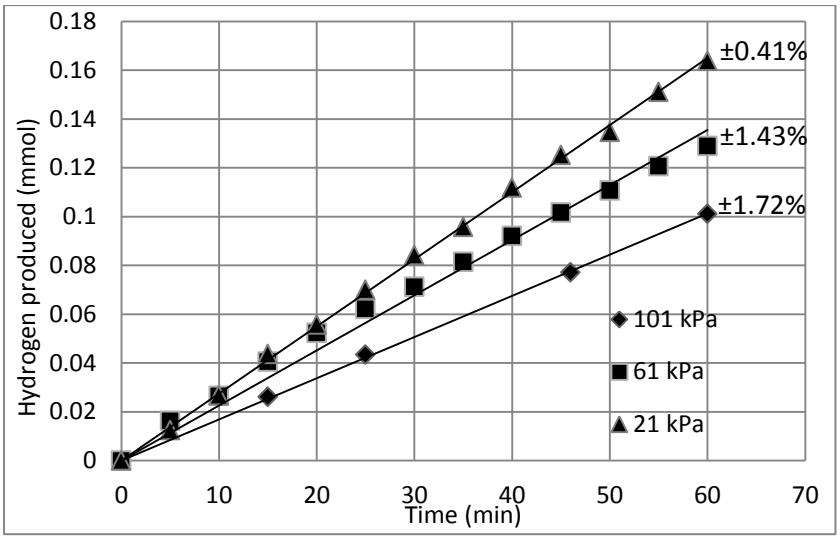

Figure 6.12: Variation of photocatalytic hydrogen production with reactor operating pressure.

The increase in the production of hydrogen is expected as the pressure is decreased. The chemical equilibrium of a reaction shifts in order to accommodate the change in pressure, according to Le Chatelier's principle. In reactions that involve a gaseous substance, this is

achieved by shifting the reaction towards greater availability of the gas. In this case, the reduction in pressure pushes the equilibrium towards greater hydrogen production. Zamfirescu et al. (2013) predicts an increase in the production rate in vacuum as that would allow a lower concentration of dissolved bubbles in the liquid, and thus a greater efficiency. The hydrogen bubbles also act as undesirable species in the electrolyte, and impede the reaction.

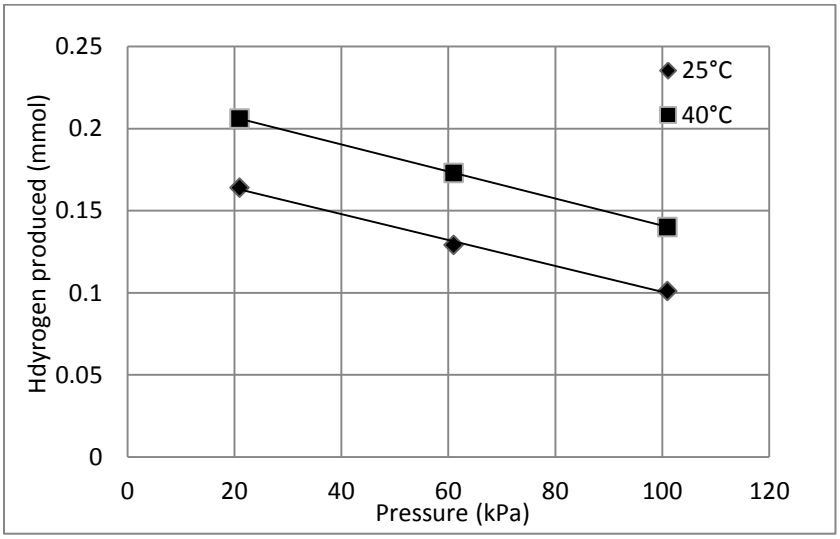

Figure 6.13: Photocatalytic hydrogen production: Final yield variation with pressure for different temperatures.

Figure 6.13 shows the variation of the final yield with pressure for each temperature. The trend for the variation appears to be linear for both temperatures. It is possible that at higher pressures than that shown on the graph, the variation ceases to be linear, but assumes a rather more exponential shape. However, as the performance is better at lower pressures, this is the range of concern, and in this region, the linear relationship is justified. The pressure coefficient obtained at both temperatures is equal. A value of -0.0008 mmol/kPa is obtained. Knowing the yield at a single pressure point for any operational temperature thus allows a prediction of the yield as the pressure is varied.

6.4 Temperature Variation

The production of hydrogen gas is observed to increase further as the operating temperature is increased. Figure 6.14 shows the plot of two experiments at different temperatures, at a pressure of 21 kPa.

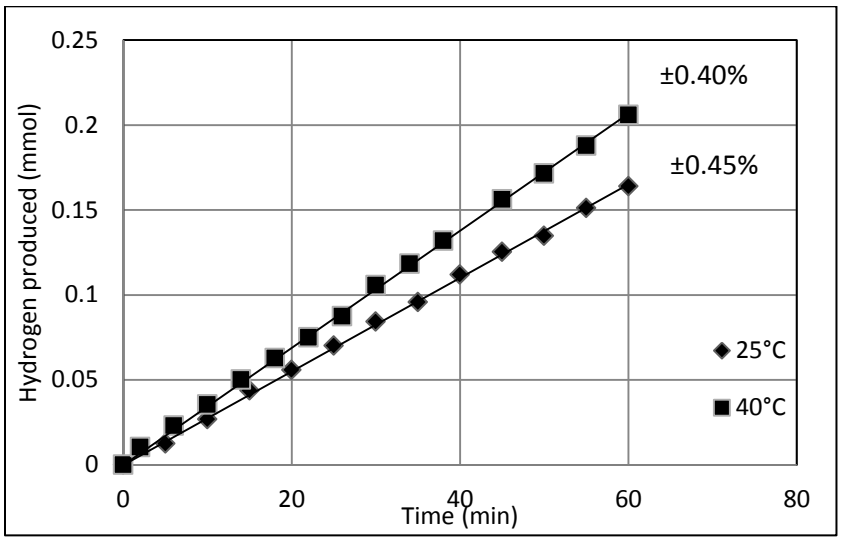

Figure 6.14: Photocatalytic hydrogen production at 21 kPa for two different temperatures.

An increase of 10 K in the operating temperature results in an increase of 26%, from 0.164 mmol to 0.206 mmol. The water splitting reaction at the temperatures studied requires a portion of energy in the form of work, and another portion in the form of heat. The reaction, thus, is an endothermic reaction, as well as being an uphill reaction. At a lower temperature, the thermal energy requirement may be fulfilled by a portion of the photons. At a higher temperature, the reaction is able to absorb a larger quantity of thermal energy from the environment, thus accelerating the water splitting process. Similar results are obtained when the process is executed at different temperatures at 61 kPa and 101 kPa, as shown in Figures 6.15 and 6.16.

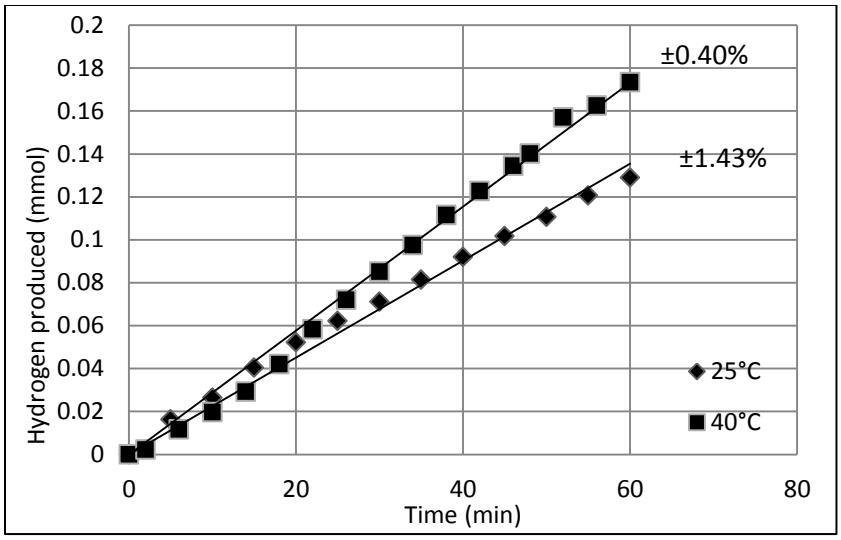

Figure 6.15: Photocatalytic hydrogen production at 61 kPa for two different temperatures.

For the process at 61 kPa, the quantity obtained increases from 0.129 mmol by 34% to 0.173 mmol when the process temperature is increased by 10 K. At a process pressure of 101 kPa, the amount of hydrogen produced increases from 0.116 mmol by 37% to 1.35 mmol when the temperature is increased by 10 K.

It is shown that the yield of hydrogen increases linearly as the temperature is increased, and that the temperature coefficient remains constant at different concentrations of the electron donor (Reber and Meier, 1984). Therefore, for this case, the temperature co-efficient may be obtained using the results of the yield at the two different temperatures. Figure 6.17 shows that at all pressures, the temperature coefficient remains the same.

6.5 Variation of Electrolyte Concentration

As the concentration of the electrolyte is decreased, the yield at the end of the time period chosen for study, and also the initial reaction rate, decreases. A better understanding of the rate dynamics is achieved by studying the progression of the reaction at lower concentrations. Figure 6.18 compares the production of hydrogen with respect to time for three different concentrations.

At the highest concentration of 0.3 M, the production is almost linear for the time period. This is because the production rate of hydrogen is small, and due to the large amount of electron donor present in the solution, the change in the solution composition is not large enough to decrease the reaction rate. When the initial concentration of the solution is decreased, the parabolic shape of the plot is more visible.

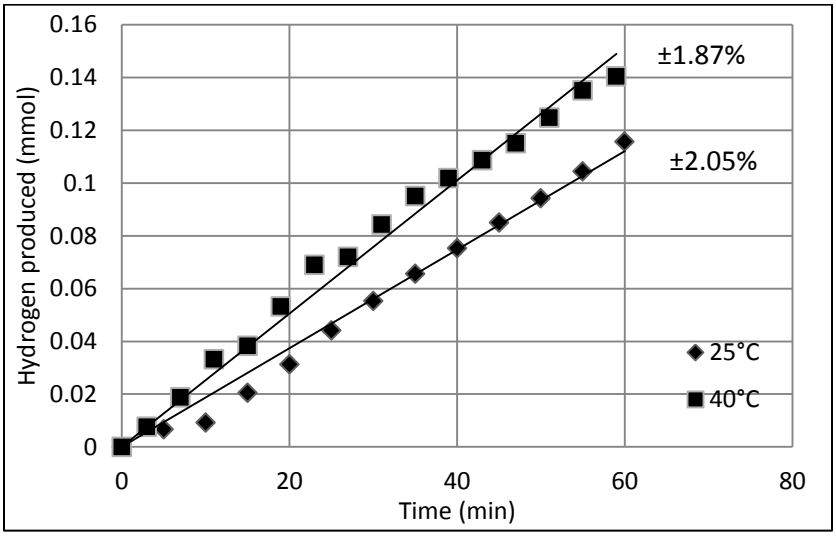

Figure 6.16: Photocatalytic hydrogen production at 101 kPa for two different temperatures.

As the reaction progresses the variations in the ionic species are sufficient to effect a change on the rate. For the smallest concentration of 0.003 M, the initial quantity of sulfide ion present is 0.25 mmol. After 10 minutes, at which point the reaction rate has decreased considerably, approximately 0.007 mmol of sulfide ion have been consumed and 0.014 mmol of hydroxyl ion produced. Since the probability of desirable collisions depends on both these factors mentioned, it becomes apparent that sum of that change, 0.021 mmol, is large relative to the initial quantity of sulfide ion present.

The initial reaction rate also decreases for each successive reduction in the concentration of solution, due to the lower initial concentration of electron donors present, and hence, the lower probability of wanted collisions that initiate a reaction. Considering the first couple of minutes of

the reaction to be linear, based on the experimental results, the initial reaction rates can be calculated to be 0.0019 mmol/min, 0.0015 mmol/min, and 0.0011 mmol/min for the concentrations of 0.3 M, 0.03 M, and 0.003 M respectively. If the initial rates are plotted against the concentration, as shown in Figure 6.19, it can be inferred that the variation follows a logarithmic curve. This is further confirmed by cross checking with results presented by Reber (1984).

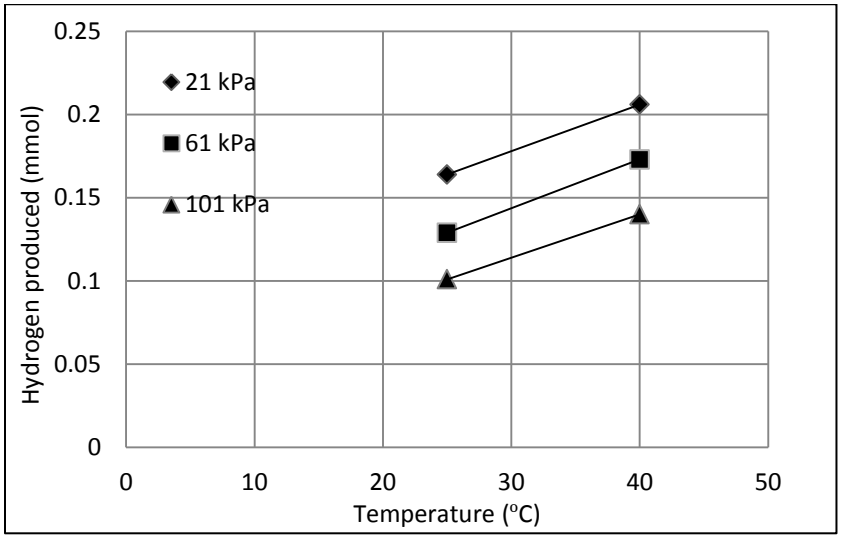

Figure 6.17: Photocatalytic hydrogen production variation of yield with temperature for various pressures.

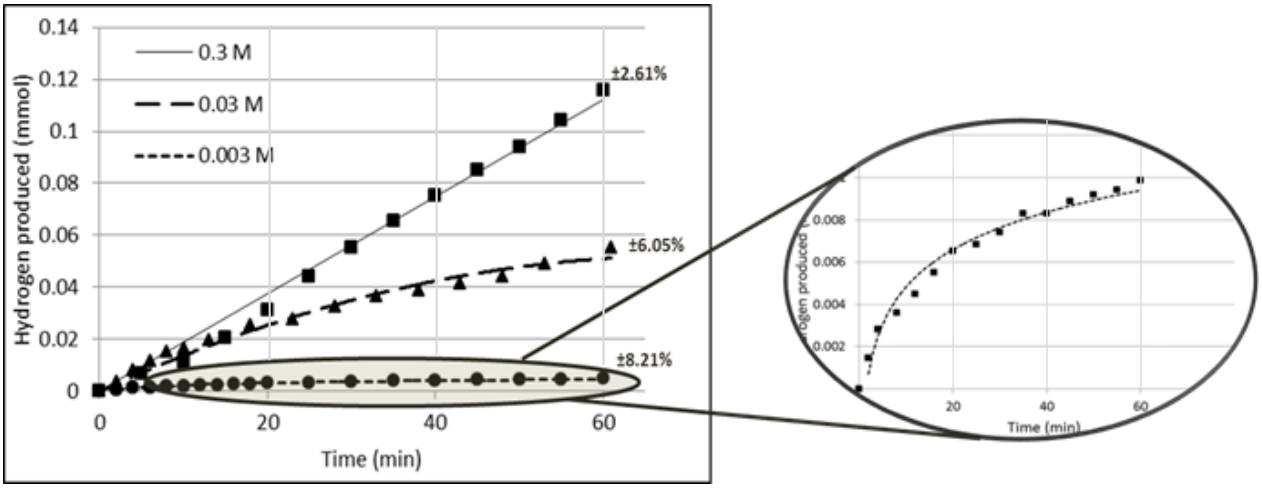

Figure 6.18: Photocatalytic hydrogen production comparison at different electrolyte concentrations.

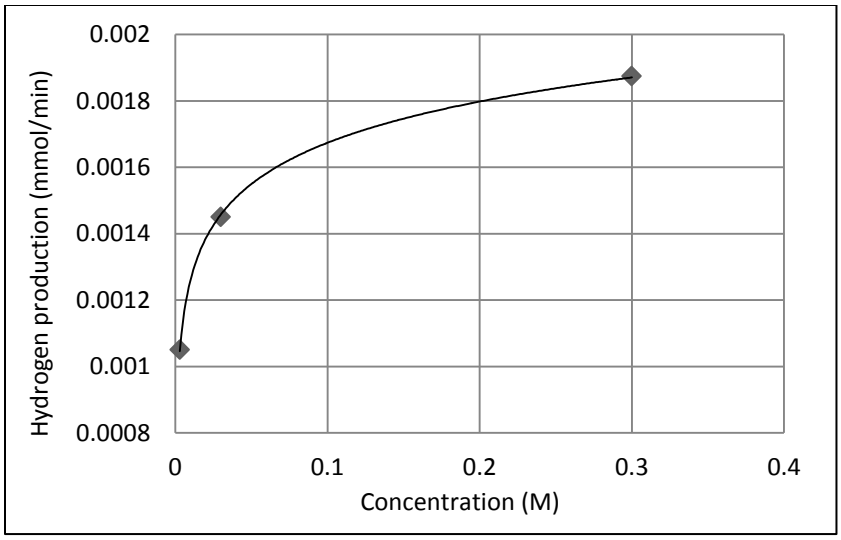

Figure 6.19: Photocatalytic hydrogen initial production rate against initial sulfide concentration.

Figure 6.19 shows that increasing the concentration of the solution is only beneficial up to about 0.1 M. Beyond this point on the plot, the initial rate of the reaction does not increase steeply, and may not be enough to justify the increased complexity of a system of higher concentration. For the batch product, the productive reaction time is longer at higher concentrations, and so is the final hydrogen quantity achieved after 60 minutes, but from the point of view of a continuous flow process, the initial reaction rate is more important than the batch process product.

6.6 Model Validation

Based on the experimental results obtained, and the mechanics of the process, a model is created that is able to simulate the photocatalytic hydrogen production process for a variety of molar concentrations over any length of time, for both batch and continuous processes. The validation is performed by comparing the results of the simulation to the further experimental results, different from the ones used to develop the model.

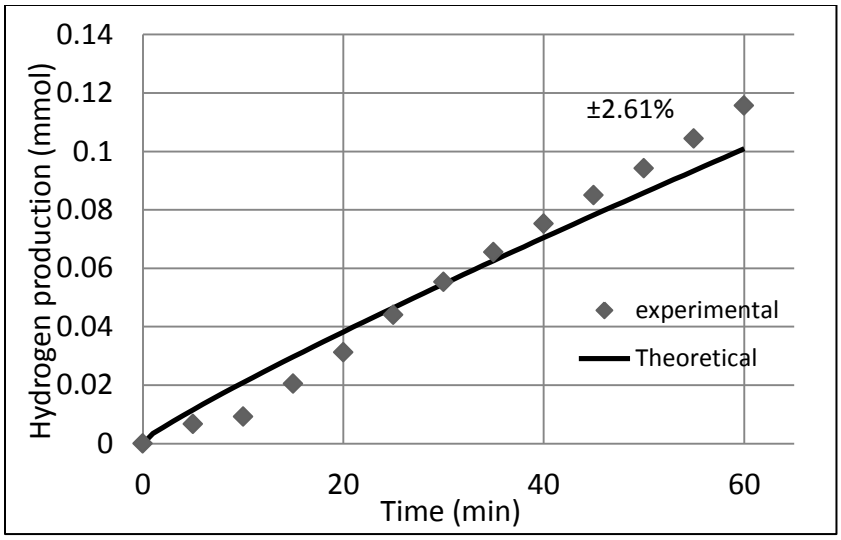

Figure 6.20: Photocalatytic hydrogen production simulated results superimposed with experimental results at 0.3 M sulfide solution.

Figures 6.20 – 6.23 show the simulated results for different electrolyte concentrations with the experimental results superimposed. The plots clearly show that the model that is derived suitably simulates the photocatalytic hydrogen production process, for the given experimental conditions (reactor design, pressure, temperature, catalyst concentration). This allows the model to be used to simulate hydrogen production for a continuous flow reactor.

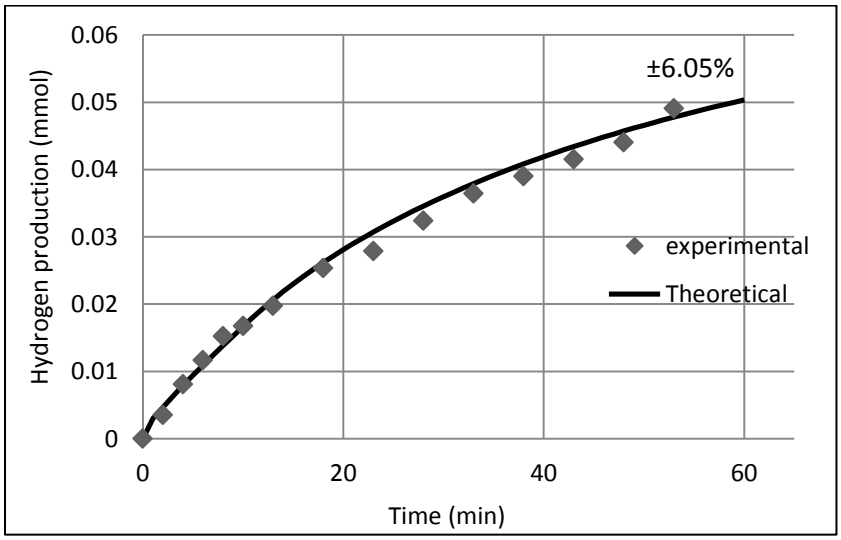

Figure 6.21: Photocatalytic hydrogen production simulated results superimposed with experimental results at 0.03 M sulfide solution.

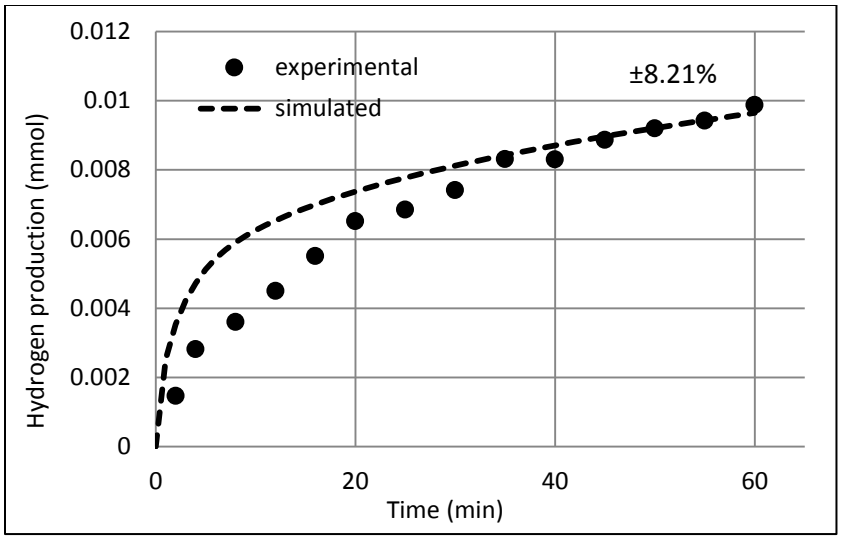

Figure 6.22: Photocatalytic hydrogen production simulated results superimposed with experimental results at 0.003 M sulfide solution.

6.7 Simulation of Processes

The theoretical process model that is developed and validated is used to simulate further processes. The model is used to simulate the photocatalytic process at different concentration levels of the sulfide ion. The concentration of sulfite ions is not considered a variable and the concentration ratio of sulfide-sulfite ion is maintained. Flow processes are also simulated and the effects of electrolyte flow rate on the hydrogen production rate are investigated. The model allows avoidance of conducting excessive experiments.

6.7.1 Batch Processes

Figure 6.23 shows the progression of the process at various concentration levels. The combined effect of the depletion of sulfide ions and the addition of hydroxyl ions on the reaction starts to become visible in the first hour after below an initial concentration of 0.3 M sulfide ions. The variation in the reaction rates for the first 5 minutes of the process is very small for all concentrations, and may be considered linear. Figure 6.24 gives the initial rate, calculated as the yield in the first 5 minutes divided by that time period, against the concentrations for various

electrolyte concentrations simulated in Figure 6.23. Figure 6.24 proves what was inferred previously based on the plot of Figure 6.19. The increase in the initial rates is indeed logarithmic as the concentration is increased. It appears that the optimal concentration to employ for the electrolyte is between 0.03 M and 0.1 M for a continuous flow process. This is discussed further later on.

Figure 6.25 extends the reactions of higher concentrations in Figure 6.23 over a greater time period. This allows the selection of the optimal electrolyte concentration for the implementation of a batch process. Beyond 1 M sulfide ion concentration, the reaction rate does not show any increase (Reber and Meier, 1984). A solution of concentration 0.1 M is not suitable, due to the short time during which the reaction rate maintains itself. 0.085 mmol of hydrogen is produced in the first hour, followed by 0.045 in the second hour, which is a drop of almost 50%. For an electrolyte concentration of 0.3 M, the production in the first hour is 0.1 mmol of hydrogen, drops to 85% in the second hour, 70 % in the third, and 50% in the fourth. For a 0.6 M concentration, the production drops to 86% in the second hour, is maintained for the third hour, when it is 83% of the original, then drops sharply to 72% in the fourth hour.

It turns out that length of the batch process is determined by the solution degradation variable $'a'$. Since the reaction rate is logarithmic with respect to a, as given in section 5.4, the reaction drops of sharply at the point at which the degradation variable reaches the bend in the logarithmic graph. At this point, the batch requires a recharge to continue efficiently. Figure 6.26 shows the variation of the hydrogen production rate for various electrolyte concentrations.

The selection of electrolyte concentration depends on the operation time for the batch process. Supposing that an 8 hour operation per day is required, based on the availability of sun

light, then a 1 M electrolyte concentration would be the most suitable with a yield of 0.72 mmol in that time. Conversely, an electrolytic concentration of 0.6 M may be run for a total of 8 hours with a recharge, giving the same output, but hardly justified.

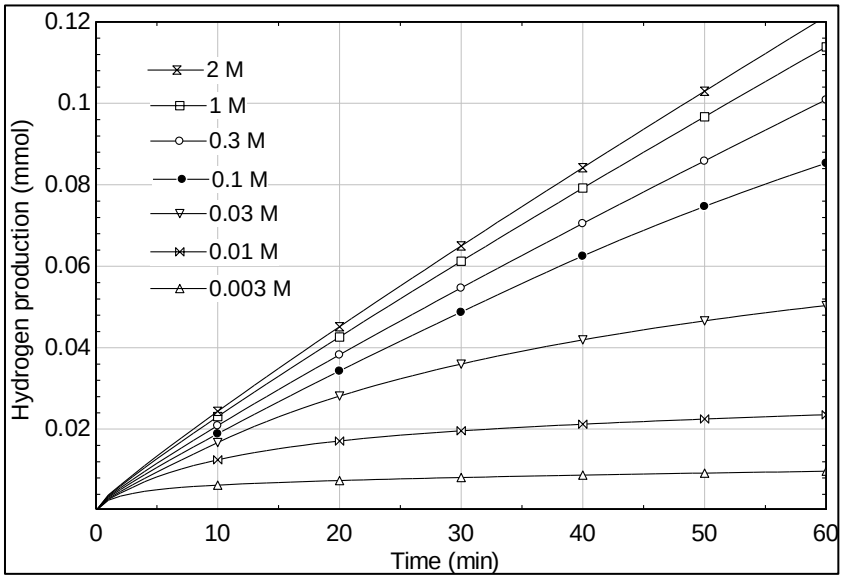

Figure 6.23: Photocatalytic hydrogen production simulations for various concentrations.

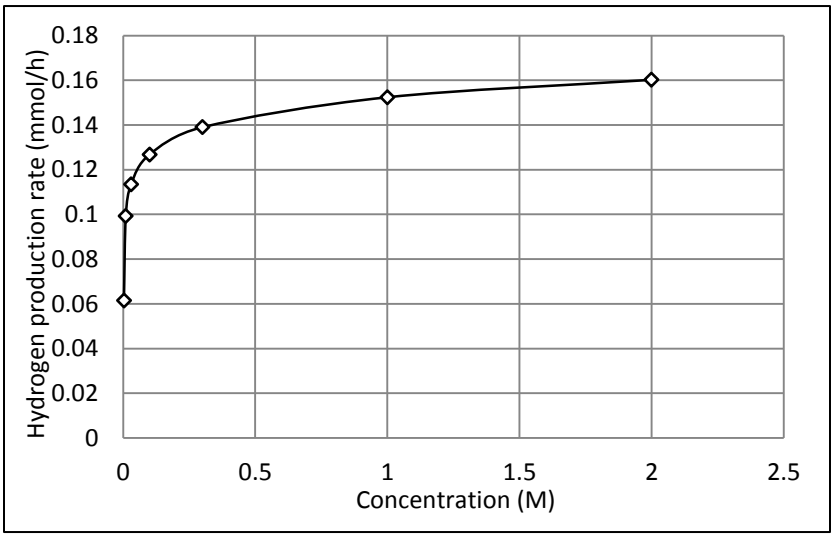

Figure 6.24: Photocatalytic hydrogen production: variation of initial reaction rates with initial sulfide ion concentration.

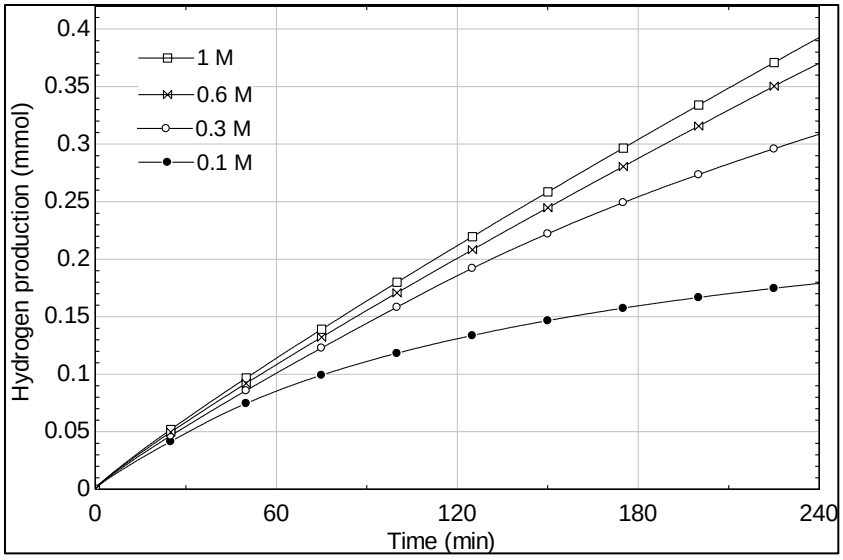

Figure 6.25: Photocatalytic hydrogen production for higher sulfide ion concentrations with respect to time.

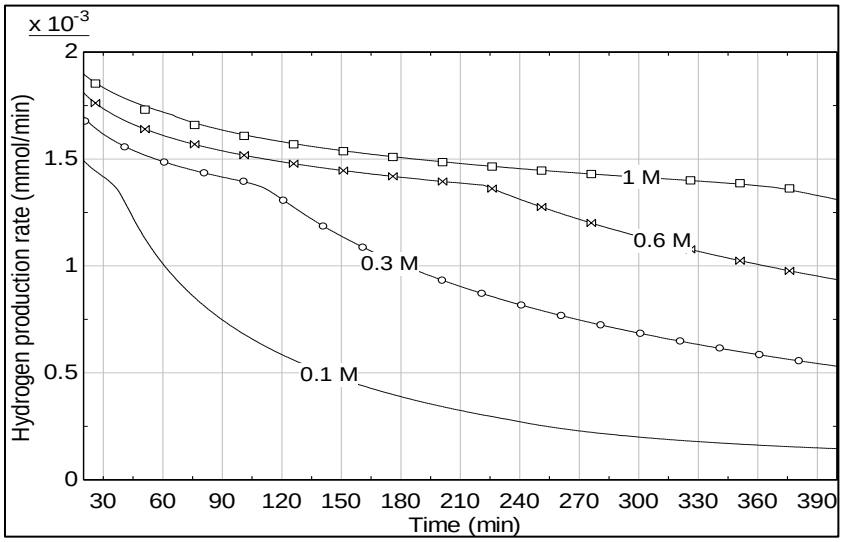

Figure 6.26: Photocatalytic hydrogen production batch process reaction rates for various concentrations.

6.7.2 Continuous Flow Process

A continuous flow process allows the rate of reaction to be maintained by attempting to maintain the solution degradation variable, described in section 5.4, to a desired value. The model is extended by integrating the rate equation into the differential equations for a continuous stirred tank reactor (CSTR). Figure 6.27 shows the steady state reaction rates for hydrogen

production plotted against volume flow rate of electrolyte for various concentrations. The relation for each concentration is logarithmic in nature, so that there is an optimum flow rate for each concentration beyond which the size in the increment of the reaction rate with increased flow is not justified.

Also noticeable from the plot is that for a common value of the reaction rate, the variation of flow rate required with the electrolyte concentration is also logarithmic in nature. For a reaction rate of 0.0024 mmol/min, a three-fold decrease in concentration results in a decrease in the flow rate requirement from 125 ml/h to 50 ml/h approximately, while a further three-fold increase in the concentration brings down the flow rate requirement from 50 ml/h to 15 ml/h. This agrees with the initial rate values shown in Figure 6.24 for the batch process. Of course, as the desired steady state is reached, all concentrations of electrolyte essentially have the same number of ions flowing through the reactor for a given amount of time, so the selection depends on the trade-off between the difficulties of handling a concentrated solutions, or those associated with handling a larger volume of solution flowing through the pump. Also included in the consideration may be the increased chances of corrosion with higher concentration, and the relation of heat exchanger effectiveness to the flow rate, if hot water or hot is to be a desired part of the hybridized set-up.

6.8 Photovoltaic Model Validation

For Equation 5.20, described earlier for PV characteristic curves, to be used, the shunt resistance (R_{SH}), series resistance (R_S), and the non-ideality constant (n) for the cell need to be determined empirically. This is done by experimentally determining the curve for a given value of intensity, and fitting the equation to that curve. The model is then validated by comparing it to a second set of experimental data taken.

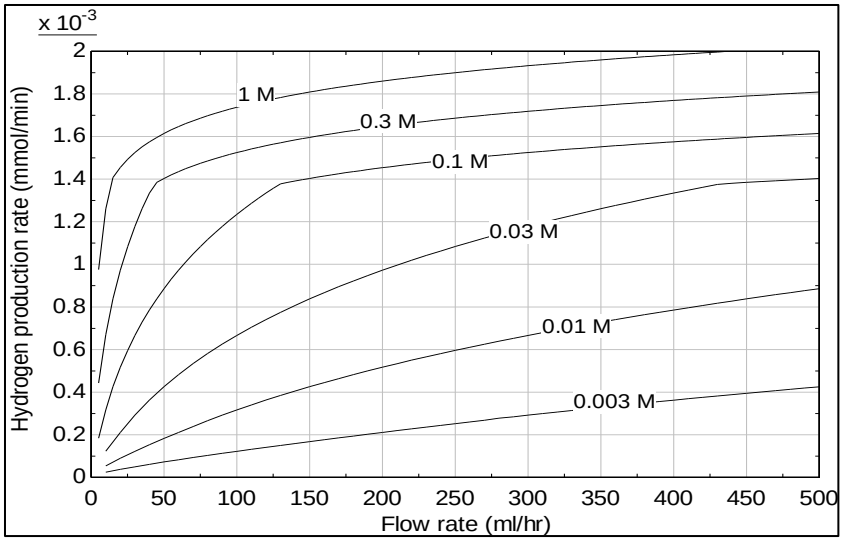

Figure 6.27: Photocatalytic hydrogen production steady state reaction rate against flow rate.

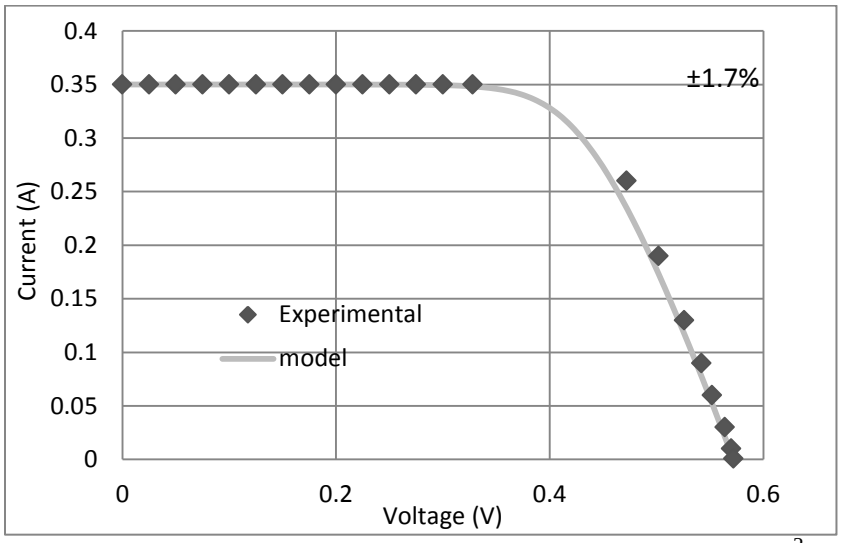

Figure 6.28: Photovoltaic characteristic curve at 1200 W/m^2.

Figure 6.28 shows the experimental data used to fit the model, and the corresponding model curve, while Figure 6.29 shows the comparison of the experimental data and the model curve for a second set of readings, for validation purposes. Both curves show an extremely good fit to the experimental data. The values obtained for n, R_{sh}, R_S are 1, infinity, and 0.3 Ω respectively.

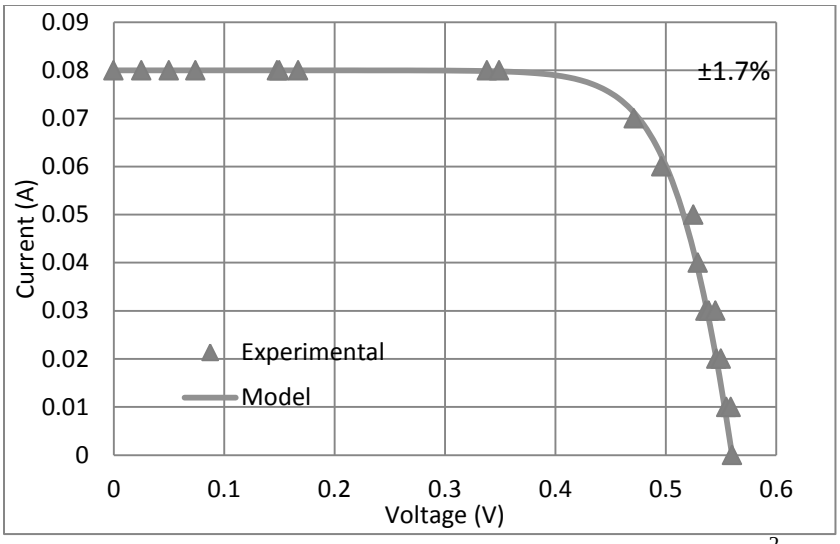

Figure 6.29: Photovoltaic characteristic curve 266 W/m^2.

6.9 Photovoltaic Power Output

In order to increase the efficiency of the photocatalytic process, PV cells are installed inside the walls of the tower housing for photon harvesting. Nine columns of cells are installed, with each column containing two cells. The two cells in each column are connected in parallel, as it is assumed that in that vertical space the solar irradiation will be close to equal. Each column is left unconnected, so that their I-V curves can be determined later and they can be connected as desired to obtain an appropriate overall I-V curve. The individual column curves are obtained by measuring the values of open circuit voltage and short circuit current and plotting the curve using the model of Equation 5.20 and the parameters determined earlier. Figure 6.30 shows the positioning of the columns with labels, while Figure 6.31 shows the corresponding characteristic curves.

Three columns of cells line either side of the cavity receiver, and three columns line the back end. The output from each column on the sides is equal to the corresponding column on the opposite side. This is expected as the set-up is designed to be symmetrical. The three columns on

the back end of the cavity receive the same irradiation and produce the same output. This output is the lowest compared to the other cells, since the cells sit behind the reactor and they receive predominantly diffused radiation. Columns 3 and 7 produce a slightly larger output as there is likely some reflected light incident on the cells. The highest output is exhibited by columns 1, 9, 2, and 8. It is likely that some direct irradiation is incident on these columns. The behaviour of these two columns requires explanation. Their open circuit voltage is equal, yet the short circuit currents differ.

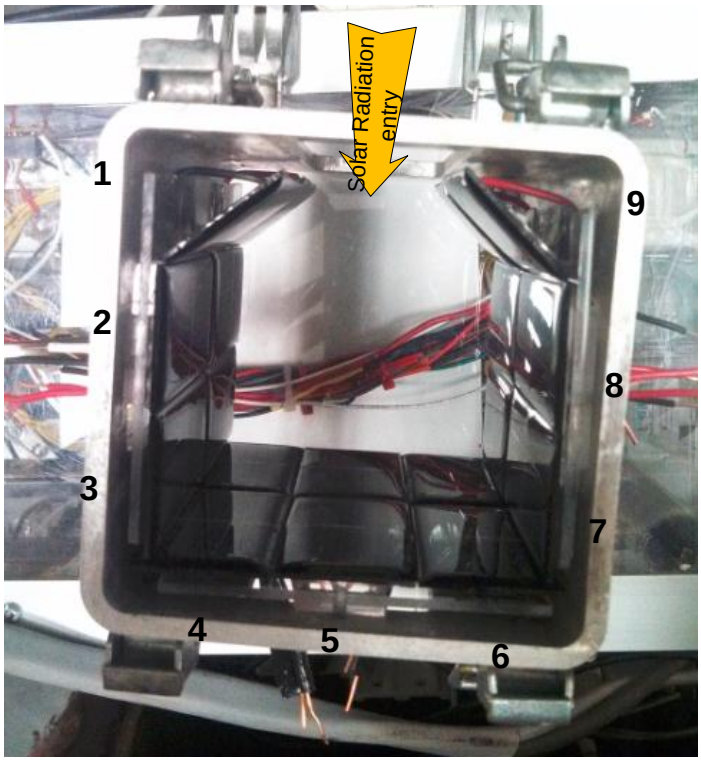

Figure 6.30: Positioning of the columns with numbers, as indicated on plots.

As mentioned earlier, two cells in each column were connected in parallel under the assumption that the incident radiation on them would be equal. However, this appears not to be the case. Consider column 2 and 8. The following explanation applies to both due to the symmetry. For a single cell with the given open circuit voltage, the short circuit current

measured is 0.1 A. So, for two cells in parallel, it should have been 0.2 A. Here, the parallel combination has a current value of 0.13 A, in between the two values. This indicates that one of the parallel cells actually receives more radiation than the other. Due to the parallel arrangement, the voltages of the two cells must be equal. So the total voltage across the cells is a value between the voltage for the higher cell and the lower cell. The total current then is simply the sum of the currents of either cell. An educated guess based on the geometry of the light rays is that the upper cell receives greater radiation. In this case, power is dissipated due to the difference in the irradiation on both cells. If they were disconnected and each measured separately, it is expected that the upper cell would have an open circuit voltage greater than 0.556 V, and the corresponding current, while the lower cell would show an open circuit voltage less than 0.556 V.

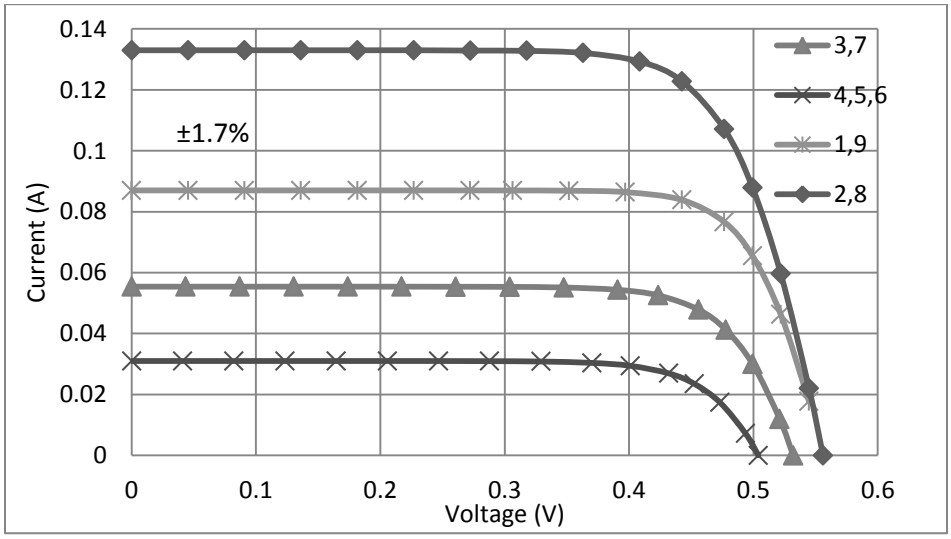

Figure 6.31: Photovoltaic characteristic curve for cells inside cavity receiver.

For columns 1 and 9, the case is slightly different. The short circuit current at the given open circuit voltage is lower than what would be expected. This indicates that one of the two cells connected in parallel in each column is dark. The cell acts as a diode, and draws current form the irradiated solar cell. The higher the intensity of radiation on the un-shaded cell, the

greater is the current drawn by the diode. This is due to the exponential shape of the I-V curve for a diode. So again, the presence of the dark cell in parallel actually hinders the power output in this case by providing a current sink. The irradiated cell would have a higher open circuit voltage without the parallel cell, and the corresponding short circuit current.

Once again, this indicates that the assumption that two cells in parallel would receive equal amounts of radiation is incorrect. A better solution is to determine the performance of each cell individually and then connect them in series or parallel as required to get a suitable output.

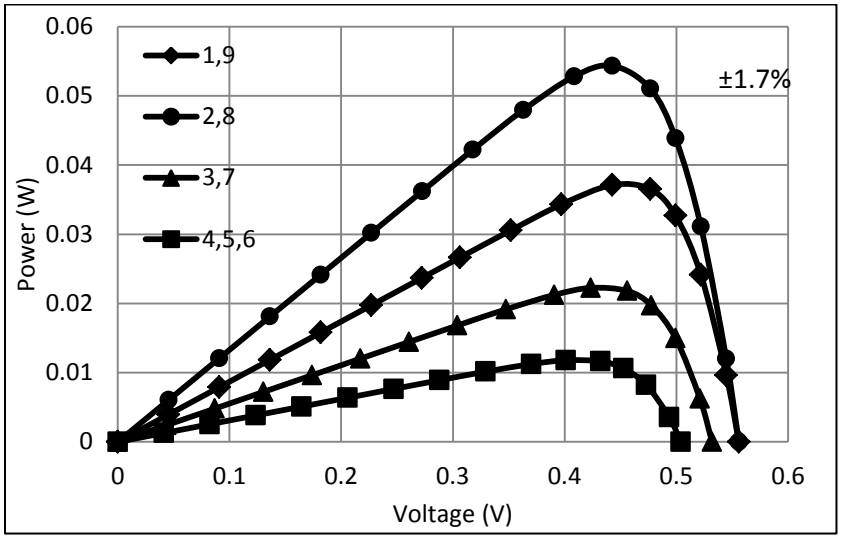

Figure 6.32: Power curve for the photovoltaic cells inside cavity receiver.

The output from the cells remains the same across all experiments, because the factors that influence PV power production remain constant. These include the light intensity, catalyst concentration, solution volume, and the sun inclination. In an actual system, the light intensity and the solar inclination are the factors that affect the PV power output most significantly. Also, the issue with uneven shading is accounted for by installing bypass diodes and blocking diodes to prevent dissipation of power, and system is integrated with a maximum power point tracker (MPPT) to draw the maximum power, and a convertor to obtain a constant, desired voltage. The

power curve of the cells is shown in Figure 6.32. A total power of 0.126 W may be obtained. The energy efficiency of the system increases from 0.08% to 1.00% with photovoltaic hybridization.

6.10 Performance Analysis of Large Scale System

In this section, the hybridized system that is proposed in section 5.1 is analyzed under various conditions and the amount of hydrogen produced is determined for a sample of archived data.

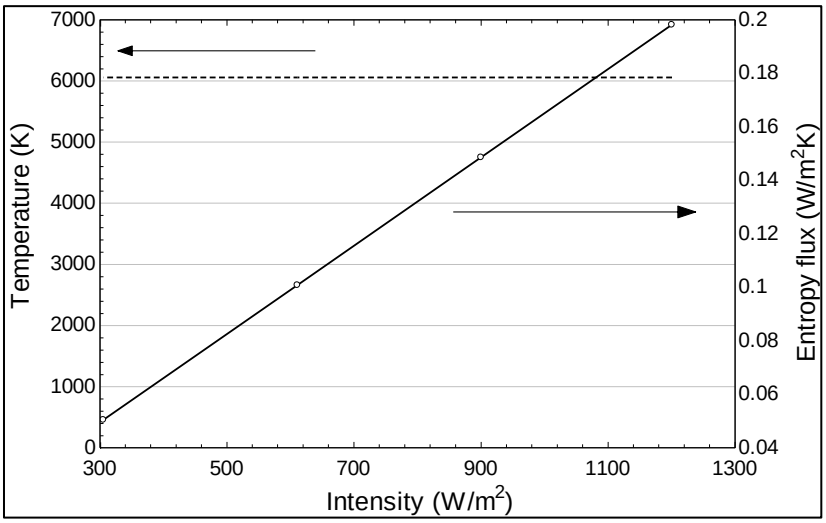

Figure 6.33: Effective radiation temperature and effective radiation entropy with respect to intensity.

The concept of effective photon temperature described by Chen et al. (2008) is used to evaluate the solar based hydrogen production system, by tracing the movement of energy through the system. The effective photon temperature is integrated over the full spectrum available in order to obtain the effective spectrum temperature, as described by Zamfirescu and Dincer (2013). This temperature defines the shape of the spectrum, but is independent of the magnitude of the solar radiation, as shown in the figure. A spectrum that has been filtered to remove the longer wavelength photons will have a higher effective temperature as compared to the full spectrum, regardless of the relative magnitudes of the two spectra. A better gage of the

quality of the radiation is the effective entropy flux of the spectrum, as defined in section 5.7.1. As noted from the plot of Figure 6.33, the entropy flux is proportional to the intensity of a spectrum whose shape is maintained.

The output form the system is dependent on the irradiation from the Sun, and the position of the sun with respect to the reflecting face of the heliostats. The field factor defined in section 5.7.1 accounts for the movement of the sun, and the various changes in the concentrated light that are caused by it. This factor is determined based on the exact details of the solar field. Here, a suitable value is selected based on a previous study conducted (Zamfirescu and Dincer, 2013).

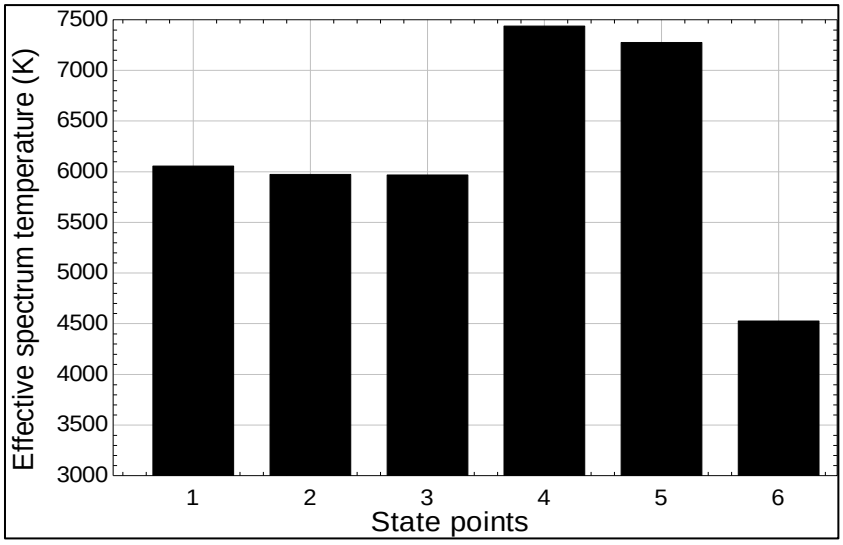

Figure 6.34: Effective radiation temperature at system states.

Figure 6.34 shows the effective temperature of the spectrum at every state in the system. The plot is understood by following the changes in the spectrum. The incoming solar radiation is reflected by the heliostats in the direction of the solar tower. The reflectance of the radiation from the heliostats is not perfect, but is determined by the material of the mirror. In this case, an aluminum mirror is used which has a reflectance plot as shown in Figure 6.35. Here, the reflectance is plotted on the left vertical axis, based on data available data (Palik, 1998).

The slight decrease in the temperature at state 2 is due to the relatively poor reflective properties at lower wavelengths, although the lowest point is still at 87%, hence the very slight decrease. The radiation is concentrated on to the diffuser, for which a high level of transmission is desired. Figure 6.35 shows the transmittance of a fused silica ground glass type diffuser, obtained from supplier (Thorlabs). The high quality of the diffuser allows the temperature to be maintained as the radiation is transmitted through and into the cavity receiver.

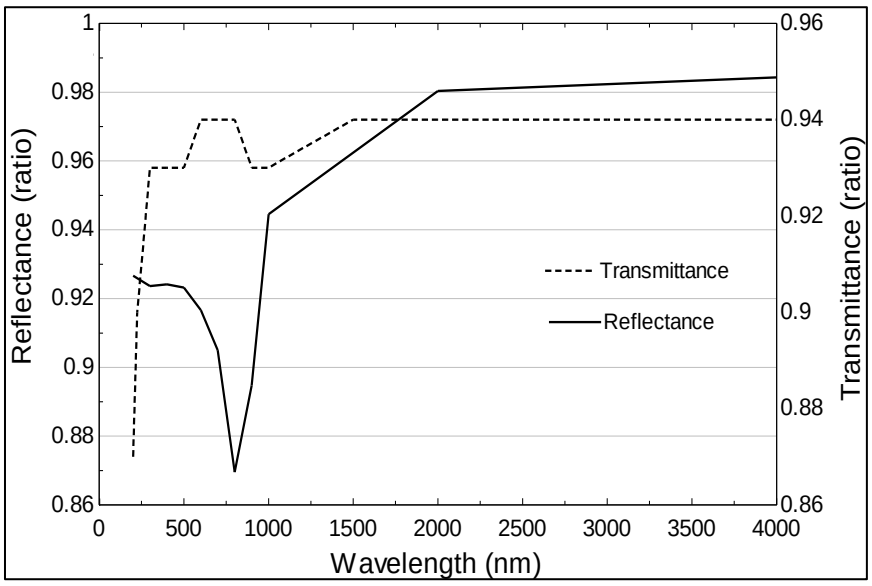

Figure 6.35: Heliostat reflectance and diffuser transmission curves.

Figure 6.36 shows the characteristics of the band pass coatings that are applied on to the photo-reactors, the PV modules and the thermal receivers inside the cavity receiver. The data is provided by ZR&C Coatings. The effective temperature of the radiation entering the photoreactors is 7400 K, due to the selective presence of high energy photons in the spectrum. The temperature at state 5, where the radiation enters the PV modules is slightly less. Due to only radiation higher than 700 nm being absorbed by the thermal receiver, a relatively low effective temperature is achieved at state 6. For the analysis, it is assumed that the radiation is absorbed sequentially; first by the photoreactors, then by the PV modules, and finally by the

thermal receiver. However, actually that is not the case, and the simultaneous absorbance of radiation by the three sub-systems may result in slightly different effective temperatures due to the interference in the wavelength of the band pass coatings.

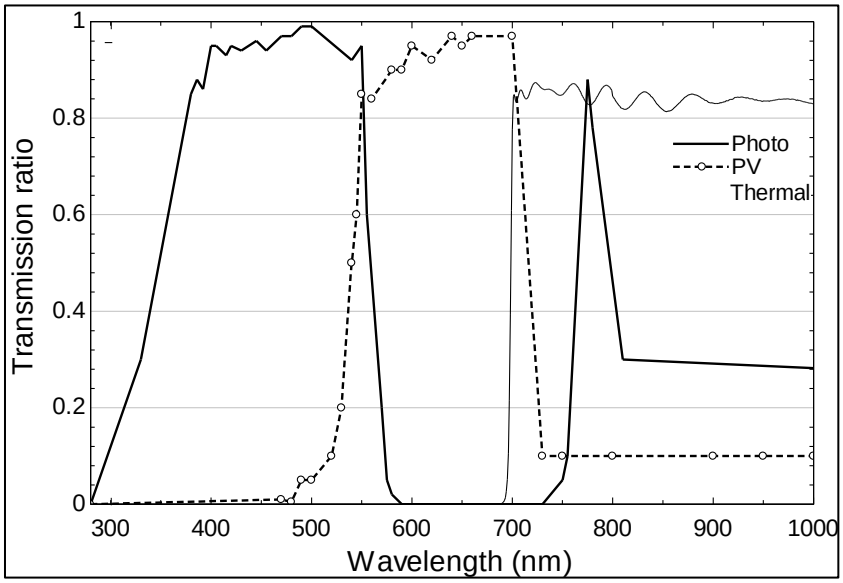

Figure 6.36: Band pass coatings for photoreactor, photovoltaics, and thermal receiver.

By knowing the intensity variation for a location, the daily path of the sun, the behaviour of specific sub-systems with respect to the input, and the design of the solar field, the performance of the system can be simulated for every hour of every day. This allows the calculation of the expected return on the investment made on such a system. Table 6.1 gives the selected set of parameters used for analysis. The sample values for effective heliostat area and the field factor are obtained from those determined in previous studies (Zamfirescu and Dincer, 2013).

Figure 6.37 shows the energy and exergy content of the solar radiation at each state in the system. A major loss occurs in the solar concentrator. Considering that the values shown are for a fairly high field factor, over the course of a day, a greater loss can be expected at this step as the field factor decreases. This shows the importance of designing heliostat fields that can

minimize the loss, by research into techniques such as arrangement algorithms for the heliostat or electronically controlled tracking. Notice the similar values for energy and exergy rate for the radiation entering the photoreactors (4) and PV modules (5), due to the high value of the effective temperatures for both. A large drop is observed from 3 to 4 because above the cut-off wavelength for the photoreactor coating is only a small portion of the solar spectrum. However, due to the arrangement of the system, the rejected energy is not lost, but utilized by the PV modules and the thermal receiver. The exergy of the radiation absorbed by the PV modules is significantly lower than that of the photoreactors because even though the effective temperature is high, it is offset by the low quantity of energy contained within that spectrum.

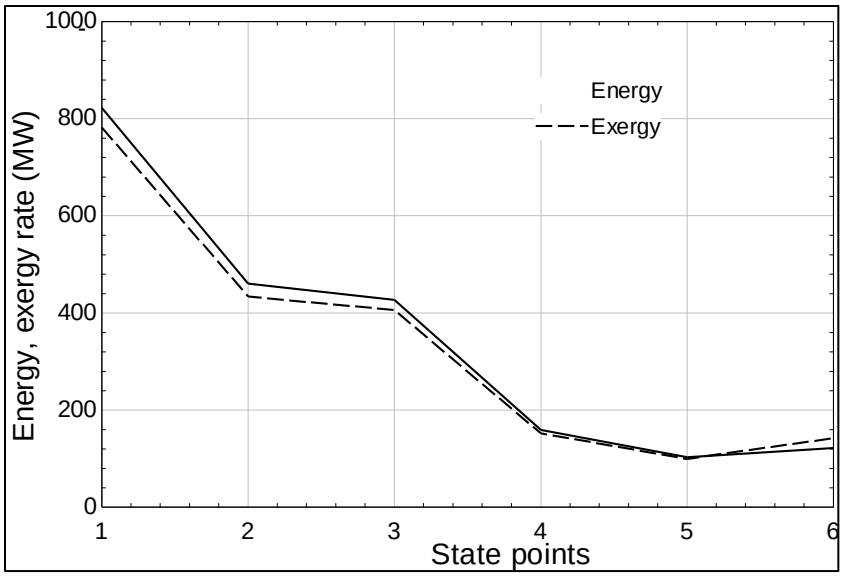

Figure 6.37: Energy and exergy transfer rate at each system state.

Figure 6.38 shows the effect of the field factor that is mentioned previously. A drop in the field factor may correspond to a situation where the angle of the sun is not close to perpendicular to the plane of the mirror, due to the passing of time, but the intensity of radiation remains the same. The degradation of the performance of the heliostat field can be observed. From a drop of close to 150 MW, the exergy loss associated with the heliostat field now is nearly 450 MW.

The value of the quantum efficiency for the photocatalytic process has been chosen based on results presented that show high activity of heterogeneous catalyst under visible light (Yan et al., 2009; Zamfirescu et al., 2013). Similarly, the efficiency for PV systems falls in the range of 10 – 40%, so a value is selected that falls within this range (Kribus and Mittelman, 2007).

Table 6.1: Parameters used for thermodynamic analyses.

Parameter	Symbol	Value	Reference
Stefan Boltzmann constant	$\sigma\ (W/m^2K^4)$	5.67 X 10^{-8}	(Cengel and Turner, 2001)
Emissivity of thermal receiver	ε	0.95	(Cengel and Turner, 2001)
Overall heat transfer coefficient of molten salt	$U\ (W/m^2K^4)$	4000	(Bohlmann, 1972)
Reflective field area	$A_{field}\ (m^2)$	913289	(Zamfirescu and Dincer, 2013)
Heat capacity of molten salt	$C_p(kJ/kg\ K)$	1560	(Bohlmann, 1972)
Quantum efficiency of photocatalytic process	ϕ_{cat} (%)	40	(Yan et al., 2009)
Energy efficiency of photocatalytic process	η_{PV} (%)	10-40	(Kribus and Mittelman, 2007)

The thermal receiver area for effective heat transfer depends on the log mean temperature difference that is selected for the thermal receiver and the heat collection fluid. Even though the thermal receiver in this case is not a conventional heat exchanger, but a pipe network within the cavity receiver that carries the heat storage fluid, the LMTD method may be used to arrive at a suitable estimate for the receiver surface area. A high LMTD allows for a smaller receiver area, as the convection heat transfer within the thermal receiver to the heat storage fluid is enhanced due to the greater temperature gradient. The plot in Figure 6.38 is for the maximum value of radiation received by the thermal receiver, at a field factor value of 1, ensuring that the area is selected for the upper limiting case. Conversely, a negative aspect of very high LMTD is a greater exergy destruction within the exchanger. Based on the plot, a suitable value is 1000 m^2.

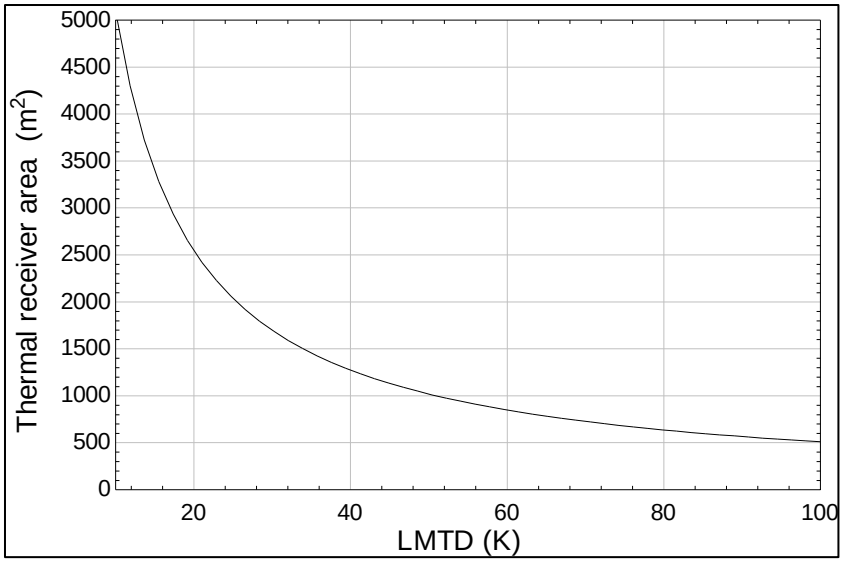

Figure 6.38: Variation of surface area required for effective heat transfer with respect to selected LMTD value.

The following assumptions are made for the thermal receiver: (a) The hot storage temperature is equal to the outlet stream from the thermal receiver, and the cold storage temperature is equal to the inlet stream temperature. (b) Only radiation heat loss occurs from the thermal receiver, and escapes through the cavity aperture. (c) Hot storage and cold storage are perfectly insulated.

For a given value of incident radiation on the thermal receiver, a relation between mass flow rate of the storage fluid, or the heat transfer fluid (HTF), through the thermal receiver and the exit temperature of HTF from the thermal receiver can be established. The cold temperature of the HTF is set at 450 K, which is around 30 K more than its freezing temperature. The plot shown in Figure 6.39 is for the case when the field factor is 1. A high temperature is beneficial from the point of view of the heat engine, but the greater temperature comes with a cost of higher radiation heat loss from the thermal receiver, and increases the sensitivity of the system, as it is likely to result in a higher cavity receiver temperature. The variation of efficiencies for the thermal receiver is shown in Figure 6.39. As the temperature of the HTF at receiver exit is

increased, it results in a decrease in the energy efficiency, due to the greater proportion of radiation heat loss. However, the exergy efficiency actually increases, as the radiation heat loss is offset by the higher quality of energy transferred to the HTF. The exergy efficiency peaks at around 1100 K. Based on the plot, a suitable temperature for the HTF at state 16 seems to be in the range of 800 – 1000 K.

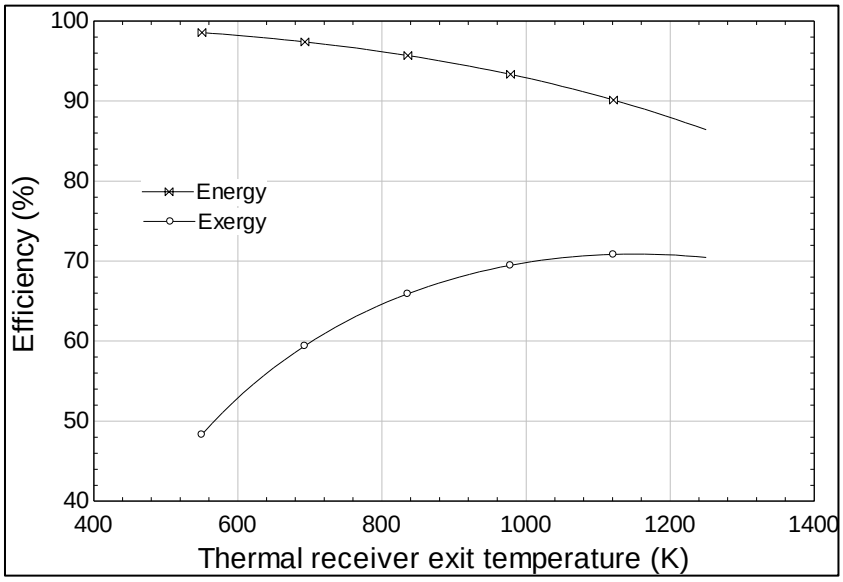

Figure 6.39: Variation of thermal receiver efficiencies with variation in HTF exit temperature.

Consideration must also be given to the fact that in order to maintain the temperature, the mass flow rate of the HTF needs adjustment as the field factor value varies over the course of a day. From a practical stand point, the variation in the flow rate must not be too excessive. The plot of Figure 6.40 shows the variation required for the mass flow rate of the HTF at different temperatures. At lower temperatures, a greater variation in the flow rate is required for the maintenance of the exit temperature. However, the variation does not appear excessive in any case.

So far the system state parameters have been determined using an arbitrary value of the field factor, or at most, the relationship between the field factor and certain quantities. However,

in order to better comprehend the design requirements of the heat engine, the field factor values for a certain day of the year are used, as shown in Figure 6.41. These field factor values are for a particular summer day of August, and for a particular day of February, in order to provide an idea of the seasonal change. It is adapted from work done by Zamfirescu and Dincer (2013), based on the System Advisor Model (SAM) provided by the National Renewable Energy Laboratory (NREL).

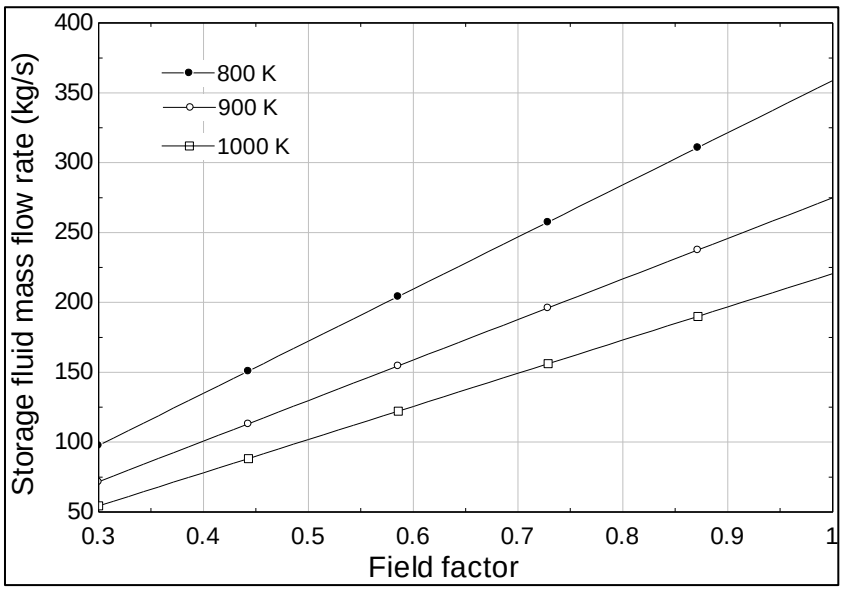

Figure 6.40: Variation of HTF flow rate with field factor for exit temperature maintenance.

Different regimes may be selected for the operation of the heat engine. However, intermittency of turbine operation is undesirable in general. In this case, the attempt is made to keep the heat engine operating constantly for 24 hours. For this, the heat engine should be sized so as to produce at least three times less power than is stored within the hot storage for the 24 hour period. Because the actual insolation received during a day in the summer may also be less than that shown in the figure for some days, or more for some days, due to weather changes, in this case, the assumption is made that at if the heat engine is sized at a quarter of the value that is stored in the hot storage on the particular summer day shown in the figure, then the excess

energy should be sufficient to overcome any fluctuations in the solar radiation that is not due to extraordinary circumstances.

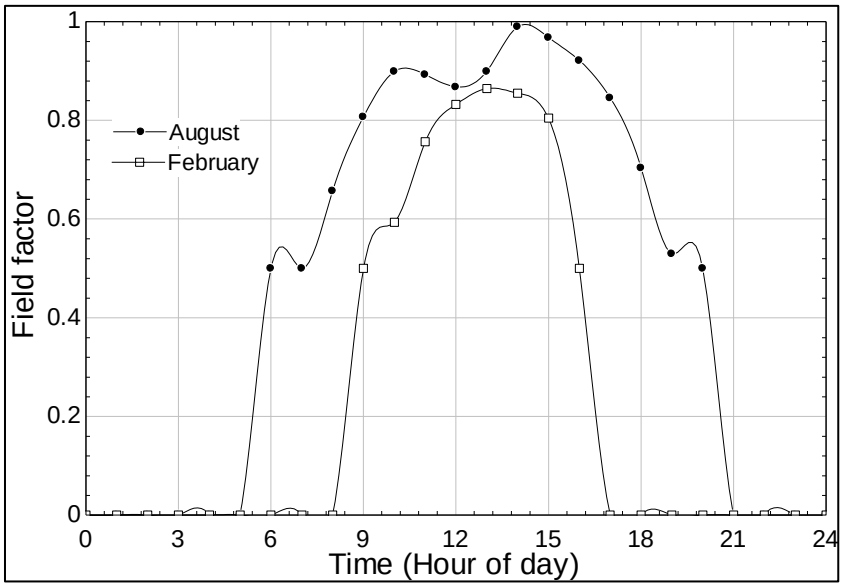

Figure 6.41: Variation of field factor for two days of the year based on archived data (Adapted from Zamfirescu and Dincer (2013)).

Based on the criteria mentioned, the hot storage may exchange heat with the heat engine working fluid at a maximum rate of 68 MW. It is assumed here that the temperature of the hot storage is equal to the temperature of the HTF as it leaves the thermal receiver, and the temperature of the cold storage is equal to the temperature of the HTF as it enters the thermal receiver. Furthermore, the assumption is made the HTF from the hot storage entering the heat engine heat exchanger is at the temperature of the hot storage, and that entering the cold storage is at a temperature of the cold storage. The size of the storage is sufficiently large with respect to the energy interactions that occur so as not to change its properties. Also, adiabatic storage is assumed.

When setting the inlet pressure of the turbine, quality of the vapour mixture achieved at the turbine exit is of importance. Usually, having a percentage of liquid greater than 20% in the

turbine is not recommended due to the adverse effects that causes on the turbine blades. The variation of the quality of mixture is shown against the chosen turbine inlet pressure in Figure 6.42. Based on this, the pressure is chosen as 12.5 MPa.

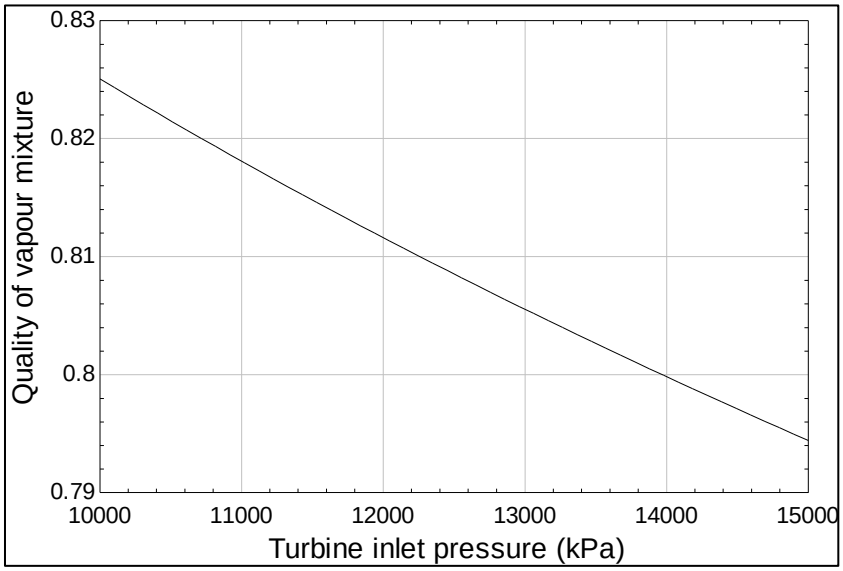

Figure 6.42: Variation of working fluid quality at turbine exit with respec to turbine inlet pressure.

Figure 6.43 shows the variation of the exergy efficiencies for the thermal receiver and for the heat engine as related to the variation of the environmental temperature. As the environment temperature increases, the exergy efficiency of the thermal receiver decreases. This is because the input for the thermal receiver, which is the solar radiation, has such a high effective temperature that the variation in the environmental temperature hardly makes a difference to the exergy content of the incoming radiation. The outputs from the thermal receiver, however, experience a significant decrease in their exergy content as the environment temperature increases, hence the observance of the decrease of efficiency.

For the heat engine, increasing the environment temperature results in an increase in the efficiency because the outputs form the heat engine are in the form of work, for which

environmental variation does not result in any change of exergy content. The input, however, is in the form of heat, which undergoes a decrease in the exergy content as the environmental temperature is increased.

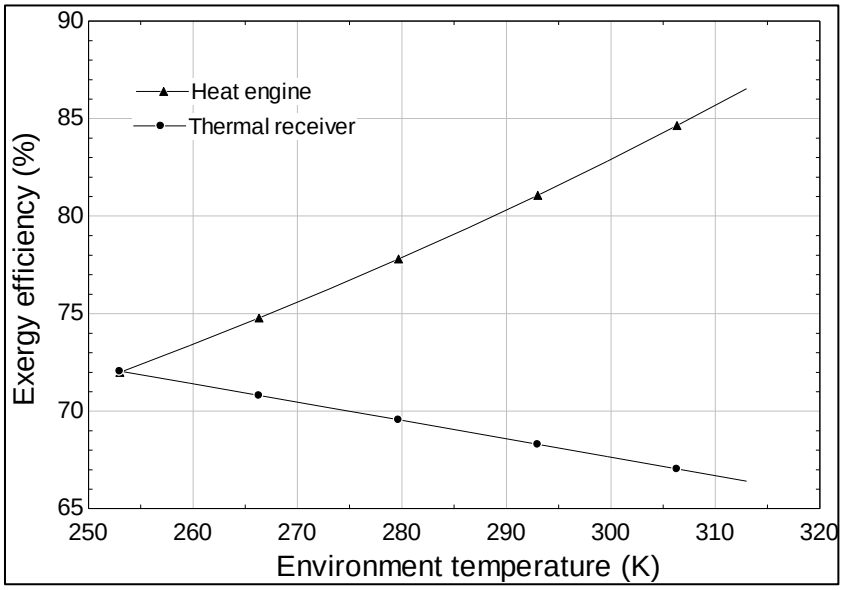

Figure 6.43: Variation of thermal receiver and heat engine exergy efficiency with change in reference state temperature.

Figure 6.44 shows the production of hydrogen for the summer day of August, for each energy conversion process of the system. The photocatalytic and photovoltaic hydrogen production is dependent on the energy input rate into the system, and is affected by the compounded field factor. This is because the processes are capable of intermittent operation, and are designed in such a way. The hydrogen produced due to the heat engine, however, increases at a constant rate due to the way the system is designed, which allows constant operation of the turbine. The total production is 52 000 kg.

The variation of the system efficiencies is shown in Figure 6.45. The outputs from the system are taken as the energy and exergy contents of the amounts of hydrogen produced by the photoreactor and the photovoltaic-electrolyzer system, and the content of the heat that is stored

in the hot storage. The inputs are the energy and exergy at state 1, which is the solar radiation harnessed by the mirrors, for the corresponding efficiencies. The major variation in the efficiency is brought about by the efficiency of the hot storage. As the field factor is increased, and consequently the inputs are increased, in order to keep the temperature of the fluid entering the hot storage constant, the mass flow rate of the increases logarithmically, resulting in an increase in efficiency initially, which tapers off towards higher values of the field factor.

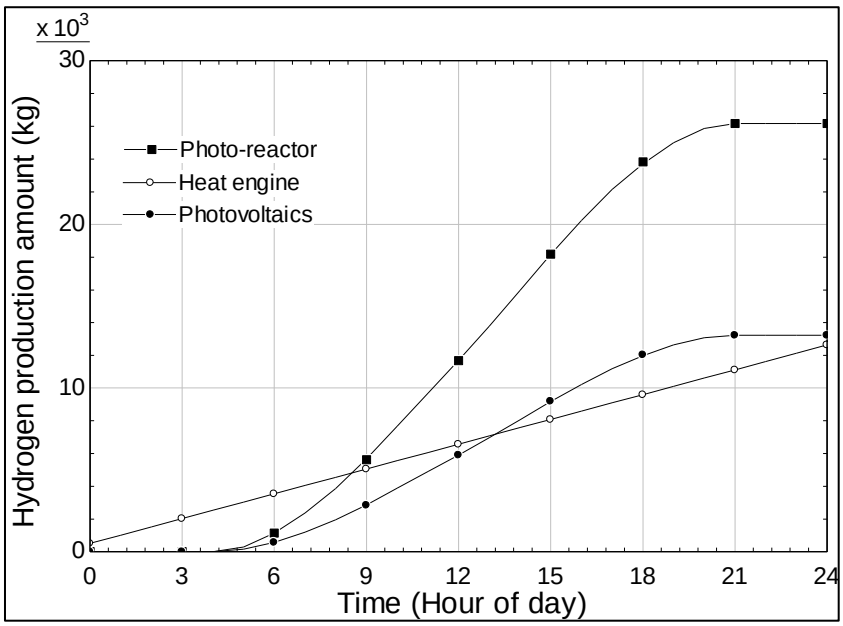

Figure 6.44: Progression of hydrogen production for a day of August.

In Figure 6.46, the variation of the system efficiencies is shown for a summer day and a winter day, during their respective operation hours. The efficiencies levels reached during winters are comparable to those in the summer, as good quality sunlight may be available in the winter. However, the decrease in the daylight hours available will have a significant effect in the winter.

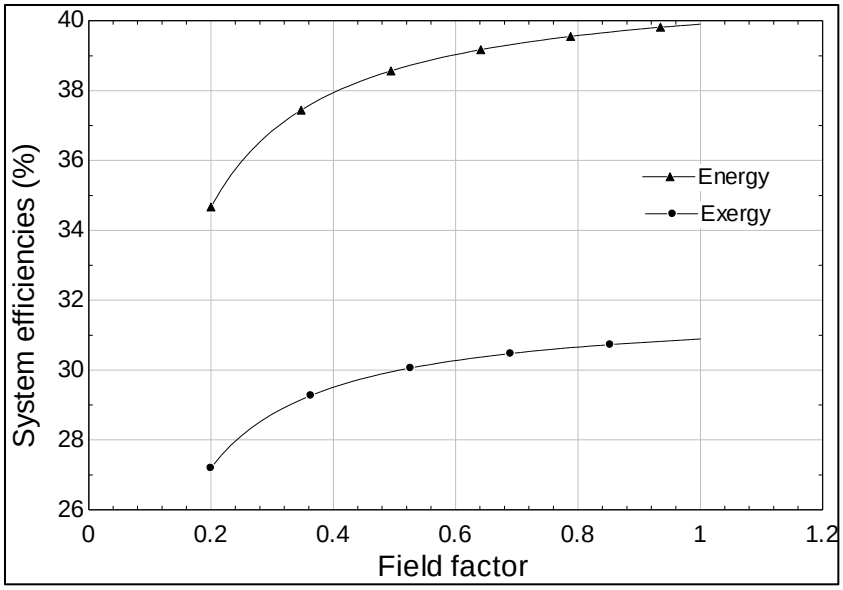

Figure 6.45: Variation of system energy and exergy efficiency with field factor variation.

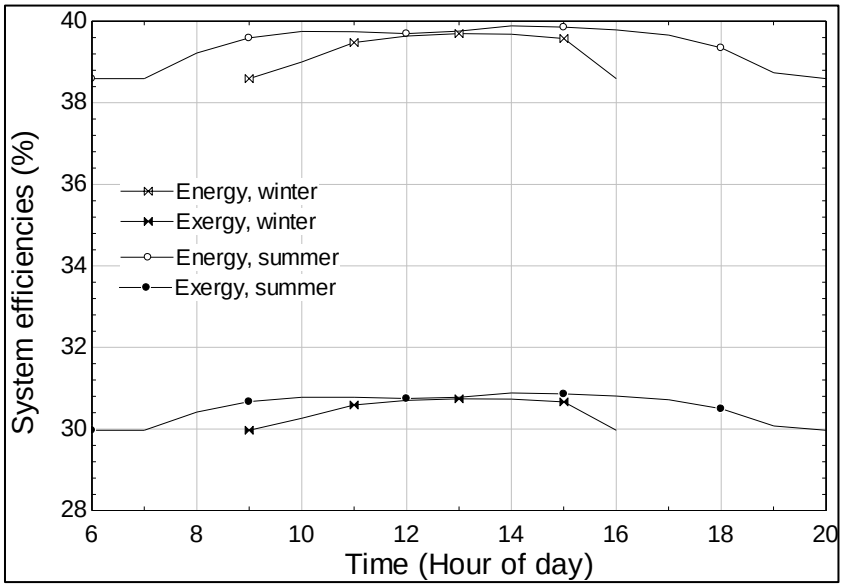

Figure 6.46: Progression of system efficiencies for two archived days of the year.

Chapter 7: Conclusions and Recommendations

In this thesis, the mechanism for photocatalytic hydrogen production water was investigated experimentally, and the behaviour of the process with respect to certain variables studied. A rate model was developed that may later be used in conjunction with other photocatalytic models. A new photoreactor system was proposed, as part of a hybridized hydrogen production system that would produce hydrogen by reduction of sulfurous waste, including hydrogen sulfide. Here, the pertinent points of the thesis are summarized, and a recommendation made on the paths that should be taken in the future with regards to research based on the work presented here.

7.1 Conclusions

This study presents a new design for a photocatalytic hydrogen production process. A solar tower concept is proposed, where the photocatalytic reactor is housed inside a cavity receiver, and unused photons are harvested by photovoltaic cells for electric power production, which may then be used to power an electrolyser for further hydrogen production. A fully functioning lab scale system of the design is built, and run as a proof of concept. A theoretical model is developed for the photocatalytic process. Thermodynamic analyses is performed for a proposed large scale system that combines a photocatalytic process, photovoltaic process, and a heat engine for the production of hydrogen within a solar tower setting. The main findings of the study are summarized as follows:

- The quantum efficiency of the photocatalytic process increases from 0.94% at atmospheric pressure and temperature to 1.92% at an absolute pressure of 21 kPa and a temperature of 40°C. The diffusion of hydrogen bubbles from the liquid to the gas phase is facilitated under

vacuum, while the high temperature increases the frequency of collision of chemical species. Both of these factors enhance the reaction rate

- A steady rate of hydrogen production may be achieved by implementation of continuous flow operation. For a process occurring in a 0.3 M electrolyte, the critical flow rate is 50 ml/h, beyond which the reaction rate does not increase justifiably.
- Hybridization of the system with photovoltaics increases the energy efficiency of the system from 0.17% to 2.15% and the exergy efficiency from 0.15% to 2.25%
- For the large scale system, the energy efficiency varies from 34% to 40% and the exergy efficiency varies from 27% to 31% for changing solar conditions throughout the day.
- For a chosen day of August, the total hydrogen produced by the system is 52 tonne. The photocatalytic process and photovoltaic process both operate intermittently according to the solar radiation. The heat engine is sized so as to operate continuously for 24 hours, through utilization of a thermal energy storage system.

7.2 Recommendations

In this section, certain points of interest that are felt to be pertinent towards future research in the area of the present study are presented as follows:

- Combination of a single or multiple electrolyser units to the photovoltaic cells provides an interesting end use of the power produced from the photovoltaic cells, and presents a more rounded and focussed hydrogen production system.
- Utilization of the heat loss from the reactor has the potential to significantly enhance the system efficiencies. For the lab scale model, it is likely to have an effect on the energy efficiency but not on the exergy efficiency. However, with greater concentration of light than

that achieved here, in a modified lab scale system or an actual large scale system, the heat may be at a high enough temperature to allow for power production via a heat engine, significantly improving both the energy and the exergy efficiencies, as shown in the large scale system. The potential of this should be investigated for the experimental system.

- There is a lack of comprehensive models that may predict the process outcome across different process parameters. Models need to be developed that incorporate temperature, pressure, concentration, and intensity variations, among other parameters, especially for the photocatalytic process, to allow for a more accurate analysis of conceptual processes.

References

Abbott, D. (2010). Keeping the energy debate clean: How do we supply the world's energy needs? *Proceedings of the IEEE, 98*(1), 42-66. doi: 10.1109/JPROC.2009.2035162

Albini, A., & Fagnoni, M. (2004). Green chemistry and photochemistry were born at the same time. *Green Chemistry, 6*(1), 1-6. doi: 10.1039/b309592d

Alstrum-Acevedo, J., Brennaman, M. K., & Meyer, T. J. (2005). Chemical approaches to artificial photosynthesis. 2. *Inorganic Chemistry, 44*(20), 6802-6827. doi: 10.1021/ic050904r

Andrew Frame, F., Carroll, E. C., Larsen, D. S., Sarahan, M., Browning, N. D., & Osterloh, F. E. (2008). First demonstration of CdSe as a photocatalyst for hydrogen evolution from water under UV and visible light. *Chemical Communications,* (19), 2206-2208. doi: 10.1039/B718796C

Balat, M. (2008). Possible methods for hydrogen production. *Energy Sources, Part A: Recovery, Utilization, and Environmental Effects, 31*(1), 39-50. doi: 10.1080/15567030701468068

Baniasadi, E. (2013). *Development of new hybrid photochemical/electrocatalytic water splitting reactor for hydrogen production: Design, analysis, and experiments.* University of ontario institute of technology).

Bao, N., Shen, L., Takata, T., & Domen, K. (2007). Self-templated synthesis of nanoporous CdS nanostructures for highly efficient photocatalytic hydrogen production under visible light. *Chemistry of Materials, 20*(1), 110-117. doi: 10.1021/cm7029344

Barber, J. (2009). Photosynthetic energy conversion: Natural and artificial. *Chemical Society Reviews, 38*(1), 185-196. doi: 10.1039/B802262N

Barnett, A., Kirkpatrick, D., Honsberg, C., Moore, D., Wanlass, M., Emery, K., . . . Salzman, D. (2009). *Very high efficiency solar cell modules* John Wiley & Sons, Ltd. doi: 10.1002/pip.852

Benniston, A. C., & Harriman, A. (2008). Artificial photosynthesis. *Materials Today, 11*(12), 26-34. doi: 10.1016/S1369-7021(08)70250-5

Bockris, J. O. M. (2013). The hydrogen economy: Its history. *International Journal of Hydrogen Energy, 38*(6), 2579-2588. doi: 10.1016/j.ijhydene.2012.12.026

Boden, T. A., Marland, G., & Andres, R. J. (2010). *Global, regional, and national fossil-fuel CO2 Emissions*. CarbonDioxide Information Analsysis Cnetre, Oak Ridge, Tennesee, USA: U.S. Department of Energy. doi: 10.3334/CDIAC/00001_V2010

Buehler, N., Meier, K., & Reber, J. F. (1984). Photochemical hydrogen production with cadmium sulfide suspensions. *The Journal of Physical Chemistry, 88*(15), 3261-3268. doi: 10.1021/j150659a025

Cetinkaya, E., Dincer, I., & Naterer, G. F. (2012). Life cycle assessment of various hydrogen production methods. *International Journal of Hydrogen Energy, 37*(3), 2071-2080. doi: 10.1016/j.ijhydene.2011.10.064

Chen, X., Shen, S., Guo, L., & Mao, S. S. (2010). Semiconductor-based photocatalytic hydrogen generation. *Chemical Reviews, 110*(11), 6503-6570. doi: 10.1021/cr1001645

Chen, Z., Mo, S., & Hu, P. (2008). Recent progress in thermodynamics of radiation -- exergy of radiation, effective temperature of photon and entropy constant of photon. *Science in China Series E: Technological Sciences, 51*(8), 1096-1109. doi: 10.1007/s11431-008-0158-x

Chow, J., Kopp, R. J., & Portney, P. R. (2003). Energy resources and global development. *Science, 302*(5650), 1528-31. Retrieved from http://search.proquest.com.uproxy.library.dc-uoit.ca/docview/213585154?accountid=14694

Ciamician, G. (1912). The photochemistry of the future. *Science, 36*(926), 385-394. Retrieved from http://www.jstor.org.uproxy.library.dc-uoit.ca/stable/1637055

Cooke, A. J., & Rowe, R. K. (1999). Extension of porosity and surface area models for uniform porous media. *Journal of Environmental Engineering, 125*(2), 126. Retrieved from http://search.ebscohost.com/login.aspx?direct=true&db=aph&AN=1558731&scope=site

Coventry, J. S. (2005). Performance of a concentrating photovoltaic/thermal solar collector. *Solar Energy, 78*(2), 211-222. doi: 10.1016/j.solener.2004.03.014

Crabtree, G. W., & Lewis, N. S. (2007). Solar energy conversion. *Physics Today, 60*(3), 37-42. Retrieved from http://dx.doi.org/10.1063/1.2718755

del Valle, F., Ishikawa, A., Domen, K., Villoria de, l. M., Sanchez-Sanchez, M. C., Gonzalez, I. D., . . . Navarro, R. M. (2009). Influence of Zn concentration in the activity of $Cd_{1-x}Zn_xS$ solid solutions for water splitting under visible light. *Catalysis Today; International Symposium on Catalysis for Clean Energy and Sustainable Chemistry, on Occasion of the 60th Birthday of Prof.Jose L.G.Fierro, 143*(1), 51-56. doi: http://dx.doi.org/10.1016/j.cattod.2008.09.024

Dincer, I., & Rosen, M. (2012). *Exergy: Energy, environment and sustainable development* Newnes.

Dincer, I., & Zamfirescu, C. (2012). Sustainable hydrogen production options and the role of IAHE. *International Journal of Hydrogen Energy, 37*(21), 16266-16286. doi: 10.1016/j.ijhydene.2012.02.133

Duan, L., Xu, Y., Zhang, P., Wang, M., & Sun, L. (2010). Visible light-driven water oxidation by a molecular ruthenium catalyst in homogeneous system. *Inorganic Chemistry, 49*(1), 209-215. doi: 10.1021/ic9017486

Elvington, M., Brown, J., Arachchige, S. M., & Brewer, K. J. (2007). Photocatalytic hydrogen production from water employing a Ru, Rh, Ru molecular device for photoinitiated electron collection. *Journal of the American Chemical Society, 129*(35), 10644-10645. doi: 10.1021/ja073123t

Esswein, A. J., Veige, A. S., & Nocera, D. G. (2005). A photocycle for hydrogen production from two-electron mixed-valence complexes. *Journal of the American Chemical Society, 127*(47), 16641-16651. doi: 10.1021/ja054371x

Ferreira, K. N., Iverson, T. M., Maghlaoui, K., Barber, J., & Iwata, S. (2004). Architecture of the photosynthetic oxygen-evolving center. *Science, 303*(5665, Drug Discovery), 1831-1838. Retrieved from http://www.jstor.org.uproxy.library.dc-uoit.ca/stable/3836509

Gía, L. M., Oroz, R., Ursúa, A., Sanchis, P., & Diéguez, P. M. (2007). Renewable hydrogen production: Performance of an alkaline water electrolyzer working under emulated wind conditions. *Energy & Fuels, 21*(3), 1699-1706. doi: 10.1021/ef060491u

Goldemberg, J. (2006). The promise of clean energy. *Energy Policy, 34*(15), 2185-2190. Retrieved from http://search.proquest.com.uproxy.library.dc-uoit.ca/docview/205315946?accountid=14694

Golder, A. S. (2007). *Photovoltaic generator modelling for large scale distribution system studies.* (Master of Science, Drexel University).

Green, M. A. (2001). Limiting photovoltaic monochromatic light conversion efficiency. *Progress in Photovoltaics: Research and Applications, 9*(4), 257-261. doi: 10.1002/pip.375

Green, M. A. (2001). Third generation photovoltaics: Ultra-high conversion efficiency at low cost. *Progress in Photovoltaics: Research and Applications, 9*(2), 123-135. doi: 10.1002/pip.360

Green, M. A., Emery, K., Hishikawa, Y., & Warta, W. (2010). Solar cell efficiency tables (version 35). *Progress in Photovoltaics: Research and Applications, 18*(2), 144-150. doi: 10.1002/pip.974

Heyduk, A. F., & Nocera, D. G. (2001). Hydrogen produced from hydrohalic acid solutions by a two-electron mixed-valence photocatalyst. *Science, 293*(5535), 1639-1641. Retrieved from http://www.jstor.org.uproxy.library.dc-uoit.ca/stable/3084619

Holladay, J. D., Hu, J., King, D. L., & Wang, Y. (2009). An overview of hydrogen production technologies. *Catalysis Today, 139*(4), 244-260. doi: 10.1016/j.cattod.2008.08.039

Hung, T. C., Shai, T. Y., & Wang, S. K. (1997). A review of organic rankine cycles (ORCs) for the recovery of low-grade waste heat. *Energy, 22*(7), 661-667. doi: 10.1016/S0360-5442(96)00165-X

Jäger-Waldau, A. (2012). Appendix D - the photovoltaic market. *Practical handbook of photovoltaics (second edition)* (pp. 1137-1152). Boston: Academic Press. doi: 10.1016/B978-0-12-385934-1.00049-0

Jing, D., Zhang, Y., & Guo, L. (2005). Study on the synthesis of Ni doped mesoporous TiO_2 and its photocatalytic activity for hydrogen evolution in aqueous methanol solution. *Chemical Physics Letters, 415*(1-3), 74-78. doi: 10.1016/j.cplett.2005.08.080

Jing, D., Guo, L., Zhao, L., Zhang, X., Liu, H., Li, M., . . . Guo, P. (2010). Efficient solar hydrogen production by photocatalytic water splitting: From fundamental study to pilot demonstration. *International Journal of Hydrogen Energy; ISMF-09 International Symposium on Multiphase Flow, Heat Mass Transfer and Energy Conversion, 35*(13), 7087-7097. doi: http://dx.doi.org/10.1016/j.ijhydene.2010.01.030

Jordan, P., Fromme, P., Horst Tobias Witt, Klukas, O., & et al. (2001). Three-dimensional structure of cyanobacterial photosystem I at 2.5 angstrom resolution. *Nature, 411*(6840), 909-17. doi: http://dx.doi.org.uproxy.library.dc-uoit.ca/10.1038/35082000

Joshi, A. S., Dincer, I., & Reddy, B. V. (2009). Thermodynamic assessment of photovoltaic systems. *Solar Energy, 83*(8), 1139-1149. doi: 10.1016/j.solener.2009.01.011

Joshi, A. S., Dincer, I., & Reddy, B. V. (2010). Exergetic assessment of solar hydrogen production methods. *International Journal of Hydrogen Energy, 35*(10), 4901-4908. doi: 10.1016/j.ijhydene.2009.09.067

Kakuta, N., Park, K. H., Finlayson, M. F., Ueno, A., Bard, A. J., Campion, A., . . . White, J. M. (1985). Photoassisted hydrogen production using visible light and coprecipitated ZnS·CdS without a noble metal. *The Journal of Physical Chemistry, 89*(5), 732-734. doi: 10.1021/j100251a002

Kato, H., Asakura, K., & Kudo, A.Highly efficient water splitting into H_2 and O_2 over lanthanum-doped $NaTaO_3$ photocatalysts with high crystallinity and surface nanostructure. *Journal of the American Chemical Society*, (10), 3082. doi: 10.1021/ja027751g

Kobayakawa, K., Teranishi, A., Tsurumaki, T., Sato, Y., & Fujishima, A. (1992). Photocatalytic activity of $CuInS_2$ and $CuIn_5S_8$. *Electrochimica Acta, 37*(3), 465-467. Retrieved from http://resolver.scholarsportal.info/resolve/00134686/v37i0003/465_paoc2ac5s8

Koca, A., & Sahin, M. (2002). Photocatalytic hydrogen production by direct sun light from sulfide/sulfite solution. *International Journal of Hydrogen Energy, 27*(4), 363-367. doi: 10.1016/S0360-3199(01)00133-1

Kribus, A., Doron, P., Rubin, R., Karni, J., Reuven, R., Duchan, S., & Taragan, E. (1999). A multistage solar receiver:: The route to high temperature. *Solar Energy, 67*(1), 3-11. doi: http://dx.doi.org/10.1016/S0038-092X(00)00056-6

Kribus, A., & Mittelman, G. (2007). Potential of polygeneration with solar thermal and photovoltaic systems. *Journal of Solar Energy Engineering, 130*(1), 011001-011001. Retrieved from http://dx.doi.org/10.1115/1.2804618

Kudo, A., & Miseki, Y. (2009). *Heterogeneous photocatalyst materials for water splitting* The Royal Society of Chemistry. doi: 10.1039/B800489G

Kudo, A., & Sekizawa, M. (1999). Photocatalytic H_2 evolution under visible light irradiation on $Zn_{1-x}Cu_xS$ solid solution. *Catalysis Letters, 58*(4), 241-243. doi: 10.1023/A:1019067025917

Kudo, A., & Sekizawa, M. (2000). Photocatalytic H evolution under visible light irradiation on Ni-doped ZnS photocatalyst. *Chemical Communications, 0*(15), 1371-1372. doi: 10.1039/B003297M

Large scale photovoltaic power plants ranking 1-50. (2013). Retrieved 04/2012, 2013, from http://www.pvresources.com/PVPowerPlants/Top50.aspx

Lee, Y., Terashima, H., Shimodaira, Y., Teramura, K., Hara, M., Kobayashi, H., . . . Yashima, M. (2007). Zinc germanium oxynitride as a photocatalyst for overall water splitting under visible light. *The Journal of Physical Chemistry C, 111*(2), 1042-1048. doi: 10.1021/jp0656532

Limburg, J., Vrettos, J. S., Liable-Sands, L. M., Rheingold, A. L., Crabtree, R. H., & Brudvig, G. W. (1999). A functional model for O-O bond formation by the O_2-evolving complex in photosystem II. *Science, 283*(5407), 1524-1527. Retrieved from http://www.jstor.org.uproxy.library.dc-uoit.ca/stable/2896915

Liu, M., You, W., Lei, Z., Zhou, G., Yang, J., Wu, G., . . . - Li, C.Water reduction and oxidation on pt-Ru/$Y_2Ta_2O_5N_2$ catalyst under visible light irradiation. *Chemical Communications,* (19), 2192. doi: 10.1039/B407892F

Maeda, K., & Domen, K. (2010). Photocatalytic water splitting: Recent progress and future challenges. *The Journal of Physical Chemistry Letters,* (18), 2655. doi: 10.1021/jz1007966

Maeda, K., Teramura, K., & Domen, K. (2008). Effect of post-calcination on photocatalytic activity of $(Ga_{1-x}Zn_x)(N_{1-x}O_x)$ solid solution for overall water splitting under visible light. *Journal of Catalysis, 254*(2), 198-204. doi: 10.1016/j.jcat.2007.12.009

Maeda, K., Abe, R., & Domen, K. (2011). Role and function of ruthenium species as promoters with TaON-based photocatalysts for oxygen evolution in two-step water splitting under visible light. *The Journal of Physical Chemistry C, 115*(7), 3057-3064. doi: 10.1021/jp110025x

Maeda, K., Takata, T., Hara, M., Saito, N., Inoue, Y., Kobayashi, H., & Domen, K. (2005). GaN:ZnO solid solution as a photocatalyst for visible-light-driven overall water splitting. *Journal of the American Chemical Society, 127*(23), 8286-8287. doi: 10.1021/ja0518777

Malato, S., Blanco, J., Richter, C., Curcó, D., & Giménez, J. (1997). Low-concentrating CPC collectors for photocatalytic water detoxification: Comparison with a medium concentrating solar collector. *Water Science and Technology, 35*(4), 157-164. Retrieved from http://resolver.scholarsportal.info/resolve/02731223/v35i0004/157_lccfpwwamcsc

Matsumura, M., Saho, Y., & Tsubomura, H. (1983). Photocatalytic hydrogen production from solutions of sulfite using platinized cadmium sulfide powder. *The Journal of Physical Chemistry, 87*(20), 3807-3808. doi: 10.1021/j100243a005

Mel, H. C., Hugus, Z. Z., & Latimer, W. M. (1956). The thermodynamics of thiosulfate Ion1. *Journal of the American Chemical Society, 78*(9), 1822-1827. doi: 10.1021/ja01590a014

Nocera, D. G. (2006). On the future of global energy. *Daedalus, 135*(4), 112-115. Retrieved from http://search.proquest.com.uproxy.library.dc-uoit.ca/docview/210572069?accountid=14694

Nozik, A. J., & Miller, J. (2010). Introduction to solar photon conversion. *Chemical Reviews, 110*(11), 6443-6445. doi: 10.1021/cr1003419

Olah, G. A. (2005). Beyond oil and gas: The methanol economy. *Angewandte Chemie International Edition, 44*(18), 2636-2639. doi: 10.1002/anie.200462121

Osterloh, F. E. (2007). Inorganic materials as catalysts for photochemical splitting of water. *Chemistry of Materials, 20*(1), 35-54. doi: 10.1021/cm7024203

Pagliaro, M., Konstandopoulos, A. G., Ciriminna, R., & Palmisano, G. (2010). Solar hydrogen: Fuel of the near future. *Energy & Environmental Science, 3*(3), 279-287. doi: 10.1039/B923793N

Preethi, V., & Kanmani, S. (2013). Photocatalytic hydrogen production. *Materials Science in Semiconductor Processing, 16*(3), 561-575. doi: 10.1016/j.mssp.2013.02.001

Rabl, A. (1976). Comparison of solar concentrators. *Solar Energy, 18*(2), 93-111. doi: 10.1016/0038-092X(76)90043-8

Rauschenbach, H. S. (1971). Electrical output of shadowed solar arrays. *Electron Devices, IEEE Transactions on, 18*(8), 483-490. doi: 10.1109/T-ED.1971.17231

Reber, J. F., & Meier, K. (1984). Photochemical production of hydrogen with zinc sulfide suspensions. *The Journal of Physical Chemistry, 88*(24), 5903-5913. doi: 10.1021/j150668a032

Reber, J. F., & Rusek, M. (1986). Photochemical hydrogen production with platinized suspensions of cadmium sulfide and cadmium zinc sulfide modified by silver sulfide. *The Journal of Physical Chemistry, 90*(5), 824-834. doi: 10.1021/j100277a024

Reich, N. H., van Sark, W. G. J. H. M., Alsema, E. A., Kan, S. Y., Silvester, S., van der Heide, A. S. H., . . . Schropp, R. E. I. (2005). Weak light performance and spectral response of different solar cell types. *20th European Photovoltaic Solar Energy Conference and Exhibition, , 6*

Rosell, J. I., Vallverdú, X., Lechón, M. A., & Ibáñez, M. (2005). Design and simulation of a low concentrating photovoltaic/thermal system. *Energy Conversion and Management, 46*(18–19), 3034-3046. doi: 10.1016/j.enconman.2005.01.012

Sarria, V., Kenfack, S., Malato, S., Blanco, J., & Pulgarin, C. (2005). New helio-photocatalytic-photovoltaic hybrid system for simultaneous water decontamination and solar energy conversion. *Solar Energy; Environmental Applications of Solar Energy, 79*(4), 353-359. doi: http://dx.doi.org/10.1016/j.solener.2005.02.022

Sasaki, Y., Nemoto, H., Saito, K., & Kudo, A. (2009). Solar water splitting using powdered photocatalysts driven by Z-schematic interparticle electron transfer without an electron mediator. *The Journal of Physical Chemistry C, 113*(40), 17536-17542. doi: 10.1021/jp907128k

Schramek, P., & Mills, D. R. (2003). Multi-tower solar array. *Solar Energy, 75*(3), 249-260. doi: 10.1016/j.solener.2003.07.004

Segal, A., & Epstein, M. (2001). The optics of the solar tower reflector. *Solar Energy, 69, Supplement 6*(0), 229-241. doi: 10.1016/S0038-092X(00)00137-7

Segal, A., & Epstein, M. (2003). Optimized working temperatures of a solar central receiver. *Solar Energy, 75*(6), 503-510. doi: http://dx.doi.org/10.1016/j.solener.2003.08.036

Shatz, N., Bortz, J., & Winston, R. (2010). Thermodynamic efficiency of solar concentrators. *Optics Express, 18*(S1), A5-A16. doi: http://dx.doi.org/10.1364/OE.18.0000A5

Sorensen, B. (2011). Chapter 4 - the energy conversion processes. *Renewable energy (fourth edition)* (pp. 337-531). Boston: Academic Press. doi: http://dx.doi.org/10.1016/B978-0-12-375025-9.00004-X

Sun, L., Hammarström, L., Åkermark, B., & Styring, S. (2001). Towards artificial photosynthesis: Ruthenium–manganese chemistry for energy production. *Chemical Society Reviews, 30*(1), 36-49. doi: 10.1039/a801490f

Tabata, M., Maeda, K., Higashi, M., Lu, D., Takata, T., Abe, R., & Domen, K. (2010). Modified Ta_3N_5 powder as a photocatalyst for O_2 evolution in a two-step water splitting system with

an Iodate/Iodide shuttle redox mediator under visible light. *Langmuir, 26*(12), 9161-9165. doi: 10.1021/la100722w

Taylor, B., & Kuyatt, C., E. (1994). *NIST technical note 1297. guidelines for evaluating and expressing the uncertainty of NIST measurement results* NIST.

Tsuji, I., Kato, H., & Kudo, A. (2005). Visible-light-induced H_2 evolution from an aqueous solution containing sulfide and sulfite over a $ZnS–CuInS_2–AgInS_2$ solid-solution photocatalyst. *Angewandte Chemie, 117*(23), 3631-3634. doi: 10.1002/ange.200500314

Tsuji, I., & Kudo, A. (2003). H2 evolution from aqueous sulfite solutions under visible-light irradiation over Pb and halogen-codoped ZnS photocatalysts. *Journal of Photochemistry and Photobiology A: Chemistry, 156*(1-3), 249-252. doi: 10.1016/S1010-6030(02)00433-1

Villoria, J. A., Navarro Yerga, R. M., Al-Zahrani, S. M., & Fierro, J. L. G. (2010). Photocatalytic hydrogen production on $Cd_{1-x}Zn_xS$ solid solutions under visible light: Influence of thermal treatment. *Industrial & Engineering Chemistry Research, 49*(15), 6854-6861. doi: 10.1021/ie901718r

Vivar, M., Skryabin, I., Everett, V., & Blakers, A. (2010). A concept for a hybrid solar water purification and photovoltaic system. *Solar Energy Materials and Solar Cells, 94*(10), 1772-1782. doi: 10.1016/j.solmat.2010.05.045

Wang, X., Maeda, K., Thomas, A., Takanabe, K., Xin, G., Carlsson, J. M., . . . Antonietti, M. (2009). A metal-free polymeric photocatalyst for hydrogen production from water under visible light. *Nature Materials, 8*(1), 76-80. doi: http://dx.doi.org.uproxy.library.dc-uoit.ca/10.1038/nmat2317

Wennerberg, J., Kessler, J., Hedström, J., Stolt, L., Karlsson, B., & Rönnelid, M. (2001). Thin film PV modules for low-concentrating systems. *Solar Energy, 69, Supplement 6*(0), 243-255. doi: 10.1016/S0038-092X(01)00051-2

Xing, C., Zhang, Y., Yan, W., & Guo, L. (2006). Band structure-controlled solid solution of formula not shown formula not shown photocatalyst for hydrogen production by water splitting. *International Journal of Hydrogen Energy, 31*(14), 2018-2024. doi: 10.1016/j.ijhydene.2006.02.003

Xu, X., Lu, R., Zhao, X., Zhu, Y., Xu, S., & Zhang, F. (2012). *Novel mesoporous $Zn_xCd_{1-x}S$ nanoparticles as highly efficient photocatalysts* Elsevier. doi: 10.1016/j.apcatb.2012.05.018

Yagi, M., & Narita, K. (2004). Catalytic O_2 evolution from water induced by adsorption of $[(OH_2)(Terpy)Mn(\mu\text{-}O)_2Mn(Terpy)(OH_2)]^{3+}$ complex onto clay compounds. *Journal of the American Chemical Society, 126*(26), 8084-8085. doi: 10.1021/ja039780c

Yan, H., Yang, J., Ma, G., Wu, G., Zong, X., Lei, Z., . . . Li, C. (2009). Visible-light-driven hydrogen production with extremely high quantum efficiency on Pt–PdS/CdS photocatalyst. *Journal of Catalysis, 266*(2), 165-168. doi: 10.1016/j.jcat.2009.06.024

Zamfirescu, C., Dincer, I., & Naterer, G. F. (2011). Analysis of a photochemical water splitting reactor with supramolecular catalysts and a proton exchange membrane. *International Journal of Hydrogen Energy, 36*(17), 11273-11281. doi: 10.1016/j.ijhydene.2010.12.126

Zamfirescu, C., Dincer, I., Naterer, G. F., & Banica, R. (2013). Quantum efficiency modeling and system scaling-up analysis of water splitting with $Cd_{1-x}Zn_xS$ solid-solution photocatalyst. *Chemical Engineering Science, 97*(2), 235-255. doi: 10.1016/j.ces.2013.04.020

Zamfirescu, C., & Dincer, I. (2013). Energy and exergy analyses of a new integrated solar energy system for hydrogen production. *The Sixth International Exergy, Energy and Environment Symposium*, Rize.

Zheng, N., Bu, X., Vu, H., & Feng, P. (2005). Open-framework chalcogenides as visible-light photocatalysts for hydrogen generation from water. *Angewandte Chemie International Edition, 44*(33), 5299-5303. doi: 10.1002/anie.200500346